UNIVERSITY OF SOUTHAMPTON

FACULTY OF PHYSICAL AND APPLIED SCIENCES
Physics

All-optical control of hybrid plasmonic semiconductor-metal nanostructures

by

Martina Abb

Thesis for the degree of Doctor of Philosophy

June 18, 2012

UNIVERSITY OF SOUTHAMPTON

ABSTRACT

FACULTY OF PHYSICAL AND APPLIED SCIENCES
Physics

Doctor of Philosophy

ALL-OPTICAL CONTROL OF HYBRID PLASMONIC SEMICONDUCTOR-METAL NANOSTRUCTURES

by Martina Abb

This thesis is dedicated to the study of linear and nonlinear properties of closely spaced gold nanoparticle dimers, so-called nanoantennas, and hybrid nanoantenna devices consisting of metals and semiconductors. Coupled nanoparticles are of particular interest for nanophotonics because of their ability to focus light into subwavelength volumes and the associated large field enhancement in the gap.

The samples used in this thesis are gold rectangles designed by electron-beam lithography, with both symmetric and asymmetric arms, as well as symmetric closely spaced 100 nm disk dimers which were fabricated by colloidal lithography in combination with angle-dependent evaporation. We investigate the linear interplay of modes in the two arms with Spatial Modulation Microscopy, an experimental technique which results in a measure directly proportional to the extinction cross-section. We find a variety of constructive and destructive interference between different order modes, which we can better understand by comprehensive simulations of antennas, varying the parameter space of gap size (coupling strength) and length-length ratio using advanced numerical methods such as the Fourier Domain Time Difference and the Boundary Element Method. We find that the presence of nonradiative modes is made visible by Electromagnetically Induced Transparency.

In order to probe the nonlinear properties of the antennas and their interaction with Indium Tin Oxide substrates, a pump-probe setup is used to get an insight into ultrafast nonlinear response with picosecond resolution. These measurements (and corresponding fits using numerical simulations) lead us to identify a new energy transfer mechanism where fast electrons are injected from the nanoparticles into the semiconductor, resulting in a refractive index change due to heating of the surroundings. In follow-up experiments, we find this mechanism to be universal (and versatile) for other types of transparent conductive oxides. These results open new avenues towards application of nanoantennas for ultrafast switching.

Contents

Acknowledgements

At the end of this thesis and of my three years as a PhD student, there are quite a few people to whom I want to express my gratitude.

First of all, I want to thank my supervisor Otto Muskens for giving me the opportunity to do research on such an exciting topic – even though I had to convince him that a dumb theoretician like me is capable of experimental work when I was applying three years ago! ;-) Otto's enthusiasm for research is truly catching and I've always had a lot of fun while learning a lot during my PhD. He is also a great example at problem solving and at "getting things done", which I am sure is something every postgraduate student (and a great many postdocs and lecturers) aspires to!

Otto also made it possible for me to visit San Sebastian to learn more about simulations, and especially BEM. I also want to thank Javier Aizpurua for the support that made this visit possible as well as the fruitful collaborations. On that note, I also want to say thank you to Pablo, Ameen and the rest of Javier's group for making me feel welcome during my stay and for answering my truckload of questions!

Another fruitful collaboration was with Borja Sepúlveda from Barcelona who provided the nice dimer metamaterial samples discussed in chapter 6. This added another dimension to the research done for this thesis, and it was truly a pleasure to work on these samples.

Back to Southampton now: I'd also like to thank Otto, Alex and Carola for proofreading this thesis and eliminating the numerous small mistakes – thank you! Thanks also go to Tom and Tasha, but also to the various other people we've shared an office with throughout the years, who have always provided a good working environment; I've always enjoyed coming to work in the mornings!

A special thank you goes to Carola – I don't know how many coffees we've had between the two of us over the last three years, but I know that it's been quite a number! Thanks for the good company and for sharing both successess and failures during the last 3 years. I hope we keep in touch in the years to come!

Without Zondy's help and experience in nanofabrication I would have been lost when I first started my PhD. Thank you for the training sessions on many different cleanroom

fabrication tools and for always being available when something didn't go the way it was supposed to! I'd also like to thank Mark and Phil for building some of the components in our setup, as well as Gareth. Gareth was always available when a piece of our lab equipment blew a fuse – thanks for that, too!

Due to our collaborators Harold Chong and Kees de Groot, we were able to make use of the new, high-standard Mountbatten cleanroom facilities. Thanks to Yudong, who prepared some of the e-beam designed antennas and got so involved that he finally began his mails to me with "Dear Antenna"...;-) I'd also like to thank Owen, Kanad, Stuart, Peter and Jim for training sessions and help with the various tools in the ECS cleanroom. Another thank you goes to Neil Sessions and Dave Sager from the ORC cleanroom for help with ITO evaporation and for sharing their knowledge on annealing of ITO.

I'd like to thank Richard Whiter and David Smith for the introduction to electrochemical deposition, which is something I can see great potential in for the fabrication of nanoantenna switches and hope to pursue in the future.

I would also like to thank my thesis committee, Hendrik Ulbricht, who has already been my advisor during the last three years, as well as José Sánchez-Gil – thanks for being my examiners! (Let's see if I still say the same after my viva...;-)!)

Last but not least, I want to express my gratitude to my parents. They have always been backing me all the way as well as supported me in any decisions I made. For this, and all their love, I will be eternally grateful. I'd also like to thank my sister Sabine – thanks to all the moaning about your exams I could always feel sure that I hadn't drawn the worst lot! ;-) I also enjoyed the summer you spend here, I hope you know that you're welcome here anytime! And I hope we'll manage to come and visit Tuebingen for the next chocolate market! :)

The biggest thanks goes to the love of my life Alex, for his neverending love and support. Even though the last three years have not always been easy, what with being so far apart, I think we truly managed to make the best of it – and you cannot imagine how much I'm looking forward to you moving here! Thank you for being you, and for being there for me. I love you.

This thesis is dedicated, with love, to my family.

Martina Abb
May 2012
Southampton, UK

List of Publications

Portions of this thesis have been drawn from the following publications:

M. Abb and O. L. Muskens, “Modeling and experimental realization of nanoantenna hybrid optical switching devices”, Proc. SPIE **8096**, 809617 (2011).

M. Abb, Y. Wang, P. Albella, C. H. de Groot, J. Aizpurua and O. L. Muskens, “Interference, coupling and nonlinear control of high-order modes in single asymmetric antennas”, submitted to ACS Nano (2012).

N. Large, M. Abb, J. Aizpurua and O. L. Muskens, “Photoconductively Loaded Plasmonic Nanoantenna as Building Block for Ultracompact Optical Switches”, Nano Lett. **10**, 1741 (2010).

M. Abb, P. Albella, J. Aizpurua and O. L. Muskens, “All-Optical Control of a Single Plasmonic Nanoantenna-ITO Hybrid”, Nano Lett. **11**, 2457 (2011).

M. Abb and O. L. Muskens, “Ultrafast Plasmonic Nanoantenna-ITO Hybrid Switches”, Int. J. of Opt. **12**, 132542 (2012).

M. Abb, B. Sepúlveda, H. M. H. Chong and O. L. Muskens, “Transparent conducting oxides for active hybrid metamaterial devices”, submitted to J. of Opt. (2012).

Chapter 1

Introduction

As we know from the Abbe diffraction limit, light cannot be focussed below roughly half its wavelength [1]. While techniques have been developed to circumvent and breach this limit, resonant metallic nanostructures already inherently offer a strong subwavelength confinement of light in the near-field [2]. These field confinements entail large field enhancements and are caused by the excitation of free electron oscillations (so-called *plasmons*) in the particles by incident light.

This chapter begins with a historical perspective on metallic nanostructures and continues with a selection of recent developments and achievements in the relatively young research field of plasmonics. Optical properties of metals and the concepts of surface plasmon polaritons and nanoantennas are discussed in detail. An outline of this thesis is presented in the final section of this chapter.

1.1 Plasmonics past and present

The scientific interest in optical properties of metal nanoparticles reaches far back in history to Faraday who first investigated the colourful appearance of colloidal solutions of gold nanoparticles [3]. These resonances are a result of induced surface charges caused by the excitation of collective electron oscillations with respect to the lattice ions, as shown in Fig. 1.1 a). Depending on size, material properties and shape, nanoparticles scatter light at different wavelengths, as shown in Fig. 1.1 b), where a direct comparison between scanning electron micrographs (SEM) and scattering is drawn. These scattering properties have been made use of long before there was any scientific interest in nanoparticles and nanostructures – the Romans used nanoparticles to create dichroic glass of vivid colours (as found in the Lycurgus cup exhibited in the British Museum whose opaque green turns to ruby red when light is shone through it); many stained glass windows found in churches (such as in the Sainte Chapelle in Paris) are equally enriched with colloidal nanoparticles.

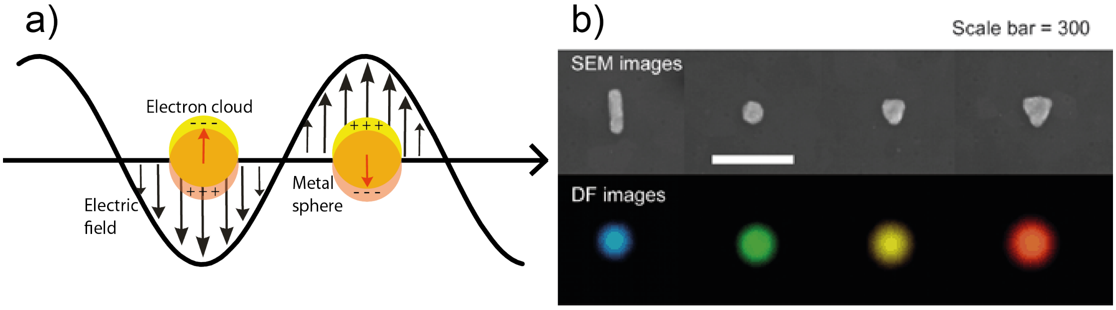

Figure 1.1: a) Schematics of the vibration of free electrons with respect to the lattice for excitation of a localized surface plasmon. b) Nanoparticles of different size and form absorb/scatter light of different wavelengths. a) is inspired by [4], b) is taken from [5].

Modern microscopy methods have made it possible to image single nanoparticles (see panel b) of Fig. 1.1) and to characterise their optical properties. Single particle spectroscopy allows the investigation of small shape variations, whereas spectroscopy of ensembles [6] results in an average of similar, but not completely identical particles. From a theoretical point of view, analytical solutions have been found for the optical response in a limited number of geometries with special symmetries, e.g. for nanospheres [7] and nanorods [8]. Additionally, a number of approximations were found to yield excellent agreement, such as for long nanowires (quasi-one dimensional systems) [9, 10]. To realistically model more complicated geometries (such as nanorice [11], nanostars [12, 13] and many more) and include the effects of adhesion to substrates as well as small form deviations [14], a variety of numerical tools to solve Maxwell's equations has been developed which will be explained in more detail in the next chapter.

Localised plasmon resonances as sustained by nanoparticles are the subject of this thesis. There is, however, another type of plasmons that needs to be mentioned: propagating surface plasmon-polaritons which can be found on metal-dielectric interfaces and which are also very useful, especially in the areas of sensing and information technology. Their derivation from Maxwell's equations will be one of the topics of the next section.

Nowadays, the original investigations into properties of nanoparticles have progressed into further fundamental research as well as a vast range of applications, mainly in communication and information technology as well as in the life sciences. In cancer research for example, nanoparticles act as local heaters to concentrate radiation into infected areas and selectively kill tumor cells [15]. This concept has been developed in particular for core-shell particles consisting of different components [16] due to their high tunability and absorption. Chemical functionalisation of nanoparticles allows for specific targeting and gentle treatment. Several therapies based on gold nanoparticles have already passed phase I clinical trials.

Another already commercially exploited application of surface plasmons is “plasmonic biosensing”. Plasmons are very sensitive with respect to their surroundings, so even monolayers of molecules or proteins can lead to sizable shifts of the resonance. Such sensors have been developed for testing for pregnancy, prostrate cancer or HIV-AIDS [17].

Hydrogen sensing has also proven a novel application for metal nanostructures. Sensing of hydrogen is routinely done using Palladium, which selectively absorbs hydrogen gas and forms a compound. Liu et al. have recently developed a sensor where a palladium nanoparticle is positioned in the hotspot of a gold nanoparticle, measuring changes in molecular concentration in the system on the single particle level [18].

Another use of nanoparticles is for label-free imaging, where nanoparticles are used instead of fluorescent markers. The particles can either be used in cells or samples, or directly on the imaging device. In 2007, the group of F. Capasso used a dimer nanoantenna on top of already well-established quantum-cascade lasers to create a sharp focus of less than 100 nm in the near-field [19]. This device was then used for biological imaging, opening up new insights at the nanoscale.

Near-field microscopy techniques can also be used to detect single molecules (first done in 1994 by E. Betzig et al. [20]), where fluorescent molecules are detected and tracked by collecting the emitted fluorescence with a near-field probe. Another way to detect single molecules lies in Raman scattering. By itself, Raman scattering is a fairly weak process, but it was found to be enhanced by several orders of magnitude in the presence of hotspots generated by nanoparticles, thus allowing detection of vibrational modes of a single molecule in such a hotspot [21]. This technique is called Surfaced Enhanced Raman Scattering (SERS).

In recent years, plasmonics has also been discovered as a means to improve the efficiency of solar cells. Positioning nanoparticles at the surface or further inside the solar cell is predicted to enhance light trapping in thin-film solar cells and make solar cells up to 30% more efficient [22]. First plasmon-enhanced solar energy conversion devices have already been demonstrated experimentally [23].

Photodetection with active optical antennas is another recent application of plasmonic structures. Knight et al. recently demonstrated experimentally how fast electrons generated by plasmonic decay can be captured as a photocurrent [24]. This work allows to build exquisitely sensitive detectors tunable to the desired range of wavelengths.

Nanostructured units can also make up what is referred to as *metamaterials* – engineered materials that exhibit properties that do not occur in any known natural materials. For example, it has been shown that negative refraction [25, 26] can be achieved this way, and that light can be bend around objects in order to disguise and hide them [27, 28, 29].

Integrated plasmonic/photonic circuits [30, 31, 32] are another field that commands a lot of public attention. Plasmonic devices are smaller than other photonic elements, and inherently much faster than any purely electronic technology. Waveguiding, all-optical modulators and hybrid devices working with both photons and electrons [33] for information processing are just some of the possibilites – the compatibility with standard CMOS fabrication techniques makes the integration capabilites endless.

This section only lists a few of the countless applications of plasmonic devices - to present a full list here would exceed the scope of this thesis. The different applications listed here can only give a first impression of the many directions in plasmonics research.

From a more fundamental point of view, our understanding of the physics leading to those applications continues to grow [34, 35]. New imaging techniques have been developed, and direct imaging of near-field enhancement (e.g. with scanning near-field optical microscopy [36, 37]) and plasmonic propagation has been achieved. For example, the resonant mode structure of gold nanostructures can be mapped out spectrally and spatially using two-photon excited luminescence (TPL) [38, 39], where the incoming light is strongly focussed into the hotspots, leading to two-photon absorption in gold and thus to wide-band photoluminescence emission.

Both the surge in characterisation techniques, the additional computational power for design and modelling that is available now and the rise of modern nanofabrication techniques allow fast progress to ever smaller dimensions. First theoretical investigations of "quantum plasmonics" [40] have already been conducted numerically a few years ago, and more recently, first experimental progress towards the quantum regime has been made [41] in plasmonic systems. To conclude, all these recent advances have led to a rapid increase of knowledge and a tremendous growth of the field of plasmonics [42] – and it continues to grow.

1.2 Optical properties of metals

The optical properties of nanoparticles differ from those of the corresponding bulk material by displaying non-propagating plasmonic resonances, depending on shape, size and material. However, one cannot describe the interaction of light and nanoparticles without taking into account the optical properties of the bulk material [8], which are fully described by its complex frequency-dependent dielectric function $\epsilon(\omega) = \epsilon_{\text{real}} + i\epsilon_{\text{im}}$. The real and imaginary part of the dielectric functions of gold and silver, the two materials commonly used to fabricate plasmonic structures, are shown in Fig. 1.2, as given by experimental data taken from Palik [43]. In the following subsections, the behaviour of bulk metals is explained first by the Drude model approximation before we take a closer look at propagating and localized surface plasmon-polaritons.

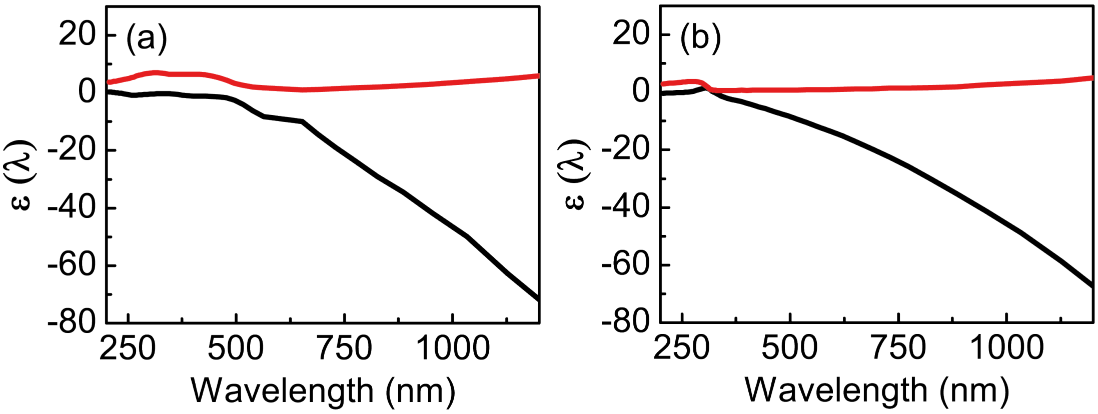

Figure 1.2: Dielectric functions of the two most common materials used for plasmonic structures: gold (a) and silver (b), as provided by Palik [43]. The imaginary part of the dielectric function is depicted in red, the real part in black.

1.2.1 The dielectric function of metals

The dielectric function describes the frequency-dependent behaviour of the material. For metals, the typical behaviour can be seen in Fig. 1.2: At long wavelengths in the IR, metals can be regarded as perfect conductors with infinitely large negative permittivity ϵ. In the visible region, on the other hand, the real part of the dielectric function even reaches positive values, and the imaginary and the real part are similar in magnitude.

The optical behaviour of metals is often described by a model developed in 1900 by Paul Drude, the so-called *Drude model*. For example, the optical properties of gold are very well described by the dielectric function of the Drude model [44], ideally with additional terms accounting for the interband transitions at 330 and 470 nm [45]. Not unlike kinetic theory, the Drude model assumes that the electrons in the valence band of such materials behave as a free electron gas, oscillating around the fixed lattice of ions. The electrons themselves neither interfere with each other nor are there any long-range interactions with the positively charged fixed ion lattice. The only possible interactions are quasi-instantaneous collisions between the free electrons and the ions, which are assumed to happen at a fixed rate $\gamma = 1/\tau$, with τ the average time between collisions. The corresponding equation of motion is therefore

$$m_e\ddot{r} + m_e\gamma\dot{r} + m_e\omega_0^2 r = eE(t), \tag{1.1}$$

with m_e the electron mass, e the charge and ω_0 the eigenfrequency. In metals, there usually are no restoring forces acting on the electrons, which means the eigenfrequency can be set to zero and we lose the linear term. As a solution of this differential equation for an external oscillating field $E(t) = E_0 e^{-i\omega t}$, we obtain:

$$r(t,\omega) = -\frac{e}{m_e(\omega^2 + i\gamma\omega)} E(t). \tag{1.2}$$

This displacement results in the macroscopic polarization $P = -N_e e r$, where N_e describes the electron density. Inserting this into the well-known combination of electric field E and polarization P that make up the dielectric displacement $D = \epsilon_0 E + P$, we find for the frequency-dependent dielectric function

$$\epsilon(\omega) = 1 - \left(\frac{\omega_{\mathrm{pl}}}{\omega}\right)^2 \frac{1}{1 + i\frac{1}{\omega\tau_D}}\,. \tag{1.3}$$

Here, ω_{pl} denotes the plasma frequency, $\omega_{\mathrm{pl}} = \sqrt{N_e e^2/\epsilon_0 m_e}$, and τ_D the relaxation time. Despite its simplicity, the Drude model gives surprisingly good agreement with experimental data [45]. In this thesis, we will use the Drude model not only to describe the optical properties of metals, but also for semiconductors (e.g. in chapter 4): Light with energy below the bandgap is able to excite free electrons in the semiconductor, which in turn behave as a free electron gas and can thus be modelled by the Drude model.

1.2.2 Propagating surface plasmon-polaritons

Plasmons, as already mentioned, are the quantised plasma oscillations of the free electron gas in metals. Incident photons can couple to plasmons and create plasmon-polaritons. Surface plasmon-polaritons (SPPs) are a solution of Maxwell's equations at the interface of a metal and a dielectric material [46]. Let us have a closer look at a SPP mode propagating in x-direction between a metal with the dielectric function ϵ_m and a dielectric medium with ϵ_d. As a solution to Maxwell's equations, we find the SPP:

$$E_x = Ae^{ik_{x1}x}e^{k_{z1}z}, E_z = Be^{ik_{x1}x}e^{k_{z1}z} \quad \text{for} \quad z < 0. \tag{1.4}$$

$$E_x = Ce^{ik_{x2}x}e^{-k_{z2}z}, E_z = Be^{ik_{x2}x}e^{-k_{z2}z} \quad \text{for} \quad z > 0. \tag{1.5}$$

This wave is the propagating plasmon-polariton, which propagates along the x-direction $\big[$see Fig. 1.3a)$\big]$. The fields perpendicular to the surface decay exponentially with distance and are said to be "evanescent" $\big[$shown in Fig. 1.3b)$\big]$. Assuming that the parallel and perpendicular electric fields are continuous on the interface, we can derive the dispersion relation for the SPP, where $k_{x1} = k_{x2} = k_{\mathrm{SPP}}$:

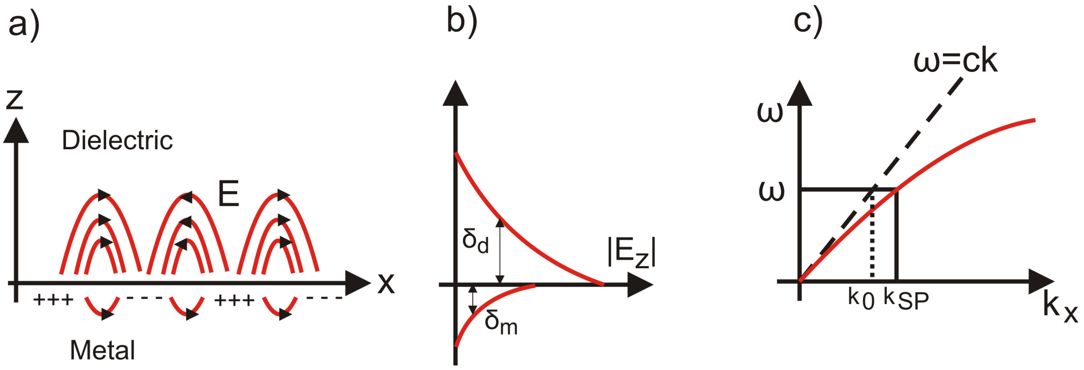

Figure 1.3: a) Schematics of a propagating SPP. The interaction between light and electrons leads to a propagating charge oscillation at the interface between metal and dielectric. b) The evanescent fields in the perpendicular direction decay exponentially and limit the propagation length of the SPP. c) The dispersion curve of a SPP mode. The mode clearly lies below the light line $\omega = ck$, which means that the momentum mismatch has to be overcome in order to couple to the mode.

$$k_{\mathrm{SPP}} = k_0 \left(\frac{\epsilon_m \epsilon_d}{\epsilon_m + \epsilon_d} \right)^{1/2}. \tag{1.6}$$

On plane metal films, SPPs can thus propagate in parallel to the interface with a k-vector larger than that of light in vacuum, which is one of the reasons for the increased popularity of SPPs [47]. This mismatch between incoming light and the propagating plasmon mode [48] can be overcome by using a grating to match the k-vectors to each other. Other ways to achieve the momentum matching are prism coupling directly to a thin metal film (*Kretschmann-Raether geometry*) or by prism coupling through a small gap onto the underlying metal layer (*Otto geometry*) [49].

The propagation length $\big[$see Fig. 1.3b)$\big]$ can be estimated by looking at the imaginary part $\mathrm{Im}(k_{\mathrm{SPP}})$ of the surface plasmon vector:

$$\delta_{SP} = \frac{1}{2\mathrm{Im}(k_{\mathrm{SPP}})} = \frac{1}{k_0} \left(\frac{\epsilon_{m1} \epsilon_d}{\epsilon_{m1} + \epsilon_d} \right)^{3/2} \frac{\epsilon_{m1}^2}{\epsilon_{m2}}, \tag{1.7}$$

where $\epsilon_m = \epsilon_{m1} + i\epsilon_{m2}$ is the dielectric function of the metal. Silver is the metal which has the lowest losses in the visible and reaches typical propagation distances in the range of 100 μm, which makes the integration of SPP-based elements into circuits possible.

In this thesis, propagating suface plasmon-polaritons are only discussed for reasons of completeness – the topic of this thesis are localised surface plasmons, which will be discussed next.

1.2.3 Localised surface plasmons (LSP)

The coupling issues of propagating plasmon-polaritons are of no concern to the non-propagating localised surface plasmon polaritons that are observed when focusing light on nanoparticles. One can consider an LSP as a standing wave constricted to the surface of a nanoparticle that therefore interferes with itself. Obviously, this results in high sensitivity with respect to the shape of the particle.

Particle plasmons are excitable by direct illumination of the particle with light of the resonant frequency. For particles that are smaller than the skin depth of the electromagnetic field, the electric field can be considered as constant, and the nanoparticle acts as a dipole. This is called the *quasi-static approximation*. Using this approximation [8], the polarisability of a nanosphere with volume V becomes:

$$\alpha = 3V\epsilon_0 \frac{\epsilon_m - \epsilon_e}{\epsilon_m + 2\epsilon_e}, \tag{1.8}$$

with ϵ_m the dielectric function of the nanosphere material and ϵ_e that of its environment. The polarisability describes the change in electron distribution in response to the electric field of the incoming light. The polarisability obtained here (also known as the Clausius-Mossotti relation) is identical to the result one obtains from Mie theory in the small-scatterer (Rayleigh) limit [7]. Both the scattering cross section σ_{scat} and the absorption cross-section σ_{abs} can be written as a function of the polarisability [8]:

$$\sigma_{\text{scat}} \propto |\alpha|^2, \tag{1.9}$$

$$\sigma_{\text{abs}} \propto \text{Im}[\alpha]. \tag{1.10}$$

These are general expressions and can be shown by applying the optical theorem. For our example of the nanosphere, Eq. (1.8) means that there is a plasmon resonance for $\epsilon_m = -2\epsilon_e$, assuming the imaginary part to be negligibly small (which is the case for gold and silver in the visible range of the spectrum where the resonance condition is fulfilled). Negligibly small still means larger than 0, however, resulting in absorption being the dominant process for small particles. For larger particles (bigger than 50 nm), it is the scattering that dominates, due to the square dependency in the scattering cross section. The extinction cross-section is the sum of both:

$$\sigma_{\text{ext}} = \sigma_{\text{scat}} + \sigma_{\text{abs}}. \tag{1.11}$$

For large particles, the quasistatic approximation (1.8) fails, since the electric field affecting the particle cannot be considered as uniform across the particle. That means

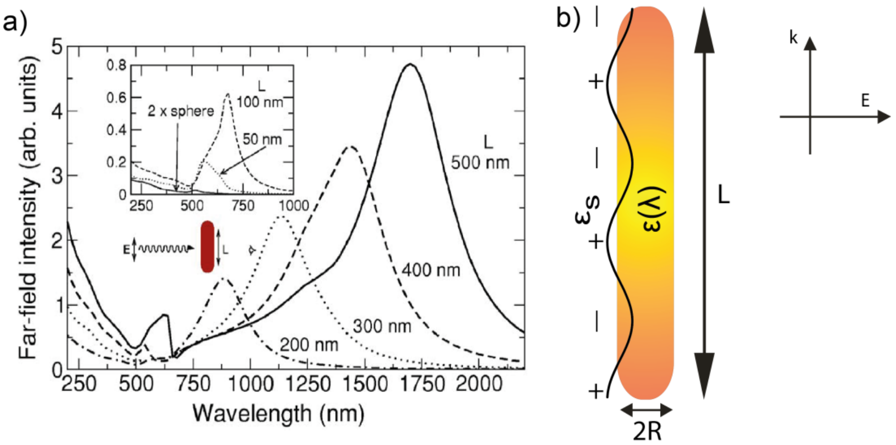

Figure 1.4: a) Full electromagnetic calculations of the far-field spectra in dependence of the length of the single nanorod antennas, from [50]. Copyright (2005) by the American Physical Society. b) Schematic rendition of an antenna as used in the derivation of the effective scaling law.

retardation effects have to be taken into account, and full electromagnetic numerical calculations have to be used for realistic results, as dicussed in the next chapter.

1.3 Nanoantennas - design and functionality

Antennas as we find them on our roofs were first developed at the beginning of the 20th century, with the most common the Yagi-Uda antenna - our stereotypical TV antenna. Since then, research into antenna characteristics such as directivity of reception and emission as well as bandwidth has taken conventional antenna designs to smaller and smaller dimensions. The length of the elements of a macroscopic antenna such as those used to receive radio or TV is usually half the wavelength of the signal they are intended to receive. Whereas TV and radio typically work in the range of 40 - 1000 MHz and are thus of the order of meters, antennas used in mobile phone and wireless networks are a lot smaller.

The size of the antennas is obviously its most crucial design parameter. For ideal antennas where we assume perfect conductivity for cylindrical rods as well as no penetration of the electromagnetic radiation (this also means that the negative real part of the dielectric function is infinite), the following relation holds true for the length L of the antenna:

$$L = \frac{\lambda}{2n} l, \tag{1.12}$$

where n is the refractive index of the surrounding medium and l the order of the mode. $l = 1$ is the fundamental resonance, larger l-values stand for higher order modes.

However, these are not conditions that we can easily assume for very small antennas. For visible light and NIR, we need antennas of the order of nano- to micrometers, where the penetration is no longer negligible. As we can see in Fig. 1.4a), antennas in this part of the optical spectrum do not adhere to the half-wavelength rule anymore: We find that the length of the antenna is quite a bit smaller than half the wavelength of its resonance. This means that the resonance condition is not fulfilled for $\lambda/2 = \lambda_{\text{res}}$, but instead for a shorter effective wavelength λ_{eff}. Novotny developed an analytic approximation to describe this effective wavelength scaling for nanorods and showed that a linear scaling applies, with $\lambda_{\text{eff}} = n_1 + n_2\lambda/\lambda_p$. A detailed derivation can be found in Ref. [51].

Novotny assumes a metal as described by the Drude model and as metal antenna a cylindrical nanorod of length L and radius $R \ll \lambda$ $\left[\text{see Fig. 1.4b)}\right]$, with $R \ll L$ sufficiently small. The approximation then yields

$$\begin{aligned}\lambda \approx \left(\frac{\lambda_p \epsilon_s}{0.12\sqrt{\epsilon_\infty + 141.04\epsilon_s}}\right) \cdot \Bigg(&\frac{nL}{4\pi R} \\ &-13.74 - \frac{0.12}{\epsilon_s}\left[\sqrt{\epsilon_\infty + 141.04\epsilon_s}\right] - \frac{2}{\pi}\Bigg).\end{aligned} \tag{1.13}$$

Here, $\lambda_p \approx 138$ nm is the plasma wavelength of gold, $\epsilon_\infty \approx 11$ the infinite frequency limit of the dielectric function for gold, ϵ_s the surrounding medium, n is the order of the mode and L the length of the nanorod including endcaps.

This analytical approximation for the optical frequency regime where metals behave as strongly coupled plasmas shows good agreement both with full electromagnetic simulations [50, 51, 52] as well as with experimental data in the IR [53, 54, 55]. We will make further use of this effective scaling law in chapter 3 in order to get a better overview of higher order modes in asymmetric dimers.

The wavelength scaling holds true as a good approximation for plasmon resonances along the long axis of a nanorod of reasonable length. However, this is not the only resonance that a nanorod sustains: Apart from the higher order modes mentioned earlier, we also find a transverse mode along the short axis of the nanorod. Both resonant modes depend crucially on the length and width of the nanorod in question. Another strong influence on the resonant wavelength is the dielectric function of the surrounding medium. For example, a nanorod in water (refractive index of 1.33) has a redshifted resonance compared to one in air (refractive index of 1). This property is used in sensing, where even small refractive index changes in the surrounding medium may shift the resonance wavelength.

Another redshift occurs when nanorods are placed in close vicinity of each other and their resonances couple, which we will investigate in more detail in chapter 3. This coupling in dimers leads to a sizable redshift of the resonance for small distances [50],

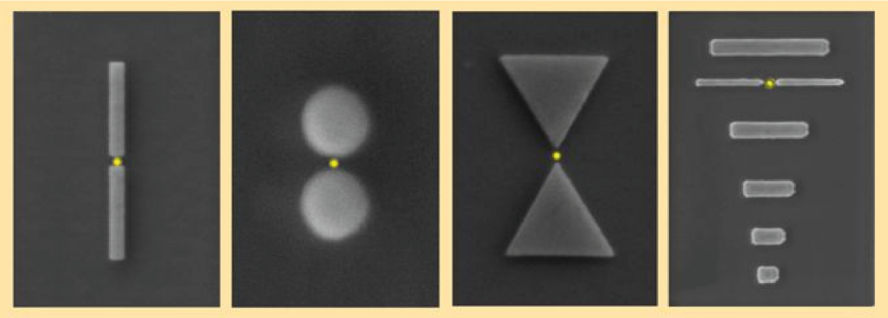

Figure 1.5: A variety of optical antennas, here from left to right: A gap antenna, a Hertzian antenna, a bowtie antenna and a Yagi-Uda antenna. The scanning electron pictures are taken from [37]. Reprinted with permission from [37]. Copyright (2011), American Institute of Physics.

and in monolayers of nanoparticles to a number of effects which can be described by effective medium theories [56]. Additionally, the field is enhanced by several orders of magnitude in the gap between particles, which is of great interest for sensing, fluorescence measurements, and Raman spectroscopy [57].

The tremendous advances in nanofabrication during the last decades have made it possible to manufacture such antennas on the nanoscale. They are routinely fabricated using a number of different methods, such as electron beam lithography [58], focussed ion beam (FIB) milling [59] and electrochemical growth [60, 61, 62]. These nanoscale devices are often referred to as "optical antennas" [37, 63, 64] since they work in the visible and NIR part of the spectrum.

Optical antennas convert incident optical radiation into localized energy very efficiently. When properly configured (for example as a so-called Yagi-Uda antenna), they can also work the other way round and direct the emission of light from an emitter positioned with nanoscale accuracy next to the antenna [65]. Another concept using antennas for emission is that of the spaser (**s**urface **p**lasmon **a**mplification by **s**timulated **e**mission of **r**adiation), the plasmonic equivalent of the laser [66], with a nanoparticle as the resonant cavity and surface plasmons instead of photons. This concept has yet to be proven successful in experiments, but demonstrates just one aspect in which nanoantennas hold great potential for future applications.

In practice, there is an endless number of antenna designs, ranging from simple nanorod antennas to complex fractal patterns [37]. We will briefly introduce the most common designs for nanoantennas here. For corresponding SEM pictures of lithographically designed structures, see Fig. 1.5. On the left, we find a gap antenna that scatters as an effective linear dipole. This kind of dimer antenna is what will be used and referred to throughout this thesis as a nanoantenna. Next to it is a Hertzian antenna consisting of two closely positioned spheres, which provides superior radiation efficiency [37]. Third is a bowtie antenna, where the tapered geometry is ideal for broadband reception and/or transmission. On the right is a Yagi-Uda antenna, the most complicated structure of the designs presented here. It provides highly directional emission due to the interplay between its components. The yellow dots indicate where receiver or transmitter (for example in the form of a fluorescent molecule or a quantum dot) would be placed.

1.4 Outline of this thesis

This thesis is structured into seven chapters. After the introduction in this chapter, chapter 2 provides the basics in the form of the three pillars used for most nanophotonics research: simulation, fabrication and characterisation. We will look at solving Maxwell's equations for nanoparticles by advanced simulation methods such as Boundary Element, Finite Element and Finite Difference Time Domain calculations. Next, we look at how the nanostructures used in this thesis are fabricated using either colloidal lithography or electron-beam lithography, as well as at a variety of deposition techniques such as sputtering, evaporation and atomic layer deposition for cover layer deposition. Last but not least the experimental techiques are introduced: Spatial Modulation Microscopy for the linear spectral characterisation and pump-probe spectroscopy to probe the nonlinear response.

Chapter 3 looks at the behaviour of localised surface plasmons in coupled dimers, first in the case of coupled symmetric dimers, looking at both gap dependence and field enhancements in coupled symmetric structures as well as the higher order modes they sustain. Next, we look at coupling in asymmetric dimers, where the coupling of higher order modes is of great interest because nonradiative modes can be detected due to their interaction with radiative modes, as we will show with Spatial Modulation measurements. The underlying interaction is further invested in detail by looking both at near- and far-field simulations.

In chapter 4, the concept of using plasmonic nanoantennas as all-optical and potentially ultrafast switches is introduced, exploiting the dependence of the plasmon resonance on the coupling. By locally inserting a semiconductor junction in the gap, we show that the capacitive coupling of closely spaced antenna arms can be "switched" to conductive coupling by exciting free carriers in the gap through optical pumping below the bandgap, effectively bridging the gap. The merits and possibilities of experimental realisations are also discussed. We also look at gaploading for configurations exhibiting destructive interference in asymmetric dimers, where the aforementioned interplay between modes of different orders makes for more complex switching dynamics.

Chapter 5 looks at a first experimental realisation of the concept of nanoantenna switches. We choose Indium Tin Oxide (ITO) as a nonlinear material to fully cover the antennas. The nonlinear optical response of ITO is more than an order of magnitude smaller than the response we observe for antenna-ITO hybrids. Unlike for pure gold antennas, we find a characteristic bipolar response which corresponds to a redshift of the plasmon resonance. When compared to numerical simulations, this cannot be accounted for by free electrons generated in the ITO. What we discover instead is that the ITO around the antennas is locally heated by fast electron injection from the illuminated gold antenna, causing a sizeable shift in the refractive index of the surroundings.

In chapter 6, we further expand on this: Using a large-area dimer metamaterial as a basis, we use different conductive oxides such as ITO and aluminum doped zinc oxide (AZO) as cover layers. We observe the same nonlinear response as in Chapter 5 – a bipolar signal much bigger than the response of just the conductive oxide. This further indicates that the gold antenna acts as a local sensitizer for the nonlinear response of the cover material.

In chapter 7, we present a summary of the results obtained in this work and look at future plans and realisations of the concepts and ideas introduced in this thesis. In particular, the energy transfer mechanism by hot electron injection followed by local heating has been shown to be extremely versatile and universal, which opens up further investigations in several veins that are discussed and expressed more thoroughly in this section.

Chapter 2

Simulation, fabrication and characterisation of nanostructures

In this chapter, we introduce the three pillars necessary on which the research results shown in the following chapters are build: Simulation, nanofabrication and characterisation of nanoantenna dimers. The simulational tools presented here are the Finite Element Method (FEM), the Boundary Element Method (BEM) and Finite Difference Time Domain (FDTD) simulations, which were all used in this thesis. The BEM calculations presented in this thesis were done with the code provided by J. Aizpurua in San Sebastian, and N. Large ran the simulation for gap-loading of symmetric dimers (published in [67]). Similarly, all the FDTD (Lumerical) calculations were done by P. Albella of the same group. All the FEM calculations as well as the BEM simulations of chapter 3 and section 4.2 were done by myself.

The section on nanofabrication is divided into three parts. First, the electron-beam lithography of nanoantenna dimers is presented. Nanoantennas were fabricated in the Rapid Prototyping Facility (RPF) of the School of Physics (cf. chapter 5 and partially chapter 3). Other samples were fabricated by Y. Wang in the Mountbatten Cleanroom, where the resolution of the e-beam (JEOL JBX-9300FS) is much better due to its 100 keV emission gun. Second, the colloidal lithography combined with angle-dependent evaporation is presented. This process is being developed to high sophistication at the moment [68, 69, 70, 71] and holds great promise for the cheap fabrication of large-area metamaterials. The samples which were used for the work presented in chapter 6 were fabricated up to lift-off by Dr Borja Sepúlveda in the cleanroom at Chalmers University, and then handed over to me for further processing. This leads us to the nanofabrication part three, the deposition of conductive oxide layers. Before the new Mountbatten cleanroom facilitiy was opened, r.f. sputter deposition in the RPF was used and optimised which therefore takes up a large part of this section. Later, ITO evaporation and subsequent annealing as well as atomic layer deposition of Al-doped zinc oxide in the Mountbatten Cleanroom were used for some of the samples in chapter 6.

All characterisation was done in the spatial modulation and pump-probe microscope setup build with a ps Fianium supercontinuum laser in our labs.

2.1 Simulation

All simulation techniques that are presented in this section are based on numerically solving Maxwell's classical equations. As a reminder, the differential equations describing all electromagnetic interaction of light and matter are as follows:

$$\begin{aligned}
\nabla \cdot \vec{E} &= \frac{\rho}{\epsilon_0}, && (2.1)\\
\nabla \cdot \vec{B} &= 0, && (2.2)\\
\nabla \times \vec{E} &= -\frac{\partial \vec{B}}{\partial t}, && (2.3)\\
\nabla \times \vec{B} &= \mu_0 \vec{J} + \mu_0 \epsilon_0 \frac{\partial \vec{E}}{\partial t}. && (2.4)
\end{aligned}$$

Maxwell's equations can also be expressed in integral form by using the divergence theorem and the Kelvin-Stokes theorem, respectively. Both forms are equivalent, and some of the simulation methods use one form, some the other. For example, the Boundary Element Method uses the integral form to calculate fields from given charge and current distributions.

2.1.1 Finite Element Method (FEM)

The Finite Element Method was first developed in the 1940s and has been used for almost every research field imaginable, demonstrating its great versatility [72] from applications in architecture to climate and weather simulations. It is a sophisticated numerical technique that finds approximate solutions of partial differential equations for a discritised mesh of a continous domain, which divides the domain into a set of discrete finite subdomains, so-called *mesh elements*. The developed meshing techniques are what makes FEM so generally applicable: It is easy to use a finer mesh for critical points, such as a strong bend in the geometry. In this thesis, we use the FEM software Comsol 3.5 [73]. Comsol provides a graphic interface as well as a connection with Matlab for scripting, which can for example be used to generate large numbers of scatterers [74].

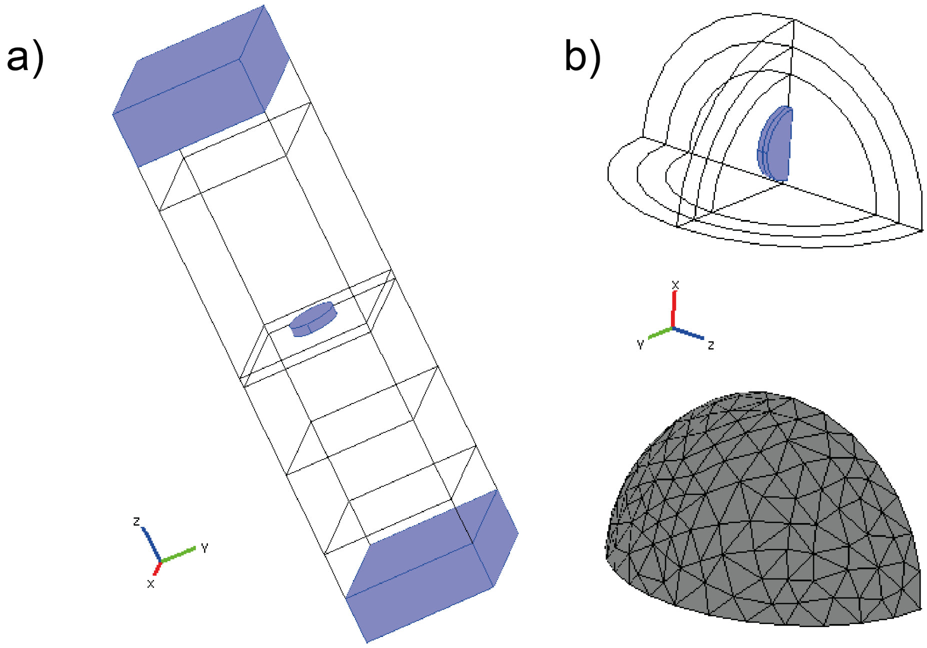

Figure 2.1: a) Comsol geometry for a single gold disk on a two-layer substrate. The disk is coloured blue here, as well as the Perfectly Matched Layers (PMLs) at the ends. b) Geometry for modelling of a coupled disk dimer. Using symmetry considerations allows us to use only one fourth of the computational resources. In the bottom picture, the geometry is meshed.

The Finite Element Method is a very powerful tool to solve partial differential equations at specific node points of a volume. These nodes are determined by the chosen mesh which may restrict resolution. Obviously, a simulation with fewer mesh elements is going to solve faster than one with a finer mesh. It is very important to make sure the mesh is chosen detailed enough in order for the solution to converge. On the other hand, a finer mesh than necessary for convergence will take an unnecessarily long time to solve. In Fig. 2.1, an example of the modelling geometry most commonly used in this thesis is given. On the left, we see a rectangular geometry for simulation of a single gold disk on a substrate. The excitation here is defined as a plane wave moving in positive z-direction, with polarisation in x-direction. Two Perfectly Matched Layers (PMLs) limit the geometry at the ends (shaded). Coarsely explained, PMLs are absorbing layers and will attenuate any wave passing through them. They absorb both propagating as well as evanescent fields. In the right-hand panel of Fig. 2.1, we use a spherical geometry with a spherical PML around it to model a nanodisk dimer in vacuum. Since the problem is symmetric both in y- and x-direction (but not in z), we can use symmetry planes and only simulate one quarter of the geometry, which is very useful to save on computational resources.

As for all simulational methods, it is important to make sure the solution is convergent and can be trusted. This is most easily done by comparing simulation results with analytical solutions for simple well-explored particles such as spheres. It can also be useful to compare the results obtained from using different simulation tools. In the following section, an overview is given of how to calculate absorption, scattering and extinction cross sections to retrieve the relevant data from a solved model. This is not restricted to Comsol, but can be used for other simulation methods, too.

The absorption cross section σ_{abs} is calculated either by integrating the resistive heating over the surface area of the nanoobject [75] or by using energy conservation and integrating over the total normal flux on spherical interior boundaries. Likewise, the scattering cross section σ_{scat} is calculated from the near-fields, by integrating the normalized scattered flux on spherical interior boundaries.

The extinction cross section is then indirectly retrieved by adding the scattering and absorption cross section together. It can also be derived from the optical theorem [8] that states that the extinction depends only on the scattering amplitude of the electromagnetic wave in the forward direction. We can thus obtain the extinction cross section $\sigma_{\mathrm{ext,OT}}$ by evaluating the following expression on a point along the symmetry axis of our structure:

$$\sigma_{\mathrm{ext,OT}} = -4\pi \frac{\mathrm{Im}(E_{\mathrm{far},x})}{E_0 k_0}, \tag{2.5}$$

where E_0 is the amplitude of the incoming plane wave and $E_{\mathrm{far},x}$ the x-component of the electric far field. The extinction cross section can also be calculated by integrating the square of the normalized far-field over a sphere of interior boundaries. However, this is an extremely inefficient method, since it involves the integration of a variable that in itself is already a surface integral, which means two surface integrations every time the expression is evaluated.

Although for our purposes we are mainly interested in the extinction cross section of our nanoantennas (due to their size, the main contribution here is scattering anyway), we also check the remaining cross sections to make sure that our results are reliable and reproducible. All these different ways to calculate the cross sections were found to yield results that were in excellent agreement with each other.

2.1.2 Boundary Element Method (BEM)

The Boundary Element Method is a numerical method for solving linear partial differential equations formulated as integral equations [76, 77] and is equally versatile as FEM. Like all other numerical methods to simulate nanoscale scattering of electromagnetic radiation, BEM is based on solving Maxwell's equations self-consistently in homogeneous media, including retardation. This is done by calculating the surface charge densities and surface currents on the nanoobject that are affected by the incoming field [78, 79, 50].

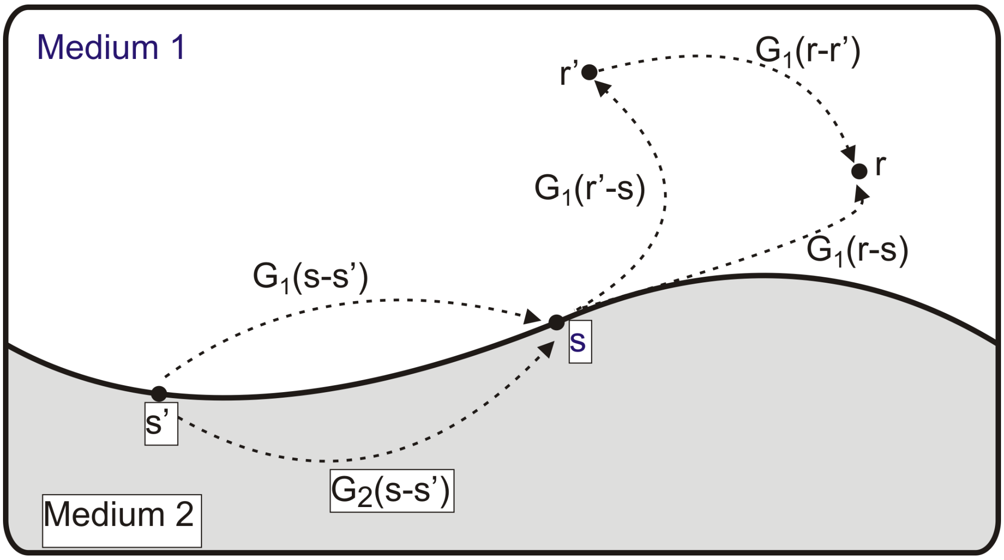

Figure 2.2: Schematics of an arbitrary interface between medium 1 (charge density σ_1, current density $\vec{h}_1$) and medium 2 (σ_2, $\vec{h}_2$). s and s' are typical discretisation points. $\vec{G}_1(r-s)$ is the Green's function that describes the interaction between two points.

In the following, we will give a brief introduction into the theoretical background used for electromagnetic BEM simulations.

Expressing the electric field $\vec{E}(\vec{r})$ and the magnetic field $\vec{H}(\vec{r})$ in terms of the scalar potential ϕ and the vector potential $\vec{A}$ as induced by the external radiation source, we can then proceed to describe $\phi(\vec{r})$ and $\vec{A}(\vec{r})$ inside the surrounding medium j as resulting from an external source in the same medium and the equivalent boundary charges $\sigma_j(\vec{s})$ and currents $\vec{h}_j(\vec{s})$ at a point $\vec{s}$ on the nano-object boundary. This can be written with the Green's function $G_j(r) = \frac{e^{ik_j r}}{r}$ (for illustration, see Fig. 2.2), where $k_j = k\sqrt{\epsilon_j \mu_j}$:

$$\phi(\vec{r}) = \phi^e(\vec{r}) + \int_{s_j} ds\ G_j(|\vec{r}-\vec{s}|)\sigma_j(\vec{s}), \tag{2.6}$$

$$\vec{A}(\vec{r}) = \vec{A}^e(\vec{r}) + \int_{s_j} ds\ G_j(|\vec{r}-\vec{s}|)\vec{h}_j(\vec{s}). \tag{2.7}$$

By discretising the surface boundaries in N such representative points s_i and ensuring the continuities of the parallel and perpendicular electric and magnetic fields, we obtain a system of $8N$ linear equations with 8 unknown surface charges and currents that can be solved. The equations for the polarisability (see previous chapter) then yield the near- and far-fields of the structure which can be calculated in a straightforward way.

The BEM code used in this thesis was provided by the Aizpurua group and is based on axial symmetry, making it one of the most efficient ways to calculate nanorod geometries. The boundary surfaces between different materials are discretised (see Fig. 2.3a) and the

Maxwell equations are solved in integral form at these discrete points. BEM is often more efficient than other methods for modelling the interaction of light with particles with a small surface/volume ratio, since it only solves for discrete points on the surface. For larger or more complex geometries, however, it is often less efficient than volume-discretising methods such as FEM or FDTD.

2.1.3 Finite Difference Time Domain method (FDTD)

The FDTD method, first proposed by Yee in 1960 [80] is based on solving Maxwell's equations on discretised volumes and its use has dramatically increased for plasmonic modelling in the last decade. This method makes use of the fact that the time derivative and thus the evolution of the electric field is dependent on the spatial change of the magnetic field as described by Maxwell's equations. Iteratively solving for E- and H-fields thus simulates the propagation in the system. This is most often done on a so-called Yee-lattice (see 2.3b) with staggered cells for electric and magnetic field components due to its proven robustness, and solved in a step-by-step manner: First, at one point in time, the electric field vector components are solved for the grid, and in the next instant in time, it is the magnetic field components that are solved. This is repeated until the desired field behaviour has fully converged.

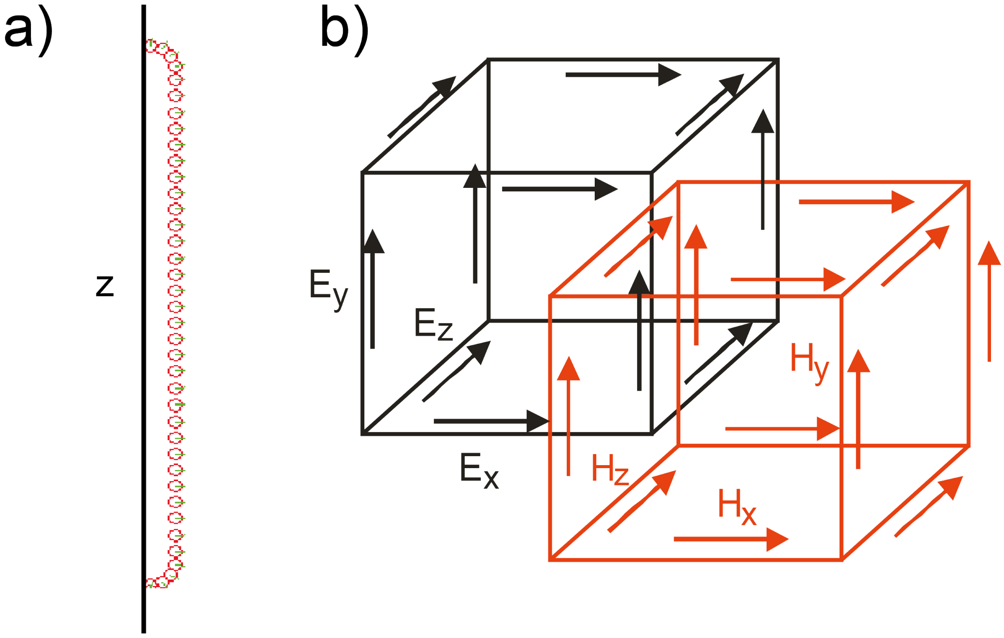

Figure 2.3: a) Typical discretisation scheme using BEM for an axially symmetric structure such as a nanorod here. The red dots are the discrete points used for solving, the green arrows indicate the normals in these points. b) Schematics of a standard cartesian Yee-lattice used for FDTD meshing, where electric and magnetic fields are arranged in lattices with different offsets.

As for FEM, meshing is a critical component of FDTD modelling. The whole structure is meshed in a space grid, and an electromagnetic wave is launched in the direction of the structure, most often a Gaussian pulse. The electromagnetic interactions are then calculated along the grid and result in a modified pulse in the time domain, which can be Fourier transformed into the frequency domain for direct comparison with the spectrum of the incoming wave as it was before encountering the nanostructure. This way, both incoming, outgoing and relative spectra can be calculated.

FDTD is a versatile simulation technique and is very intuitive since it simulates the temporal propagation as we are used to expect it. Animated displays of the propagating light and its interaction with nanostructures can easily be generated using FDTD, and are very useful for our understanding. Since it is a time-domain technique, it is possible to cover a wide range of frequencies with a single simulation run. Additionally, FDTD has the advantage of treating nonlinear properties in a natural way, which is often problematic with FEM and BEM.

2.2 Nanofabrication

In this thesis, we use two different kinds of nanoantennas: Lithographically designed nanorod antennas and disk dimers fabricated by colloidal lithography and angle-controlled deposition. These two techniques will be discussed in detail in this section, as well as deposition techniques to cover them with thin semiconductor layers for activation.

2.2.1 Nanoantenna fabrication by e-beam lithography

In order to fabricate plasmonic nanoantennas, a working and reproducible process had to be developed in the Rapid Prototyping Facility in the School of Physics. This involved optimisation of the different sensitive parameters (such as photoresist treatment and exposure voltage) and resulted in well-resolved nanoantennas of the size of 100 nm × 180 nm, and a gap of 20-60 nm for the individual antennas (see Fig. 2.5). The quality is sufficiently homogenous on a μm scale and the process itself is reproducible. Adjusting the dose allows for tiny variations in size. In this section, a detailed description of the established fabrication process is presented.

Glass slides covered with ITO were used as a substrate, preventing a charging of the sample during the writing process. The crucial steps are shown in Fig. 2.4. First, the sample was cleaned by sonication in acetone, isopropanol (IPA) and deionised water for 20 minutes each. It was then blow-dried with an air gun. Next, approx. 100 nm methyl methacrylate (MMA) EL6 (6% in ethyl lactate) was spincoated onto the sample and baked for one minute at 150°C. After allowing it to cool down to room temperature, another 50 nm layer of poly-methyl methacrylate (PMMA) A2 (2% in anisole) was

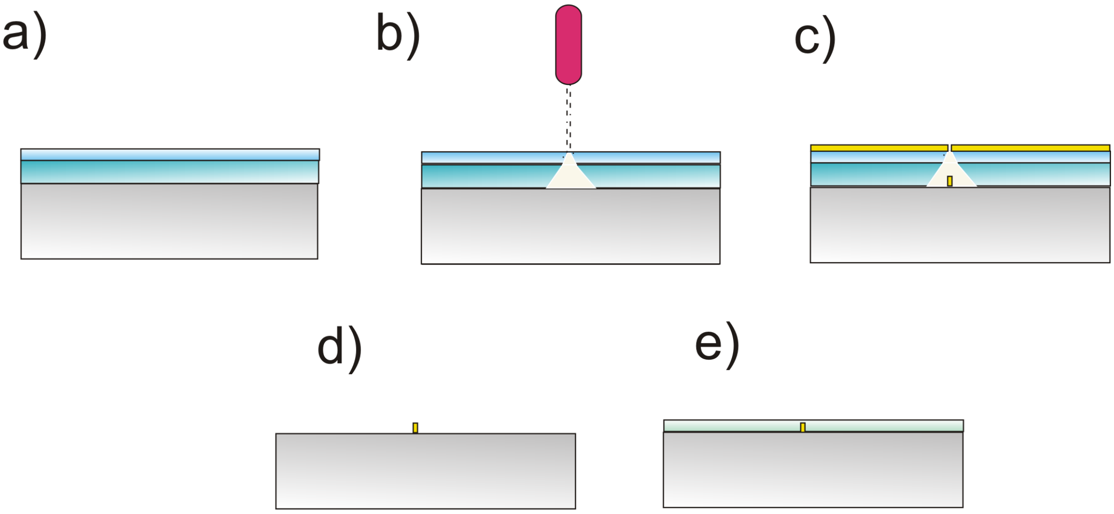

Figure 2.4: a) A bilayer of photoresist is spin-coated onto an ITO-covered glass slide. b) Exposure to the electron beam breaks up the molecules of the photoresist. The affected molecules are dissolved by the developer and any remains are stripped off by plasma-ashering with O_2. c) A thin layer of gold is evaporated onto the sample. d) After the lift-off with acetone, only the gold structures remain and can be coated in the semiconductor (e).

spincoated onto the sample and baked for another minute at 180°C. Using a bilayer of positive photoresist (such as our MMA and PMMA) with different molecular weights (= different sensitivities) is necessary for good resolution. This circumvents the so-called *proximity effect* (backscattered electrons widening the exposed pattern) and makes it possible to obtain sharp edges [81]. On the other hand, the bilayer restricts the size of the gap between the two nanorods forming an antenna to 20 – 30 nm (again due to the proximity effect, see Fig. 2.4 b).

For electron beam lithography, the highest possible EHT voltage of 30 kV and a spot size of 10 nm was used to expose the resist, which also ensured high resolution and

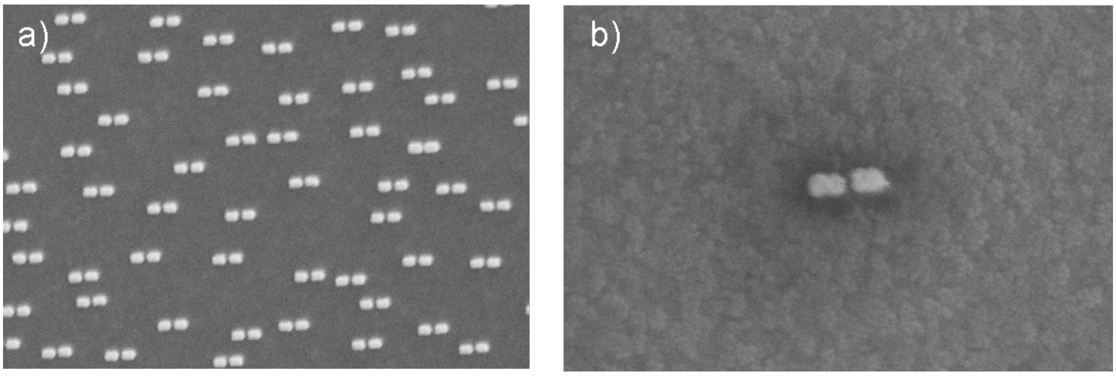

Figure 2.5: a) A pseudorandom array of uniform nanoantennas of the size 100 nm × 180 nm with a gap of 30 nm. b) A single nanoantenna, charged up by exposure during characterisation by SEM. In the background, it can be seen that the highly conductive ITO (8-12 Ω/square) forms crystalline areas.

reproducibility. An exposure dose of 130 μAs/cm^2 was found to produce the best results. The exposed bilayer was then developed in the developing solution MIBK : IPA (methyl isobutyl ketone : isopopropyl alcohol = 1 : 3) at room temperature for 40 s, forming an undercut especially in the bottom layer of photoresist. The development is stopped by rinsing the sample in IPA for 60 s. Before evaporating the gold onto the sample, we plasma asher the sample with O_2 for 10 s to rid it of any residual resist in the developed parts. This step is crucial to ensure a good adhesion of the gold to the ITO. After the remaining photoresist is removed, a 20-30 nm layer of gold is deposited onto the sample.

The final step consists of the lift-off in acetone. The sample was left to soak in acetone for a couple of minutes and cleaned in IPA afterwards, allowing the photoresist covered with gold to come off easily. To obtain hybrid semiconductor-metal nanoantennas (see chapters 5 and 6), the antennas were burried in a matrix of semiconductor. The thin films of approx. 25 nm thickness were deposited by r.f. sputtering, which is described more closely in the following section. The results of the nanofabrication process are shown in Fig. 2.5 for a pseudorandom array, with randomness an a scale of several μm of antennas and, at larger magnification, a single nanoantenna on highly conductive ITO, used for single antenna spectroscopy.

2.2.2 Nanoantenna fabrication by colloidal lithography

Nanofabrication methods using colloids have been developing at a rapid pace during the last 10 years. Colloidal nanofabrication methods have the unique advantage of providing large area coverage, high fabrication speed (unlike e-beam or FIB), uniformity

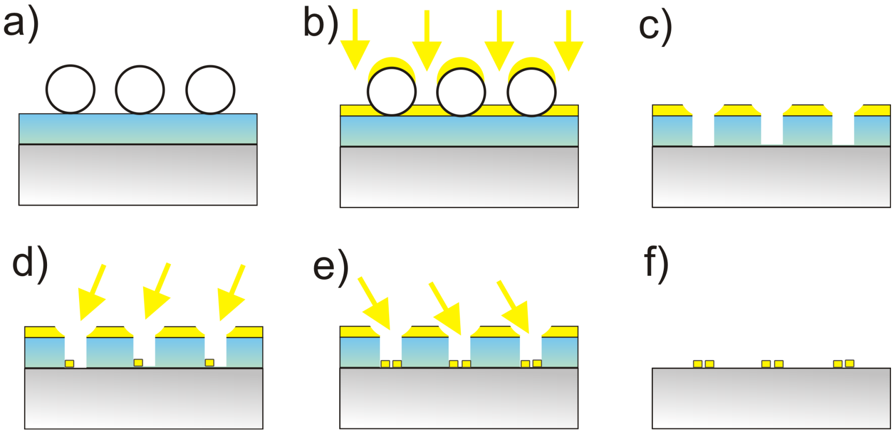

Figure 2.6: Schematic overview of large-area dimer fabrication using colloidal hole-mask lithography combined with angle-controlled evaporation. Deposition of sacrifical photoresist layer and masking colloids [a)] is followed by evaporation of the hole-mask [b)]. After tape-stripping the colloidal spheres, holes are etched into the resist [c)], which is subsequently followed by evaporation at different angles [d), e)]. In the end, the mask is lifted off together with the resist in acetone [f)].

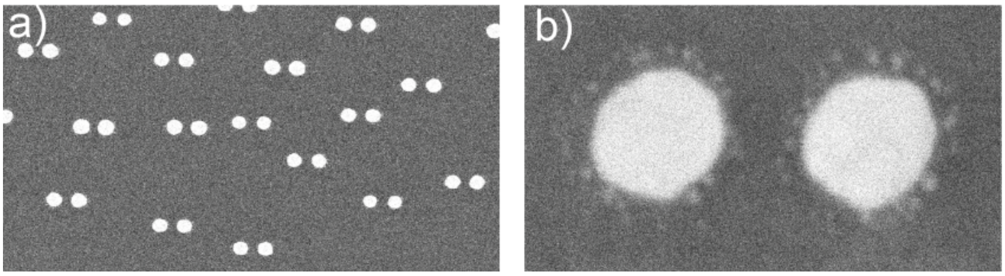

Figure 2.7: a) FEGSEM picture of randomly distributed disk dimers with radius of approx. 100 nm and a gap of 20 nm. b) A single disk dimer in high magnification.

and reproducibility. The simplicity of colloidal fabrication techniques and their economic viability make them highly appropriate for routine nanofabrication. Using self-assembled colloids for mask production coupled with angle-dependent evaporation, a number of different nanostructures have been demonstrated to be manifacturable: splitrings [71], bowtie antennas [70], random disks [82], disk dimers consisting of gold, silver or with arms of different materials (so-called *heterodimers*) [69] are just some of many examples. Here, an overview of the nanofabrication of closely spaced disk dimers is given.

The basic fabrication steps are presented in the schematic overview in Fig. 2.6, following the description from Ref. [68]: First, a sacrificial PMMA film was spin-coated onto the substrate. Charged polymer spheres were then deposited onto the photoresist, which was made hydrophilic by a short oxygen plasma etch. Due to the electrostatic repulsion between the spheres, a random deposition of colloids is achieved, on which the hole-mask made of a thin gold layer is then evaporated. The polymer spheres were stripped away with tape. The spacing and diameter of the holes is determined by the separation distance and size of the polymer spheres. The photoresist below the remaining holes was etched away in an oxygen plasma, resulting in an undercut of the gold mask not unlike after e-beam exposure and development. This hole-mask could then be used to deposit gold at different angles to achieve dimers. This was done at very small angles and in several steps, depositing 5 nm in one direction, 5 nm in the other, and so on. Otherwise, the deposited gold starts to obstruct the holes and deposition of first one dimer arm and then the other would lead to differently sized disks. The last step is lift-off, were the gold on top is disposed of together with the sacrificial resist. The samples were delivered to us before the final lift-off step, so we could do another evaporation step ourselves in order to deposit one more semiconductor disk in the gap (see chapter 6).

2.2.3 Deposition of conductive oxide layers

For hybridisation of our nanoantennas, we deposit thin layers of conductive oxides on top [83, 84, 85, 86, 87, 88]. The antennas used in the experiments in chapter 5 were covered with sputtered ITO after being already fabricated on ITO substrates, thus allowing coverage from all sides. For the activation of the dimer disk metamaterials in chapter 6, we compare sputtered ITO layers with evaporated and post-annealed ITO and atomic layer deposited aluminium-doped zinc oxide (AZO).

2.2.3.1 Fabrication and analysis of thin r.f. sputtered ITO films

Radio-frequency (r.f.) sputtering is a popular means of depositing material onto a substrate through the oblation of a target due to the impact of high energy ions, in our case argon. With the help of a strong electric field, an argon plasma is created and driven to strike the substrate with a high frequency. Sputtering allows the deposition of not only metals, but also semiconductors and nonconducting materials. Mixing of the inertial gas (Ar) with a reactive gas (e.g. oxygen) allows to deposit an oxide. Here, we look at r.f. sputtering of Indium Tin Oxide (ITO), a n-type semiconductor of high transparency and nearly metallic conductivity with a bandgap of 3.5 - 4 eV [43, 89]. Davenas et al. [89] report band-to-band transitions to be at the origin of the strong absorption observed below 0.35 μm, whereas intra-band transitions resulting from free carrier excitation occur above 1.2 μm.

Over the past few years, intensive research has been done into deposition of highly conductive ITO, see [90]. A very effective technique to get low sheet resistance coupled with good optical transparency has been found to be r.f. sputtering. Substrate temperature, deposition rate, partial gas mixture and pressure have a strong influence on the qualities of the resulting films [91, 90] and have to be chosen with care. In Table 2.1, an overview of different parameters is presented together with the sheet resistivity of the resulting films.

For ITO deposition, the target consists of a circular disk of an alloy with a (90 : 10) mixing ratio of indium oxide : tin oxide. An argon flow of 136 sccm combined with an oxygen flow of 1 sccm yields films with good electrical characteristics. This was found by Dr Peter Ayliffe in the framework of the ‘mesophotonics’ spin-off. Optimising the sputtering process with regard to temperature and time left for cooling of the sample, values of up to 20 Ω/sq were achieved. The most critical parameter (apart from the oxygen and argon flow ratio) appears to be the temperature. This is attributed to some annealing taking place at high temperatures during the sputtering or during the subsequent cooling down of the sample. The results for different conditions can be found in Table 2.1. The resistivities were obtained using a 4-point probe setup (Jandel) that sends a current through two metal tips and uses another two metal tips (all equally spaced) to measure the induced voltage in between. The thickness of the films is 200 nm (±5 nm) for all films.

Sample	Temp. [°C]	Power [W]	Ar flow [sccm]	O_2 flow [sccm]	Wait [s]	Annealing (1h)	Resistivity [Ω/sq]
1	0	100	6.5	0	0	No	15.5k - 91.19k
A	350	250	136	1	3230	No	58.66, 60.55
E	350	250	136	1	1430	No	57.79, 57.8
M	400	250	136	1	1430	No	33.26, 31.7
T	340	250	136	1	1430	No	64.46, 60.09
S	300	250	136	1	1430	No	161.87, 162.30
F	450	250	136	1	1430	No	27.12, 26.75
Ref	300	250	136	1	1430	No	27.52, 28.05
U	490	250	136	1	3000	No	23.77, 21.19
E1	350	250	136	1	1430	in air at 200 °C	55.70, 56.9
E2	350	250	136	1	1430	in air at 300 °C	234.61.61, 205.62
E3	350	250	136	1	1430	in air at 400 °C	403.42, 409.8

Table 2.1: Resistivity of thin ITO films sputtered under different conditions, such as temperature, power, partial pressure, wait for stabiliation of the flows, annealing gas and times.

We have also tried to achieve even lower sheet resistances with the help of post-annealing. According to literature, annealing conditions strongly affect the properties of the films. Improved conductivity and optical transparency has been reported for annealing in air [92], oxygen [93], hydrogen [94], and a variety of gas mixtures [90]. For annealing in air, we found the opposite to be true, i.e. a deterioration in conductivity (compare Table 2.1). A likely explanation for this deterioration is that we are already depositing the ITO in an oxygen/argon gas mixture at high temperatures. Waiting for the temperature to drop below 130°C takes approx. 1–2 h, leading to an annealing immediately after deposition.

Best results in literature were obtained for annealing in a forming gas (a mixture of N_2 and H_2) [95, 96]. At the moment, there are no facilities in which to anneal a batch of samples in forming gas; however, the Mountbatten Cleanroom has just begun to put several furnaces into operation, one of which uses forming gas for annealing. Should the conductivity of our ITO films need further improvement, that is one of the options worth exploring in the future.

Making use of the UV/VIS Spectrometer in the Physics Cleanroom (Jasco), the reflectivity and transmittance of the sputtered samples from Table 2.1 and of two batches

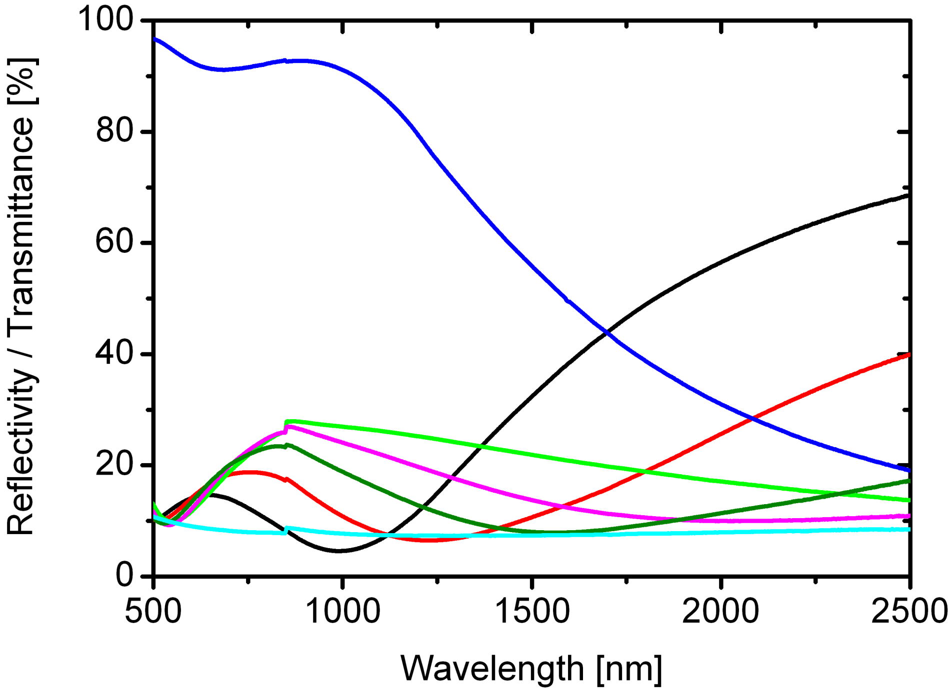

Figure 2.8: UV/Vis reflectivity spectra for Sample M (red), Sample S (magenta), Sample A (olive), Sample 1 (green) and commercial samples of 100 Ω/sq (cyan) and of 12.37 Ω/sq (black), as well as the transmittance for the 12.37 Ω/sq sample (blue). The slight offset in the curves between 800 and 900 nm is due to the gratings in the UV/Vis being changed.

of commercially purchased ITO covered slides with resistivites of 8-12 Ω/sq and 70-100 Ω/sq were measured. The spectra are shown in Fig. 2.8. Using the Fresnel equation with angle zero for the reflectivity between ITO and air as a rough approximation, we can qualitatively describe the behaviour of the measured reflectivity curves:

$$R = \frac{(n-1)^2 + k^2}{(n+1)^2 + k^2} \tag{2.8}$$

For long wavelengths, the absorption coefficient k dominates the reflectivity spectra, leading to an almost metallic behaviour of the ITO films. This behaviour is more pronounced for higher free-carrier concentrations, as can be seen in Fig. 2.8.

2.2.3.2 Other deposition techniques

For coverage of the large-area dimer metamaterials in chapter 6, we also investigated conductive oxide layers deposited by other techniques, in particular by evaporation and subsequent annealing, and Atomic Layer Deposition (ALD), which offer advantages in terms of control over dopants and uniformity.

For evaporation, ITO grains (90-10 wt%, 99.99 % pure from Testbourne Ltd.) were heated in a ceramic crucible at 2×10^{-4} mbar partial oxygen pressure and subsequently annealed in air for 1h at 200°C. As can be seen in Fig. 2.9, the evaporated ITO forms a smooth film on the gold dimers, whereas the sputtered ITO forms grains on the substrate. These grains can be found next to the dimers, but also sometimes in the gap between two disks which accounts for and explains the variety in the magnitude of the results presented in chapter 5 and in [97, 98]. The stochiometry of ITO is crucial due to its effect on electrical and optical properties, so smooth and uniform films are desirable.

For ITO, we optimised conductivity for both sputtering (see previous section) and evaporation and came to the conclusion that while both r.f. sputtering and evaporation allow us to reach high sheet resistances of 20-50 Ω/sq for a 200 nm film of good transparency, evaporated films show a much more uniform consistency. Evaporation also has the additional advantage of being directional, unlike sputtering, which makes it possible to use photoresist patterning.

This leads us to another candidate for conductive transparent oxides, Aluminum-doped Zinc Oxide (AZO), which provides the best prerequisites in terms of uniformity. For AZO films, we used ALD, a technique for deposition of thin films that is based on using gas phase chemical processes sequentially. The chemicals are provided in the form of so-called precursors that react with the sample surface to form a self-limiting deposition layer of $\AA$ thickness. The precursor used for AZO deposition were DEZ (diethylzinc) and TMA (trimethyl aluminum).

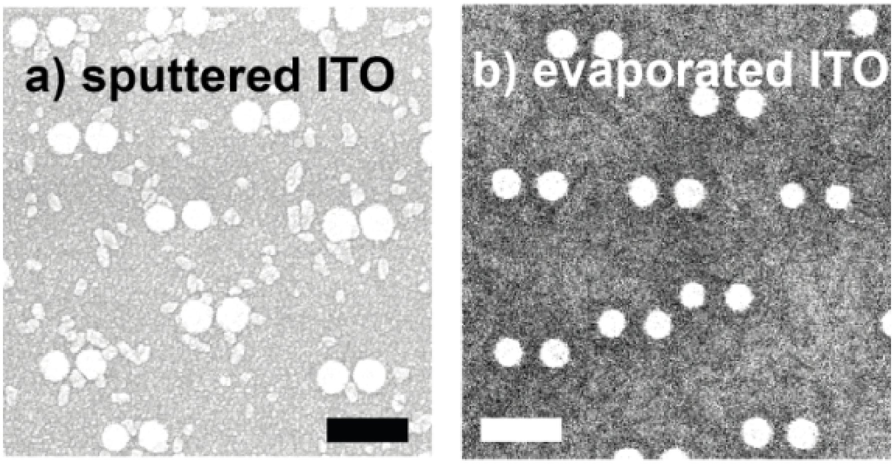

Figure 2.9: FEGSEM pictures of dimer substrate covered in sputtered, respectively evaporated ITO. It is clearly visible that the evaporated ITO forms much smoother layers. The scale bars denote 200 nm. The difference in brightness is simply due to different contrast settings.

For AZO deposition, we used a temperature of 150° and created a layer-by-layer structure consisting of a ZnO matrix and Al_2O_3 dopant layers, with a mixing ratio of 20 cycles of ZnO and 1 cycle of Al_2O_3 for each supercycle, as proposed for optimal resistivity in [99]. ALD is by far the best controlled of the three processes with its controlled growth of single atomic layers, guaranteeing large-area film deposition conformality due to the self-limiting and surface-saturated reaction [100, 101]. Additional advantages include the low deposition temperature and minute control of doping concentration by adjusting the cycle ratio. The only real disadvantages of ALD are its inherent slowness as well as the inability to use patterning by photoresist, since the ALD covers all available surfaces equally.

2.3 Optical microscopy techniques

Two main spectroscopy techniques are used throughout this thesis: Spatial modulation spectroscopy, like the more common darkfield spectroscopy, is used to characterise the linear response of nanoantennas. It has the advantage of being very sensitive to even very small nanoparticles and of yielding a measure directly proportional to the extinction cross section. Pump probe spectroscopy, on the other hand, uses one pulse to excite the antenna, and another one to probe its subsequent femto- to picosecond response, which makes it an extremely sensitive technique for measuring nonlinear responses. Both techniques will be explained in more detail in this section, after we have shortly introduced their application in our setup.

For spectroscopy, we use a Fianium supercontinuum light source [102] with a dual output, picosecond pulses (approx. 4 ps), a maximum overall power of 1 W and a repetition rate of 40 MHz. The first output generates light in the range from 407 – 2000 nm, which is used for spectral characterisation. As shown in Fig. 2.10, the white light supercontinuum from the probe beam is led through a double-prism subtractive mode monochromator, where the beam is first dispersed by a prism and then focused onto a slit for selection of a specific wavelength. Varying the slit width allows to tune the transmitted frequency range with a resolution of up to 20 nm.

A second lens and prism in subtractive mode was used to recombine the different spectral components after filtering. After the prism monochromator, a piezo-mirror was used to spatially modulate the beam before it is thightly focused onto the sample with a NIR objective with 0.5 NA from Mitutoyo.

For the second output, the pump beam, the beam is focussed onto a BBO crystal for second harmonic generation (later substituted by a 5 mm thick KTP crystal for more efficient transformation), generating a green beam of 530 nm. Another modulation, this time of the pump beam, is introduced by a hopper in the pump beam. After the beam passes a delay line in the form of a translation stage, it is focussed through a lens with 0.6 NA onto the sample from the backside.

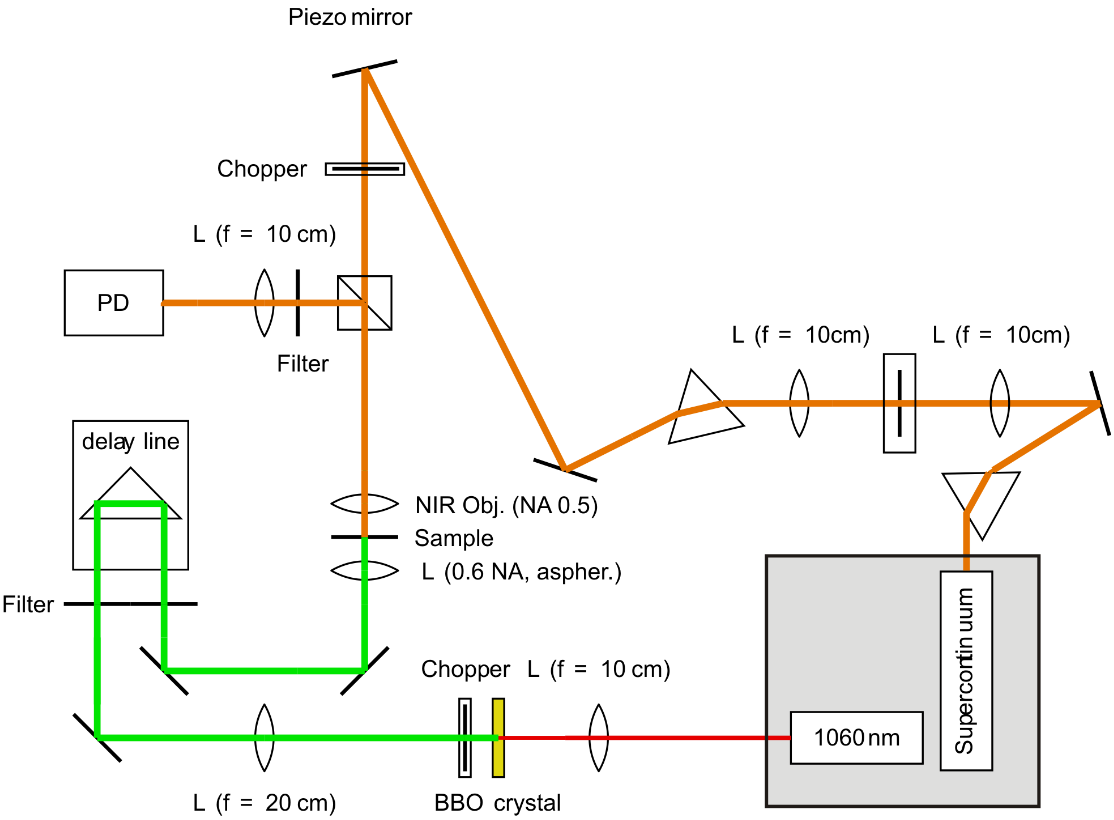

Figure 2.10: Home-built optical setup for spatial modulation microscopy and pump-probe measurements in either transmission or reflection (shown is reflection only since the data for this thesis was measured in reflection).

The probe signal after reflection from the sample back through the objective is measured by reflecting the signal off a beamsplitter in the probe beam path onto a photodetector. This setup allows to measure either in reflection or transmission, in which case the beamsplitter and photodetector are transferred onto the other side of the sample, along with various filters. The measurements presented in this thesis were almost all done in reflection, due to the straightforward separation of pump and probe light components and better signal-to-noise ratio compared to transmission. Both the spatial modulation of the probe beam by the piezo-mirror and the integrated delay line in the pump beam path for pump-probe measurements will be explained in more detail in the next subsection.

For both techniques for linear and nonlinear characterisation, another chopper was used in the beam path of the probe, see Fig. 2.10, in order to provide a reference signal and normalise the differential signals obtained from spatial modulation and pump probe.

2.3.1 Spatial modulation spectroscopy

Spatial modulation microscopy is a tool for characterising single nanoparticles down to a size of 5 nm [103]. This technique uses the modulation of the cross section of the illuminated particle with respect to the incident beam. In our setup, the incident beam is modulated instead and the sample kept fixed, see Fig. 2.10). The laser beam is assumed to have a Gaussian profile $I(x, y)$ and to be tightly focused, ideally of the order of the amplitude of the modulation [103, 104, 105]. Using a lock-in amplifier, it is possible to only detect the modulated light, which allows to extract information about the wavelength-dependent extinction cross section $\sigma_{\text{ext}}(\lambda)$. To make this clearer, we briefly revise the derivation from [104].

In a first approximation, we can assume the modulation amplitude in x-direction δ_x to be sufficiently small ($\delta_x \ll$ FWHM). Therefore, it is allowed to expand the modulated transmitted power, yielding

$$\begin{aligned} P_t &= P_i - \sigma_{\text{ext}}(\lambda) I[x + \delta_x \sin(2\pi f t), y] \\ &= -\sigma_{\text{ext}}(\lambda) \big[I[x, y] + \delta_x I'[x, y] \sin(2\pi f t) \\ &\qquad + \frac{1}{2} \delta_x^2 I''[x, y] \sin^2(2\pi f t) + ... \big] \\ &\approx -\sigma_{\text{ext}}(\lambda) \big[I[x, y] + \delta_x I'[x, y] \sin(2\pi f t) \\ &\qquad + \frac{1}{4} \delta_x^2 I''[x, y] - \frac{1}{4} \delta_x^2 I''[x, y] \cos(2\pi f t) \big], \end{aligned} \tag{2.9}$$

where the derivatives are all with respect to x and we only consider the first few elements of the Taylor expansion.

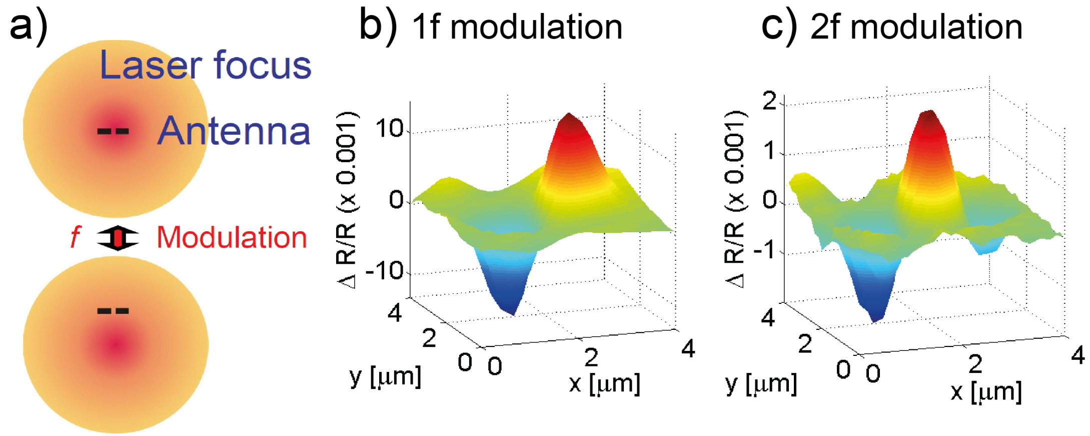

Figure 2.11: a) Principle of spatial modulation microscopy. Depending on the position of the nanoparticle (here a nanoantenna) in the Gaussian intensity profile of the beam, the transmitted/reflected light changes. This makes it possible to detect the modulation with the lock-in amplifier. b) 1f spatial modulation profile of a nanoantenna as used in chapter 5. c) 2f spatial modulation profile of the same antenna.

Detecting a signal on the fundamental ($1f$) or harmonic ($2f$) frequencies with the aid of a lock-in amplifier thus gives information about both extinction cross section, from the amplitude of the detected signal, and the beam size, through the FWHM by way of the derivatives of the Gaussian intensity profile. It is comparatively easy to determine the spotsize of the beam that way, whereas for the extinction cross section it is essential to carefully model Eq. (2.9) numerically to compare with the measured relative transmission change, $\Delta T/T = (P_i - P_t)/P_i$. The same applies for measurements in reflection, where the signal-to-background ratio is approx. a factor of 10 bigger than in transmission because of the lower background intensity.

In Fig. 2.11, we show typical scans as obtained with the Spatial Modulation method for a single nanoantenna. For the $1f$ signal, we obtain the typical form of a first derivative of a Gaussian, whereas for $2f$, it is the second derivative. This is why $2f$ is the preferred signal for spectral characterisation: To be positioned directly on top of the nanoparticle, one only needs to maximise the signal by positioning, instead of at the zero crossing as necessary for the $1f$ signal. Here in panel c), the negative troughs are not of the same magnitude, which is typical if the beam is not perfectly Gaussian – however, this does not have an effect on the maximum of the signal, which is directly related to the extinction cross section. Once positioned at the maximum, it is easy to obtain the full spectrum by scanning the different wavelengths, which is automated now in our setup. We are able to achieve a sensitivity in $\Delta R/R$ of up to 10^{-3} with our setup, comparable to the sensitivities reported in literature [104].

Spatial modulation microscopy is the only known far-field technique that extends to characterising particles of sizes far beyond the diffraction limit. Although near-field methods such as SNOM (scanning near-field optical microscopy) can easily reach comparable sizes when it comes to detection, they are also intrusive and rely on the interaction between particle and environment and the tip. This makes it both harder to interpret the results and fails when it comes to inaccessible geometries such as ours where the nanostructure is embedded in a matrix of semiconductor.

2.3.2 Pump probe spectroscopy

For nonlinear pump probe experiments, we used the same spectroscopy setup (see Fig. 2.10) in combination with a synchronized Ytterbium fibre amplifier, which was frequency doubled to a wavelength of 530 nm. The pump beam is directed into a corner cube in the delay line and then onto the sample from the back (see Fig. 2.10), where its focussed spot is overlaid with the spot from the frequency tunable probe beam. After filtering out the pump beam by a combination of filters and gratings either in transmission or reflection, the signal is measured by a photo diode and fed into the lock-in amplifier. The frequency reference for the lock-in is provided by the chopper in the path of the pump beam.

The delay line consists of a translation stage in the way of the pump beam and allows to change the relative time delay between the arrival of the pulses of pump and probe beam on the sample. If they arrive on the sample simultaneously, the pump creates a large population of excited carriers in the material, thus increasing the reflectivity of the sample for the probe beam. Since both reflectivity and transmittance are functions

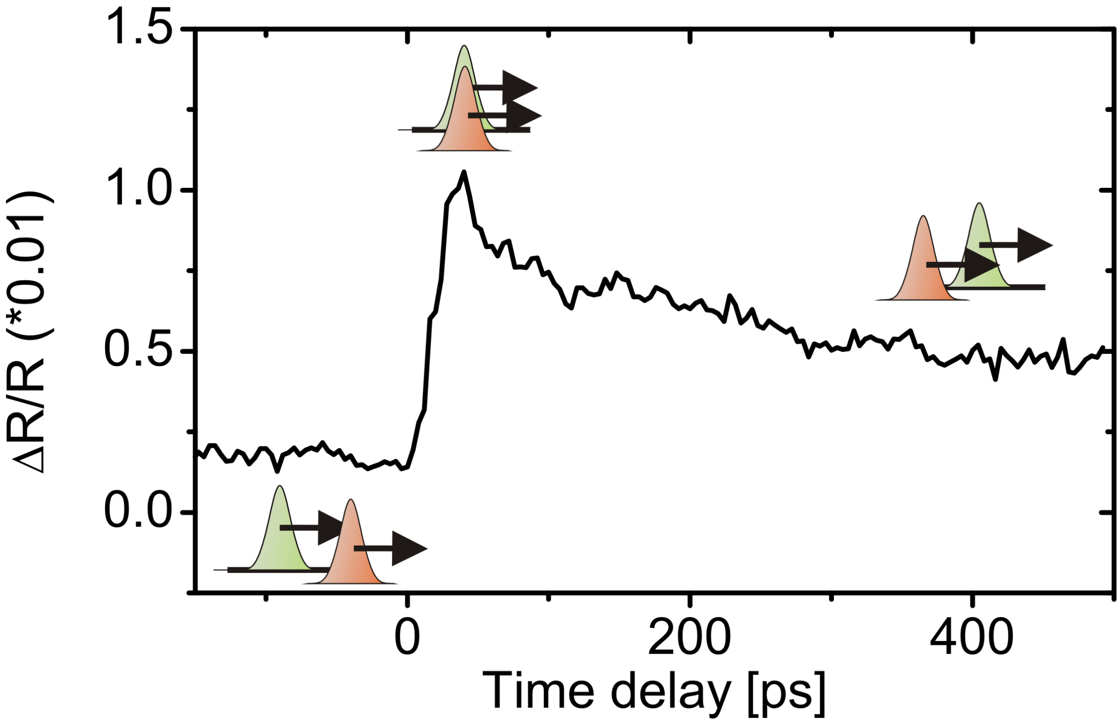

Figure 2.12: A typical pump-probe signal as obtained for ps pulses. The pulses indicate in which order the pump beam (green) and the probe beam (red) arrive.

of the carrier density, the detected power changes when varying the delay time. Taking measurements for subsequent delay times creates a picture of the temporal evolution of the carrier population, see Fig. 2.12.

Pump probe measurements are routinely used for investigations of the dynamics of metals and semiconductors on a femto- to nanosecond timescale. For example, research has been done with pump probe experiments on the recovery of saturable absorbers after excitation, on the diffusion velocity of photoexcited carriers, on phonon modes and coupling, etc. In our case, we do not directly measure the carrier dynamics, but rather the influence of the carrier dynamics on the plasmonic resonance of our optical antennas.

Chapter 3

Localised surface plasmons in coupled nanorods

In this chapter, the far-field and near-field optical response of coupled nanorods is investigated in detail, both in symmetric and asymmetric configuration. As shown in the first chapter, there is a wide variety of plasmonic structures between the limits of propagating plasmons on planar films and localised plasmons on small nanoparticles where the electrostatic limit applies. Here, we present a systematic study of nanorod dimers using BEM calculations and spectral spatial modulation (SM) measurements in order to explore the effects of particle length and separation distance in nanorod dimers. Recently, a lot of interest has also developed into dimers of other configurations, such as nanoshells or nanorings. For example, particularly strong field enhancement in the feedgap has been found in coupled gold nanoring dimers [106].

Capacitively coupled nanorods are of particular interest because of the high field enhancement generated in the gap, which can be used to enhance fluorescence or quantum dot emission [107, 108, 109], for instance. This enhancement is caused by the interaction of the localised plasmons along the rods on the one hand and the interference of the electromagnetic fields they generate on the other hand. A number of different geometrical configurations has been explored in the past, such as putting one rod at an angle to the other or aligning rods in parallel [110, 111, 112, 113]. More recently, coupling between dipolar and quadrupolar modes of two nanorods has been shown to exhibit Electromagnetically Induced Transparency [114, 115, 116]. EIT is a well-known example of destructive interference between excitation pathways in quantum and classical oscillator systems. One such system will be explored in the second half of this chapter in the form of asymmetric nanorod dimers, where higher order mode interference and EIT will be demonstrated.

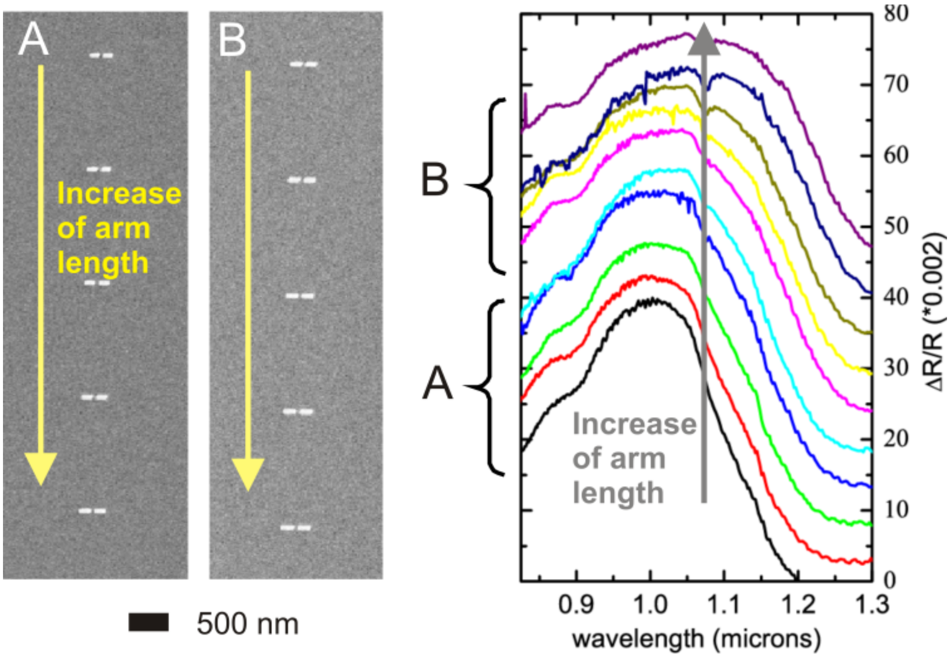

Figure 3.1: Measured SM spectra in reflection of coupled dimers with increasing arm lengths from 250 nm to 350 nm, a width of 100 nm and a fixed gap of 25 nm, grown on a 20 nm ITO substrate, with corresponding SEM pictures of the 10 antennas with increasing lengths in the left panels. Each spectrum was shifted vertically by approx. 10-20 nm.

3.1 Coupled symmetric nanorods

Nanorods sustain resonances along both axes [117] and exhibit higher order modes for sufficient rod length [11, 118]. They have strong hotspots at the rod ends due to the curvature compared to spheres of the same volume and are tunable over a wide range by varying the aspect ratio.

In Fig. 3.1, we have measured spectra of coupled nanorod dimers designed by e-beam lithography with increasing arm lengths. As for single nanorods, an increase in length leads to a redshift of the resonance, as shown in Novotny's effective wavelength scaling, see chapter 1. For coupled dimers, there is an additional redshift due to the coupling between the rods, depending strongly on the separation distance. For the 10 antennas with increasing length shown in Fig. 3.1, we observe an overall spectral shift of more than 100 nm. The shift is more pronounced for the extinction cross-section than can be seen for the differential signal $\Delta R/R$, since it scales with an additional factor of λ^2, leading to a further increase of the spectra towards longer wavelengths. The spectra where measured using the Spatial Modulation technique introduced in the previous chapter, allowing us to spectrally characterise antennas over a wide wavelength range.

3.1.1 The plasmon ruler equation

When two or more metallic nanoparticles are placed next to each other, their behaviour changes from the individual to a collective response [119, 120, 121, 122]. The new coupled structure exhibits its own plasmon modes due to the coupling between its components [123]. These new plasmon modes differ from the plasmon modes of the individual particles and can be understood in terms of the hybridisation model, which is explained in more detail in the next section.

Here, we will look at the effects of coupling between two nanorods of equal length on the resonance wavelength of the redshifted resonance. In Fig. 3.2a), we have calculated extinction spectra for coupled nanorods of 150 nm arm length, including the hemispherical endcaps. We observe that both the cross section and the resonance wavelength increase with stronger coupling. The same is true for the near-field enhancement at the resonance wavelength, as plotted in panels b) and c) for gaps of 2 and 20 nm: We achieve field enhancements up to a factor of 80 for a gap of 2 nm.

For big gap sizes, the shifts of the first order plasmon resonances follows the interaction between dipoles and can be described by an inverse cubic law. For smaller gap sizes, however, the redshift becomes much stronger and increases much faster due to higher-order multipole interactions. The length scaling of the plasmon coupling for small sizes

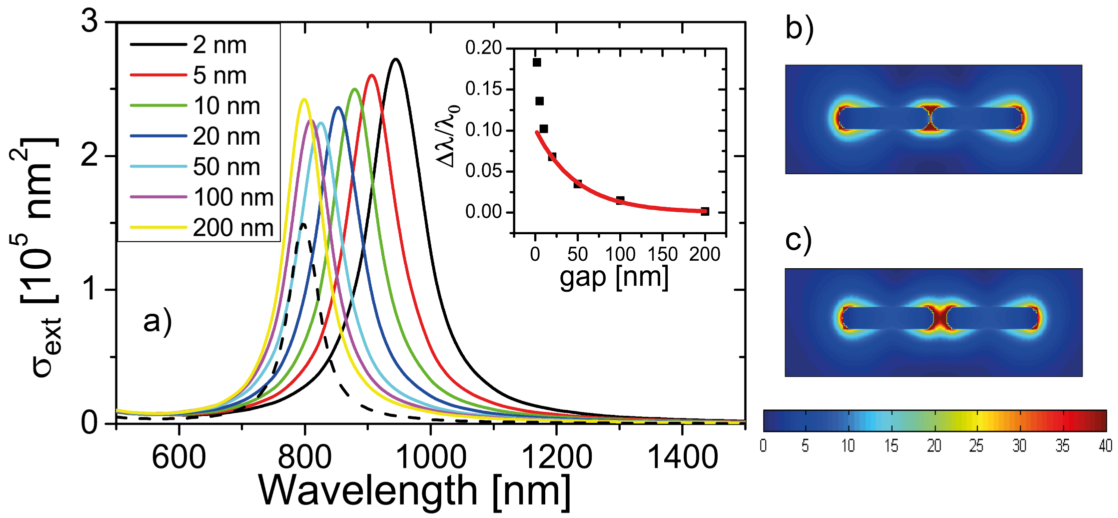

Figure 3.2: a) Calculated extinction spectra for coupled nanorod dimers with hemispherical endcaps and arm lengths of 150 nm respectively (including the endcaps) and decreasing gap sizes from 200 nm to 2 nm, showing a distinct redshift with decrease of the separation [see also inset, where the gap dependence at larger gap sizes is fitted by the plasmon ruler equation (3.1)]. The resonance for a single nanorod (dashed line) is shown as a reference. b) and c) Near-field enhancement for 2 nanoantennas with gap length of 2 nm and 20 nm. We observe a dramatic increase in field enhancement for decreasing gap size.

of the feedgap is well described by a universal exponential dependence on separation, also known as *plasmon ruler equation* [124, 125]:

$$\Delta\lambda/\lambda_0 = \sigma \mathrm{e}^{-s/(\tau l)} \tag{3.1}$$

where λ_0 is the resonance wavelength of an isolated rod, $\Delta\lambda = \lambda - \lambda_0$ the wavelength shift of the nanorod dimer with respect to a single rod, l and s the rod length and gap size, respectively, and σ and τ the two fitting parameters. Interestingly, this scaling law was found to be valid independently of particle shape and size [111, 126, 127, 128, 129].

Even this universal exponential scaling law breaks down for very small gaps (roughly $s/l \leq 0.1$, which in our case means 15 nm), which indicates a different coupling behaviour dominating the strong coupling regime. More elaborate plasmon ruler equations have been introduced to describe the strong coupling between nanoparticles [124, 130, 131]. This regime has attracted great interest, but will not be discussed in more detail here, since this regime is not addressed in this thesis.

For even smaller gap sizes (distances shorter than 1 nm), we enter the quantum regime where deviations such as electron tunneling across the gap and screening [132, 40, 133] occur – phenomena that have been investigated for the first time in a plasmonics context in recent years.

3.1.2 The plasmon hybridisation model

Plasmon hybridisation is a theory that was developed about a decade ago by P. Nordlander and colleagues [134, 135] and which facilitates easy and intuitive understanding of mode coupling in complex plasmonic nanostructures. Plasmon hybridisation is the electromagnetic analogon to the molecular orbital hybridisation picture. The plasmons are treated as incompressible deformations of the charged electron "liquid", while the ions are assumed to be fixed and uniformly distributed. With these approximations, it is possible to get not only a qualitative, but also a first quantitative measure of the plasmonic mode structure, not including retardation [136, 137]. Here, we will not go into detail about the mathematical framework of this model, but simply use the model to intuitively grasp plasmonic interactions in metal nanostructures.

The plasmon hybridisation model has been very successful in explaining the behaviour of increasingly complex plasmonic structures such as, for instance, nanoshells, where the energy splitting is the result of the hybridisation of the plasmon modes of a sphere and a cavity [138]. In the following, we will look at the hybridisation picture for the case of coupling between nanorods of the same arm length as explained in Ref. [139].

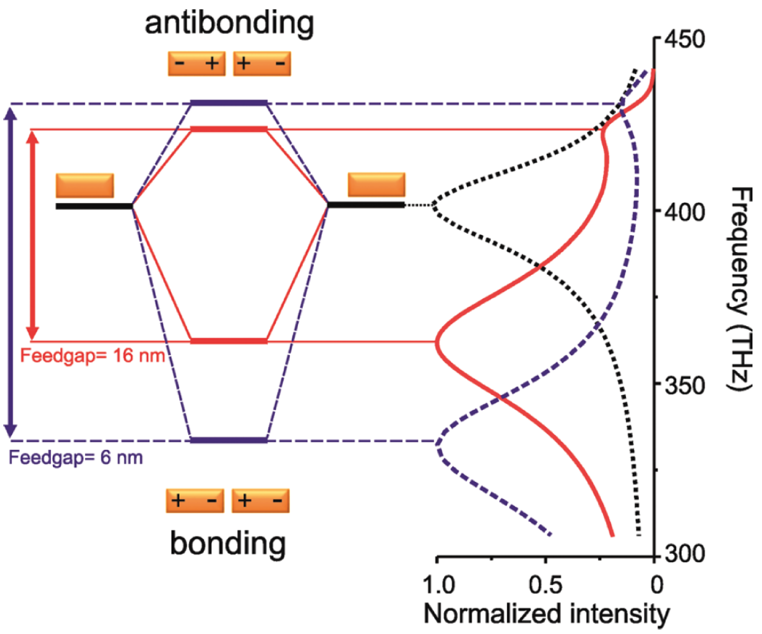

Figure 3.3: Schematic illustration of the energy-level splitting and the corresponding near-field intensity spectra, taken from [139]. Copyright (2010) American Chemical Society. The dependence on the feedgap is very clear in the splitting between bonding and antibonding mode.

Placing two nanorods in close vicinity along their longitudinal axis, we observe a sizable redshift compared to the individual plasmon resonances (see Fig. 3.2). However, there is also a second mode that occurs due to the coupling, which appears at smaller wavelengths.

Fig. 3.3 shows the plasmonic energy-level diagram of two coupled nanorods excited along the longitudinal axis in terms of the hybridisation picture combined with their spectral response. As expected, we observe a splitting due to the mode coupling: At lower energies, we obtain the *bonding mode* and at higher energies the *antibonding mode*, referring to the electron oscillations in the nanorods with respect to each other. The energy splitting in such a dipole antenna depends crucially on the size of the feedgap, and increases with reduced gap size.

The antibonding mode is a nonradiative mode, which means that its net dipole moment is zero. Nonradiative modes are also called *dark modes*, since they cannot be observed in scattering experiments with normally incident plane waves. Radiative modes, on the other hand, are called *bright modes*. Dark modes can only be observed once the symmetry is broken, either by the excitation geometry or by the geometrical shape of the structure. In order to see the antibonding mode in Fig. 3.3, the dimer is illuminated with a source placed 100 nm above the center of the gap, and what is plotted in the figure is the local normalised field intensity 5 nm away from the nanorod ends. Addressing and functionalising dark modes in plasmonic structures is particularly attractive because of their relatively high quality factor due to their nonradiative nature, which is ultimately limited by ohmic losses.

In most studies of coupling behaviour, the antibonding mode is neglected since it is nonradiative. Another reason why the dark antibonding mode has rarely been observed experimentally is that the feedgap needs to be very small (below 20 nm) in order to observe the splitting, which is hard to reproducibly fabricate with conventional nanofabrication methods.

In Fig. 3.3, we only look at the first order modes of the nanorods. However, long nanorods sustain a variety of higher order modes [11, 118], both radiative and nonradiative. This will be of significance in the next section, where we look at coupling between nanorods of different lengths.

3.2 Coupled asymmetric nanorods

Recently, coupling between two nanorods of different length has been proposed theoretically [116, 120]. Here, we present a combined experimental and theoretical approach to address the optical response of asymmetric dimers. In particular, we expand the theoretical investigation of interference and coupling of higher-order plasmonic modes corresponding to odd and even multiples of the plasmon wavelength [118, 50, 52, 140].

3.2.1 Higher-order mode interference

Theoretical model calculations were performed using full electrodynamical methods including retardation. In order to obtain detailed agreement with experiments, including effects of the substrate and of the rectangular antenna geometry, the FDTD method was used (Lumerical). More extensive explorations of the parameter space for asymmetric antennas were done using a model system of cylindrical rods in air employing the boundary element method (BEM). For more information on simulation techniques, see chapter 2.

Experimental extinction spectra of selected asymmetric dimer antennas are shown in the right panel of Fig. 3.4, with corresponding FDTD calculations shown in the left panel. The spectra show a marked dependence on gap position, with good agreement between simulations and experiment. The typical resonant features haven been numbered from 1.-5. to relate them with the modes obtained from the model calculations for coupled rods in vacuum shown further below (Fig. 3.5). This comparison allows us to identify both modes 5 and 2 as the fundamental dipole mode ($\lambda/2$) of the short rod, which splits up into two parts (3.,4.) around 420 nm length of the long rod L_2. For $L_2 = 460$ nm, another crossing of modes is observed without the splitting. The fundamental dipole mode for

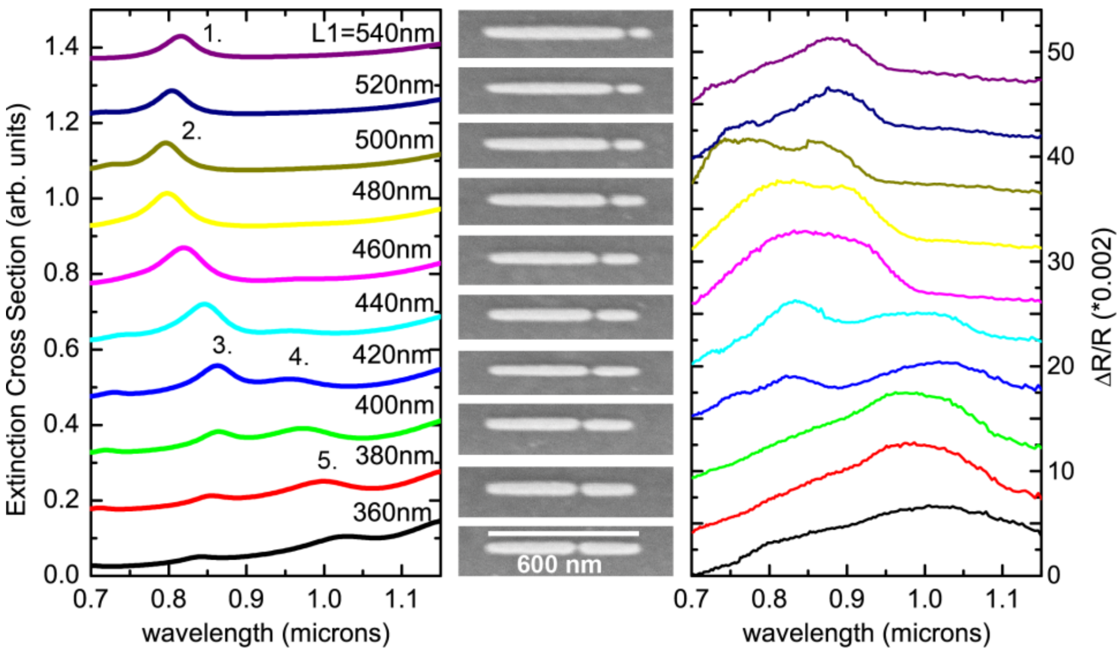

Figure 3.4: Theoretical FDTD (left) and experimental (right) spectra with corresponding SEM images (center) for strong coupling (20 nm gap), with the overall length of both antenna arms kept constant at 600 nm excluding the gap. The length of the long rod varies from 360 nm (bottom) to 540 nm (top), with the length of the smaller rod decreasing accordingly, as shown in the SEM pictures.

the long antenna is located at a longer wavelength, i.e. outside of our experimental window. Mode 1 corresponds to a higher-order bright mode of the long antenna ($3\lambda/2$).

3.2.2 Far-field interference

In Fig. 3.4, we have seen experimentally that the crossing of higher-order modes of the individual nanorods results in a hybridisation of the asymmetric antenna modes. To get a complete picture of the underlying interference and coupling, we numerically investigate the interplay between different multipolar modes depending on the length-length ratio using calculations of the far-field response of an asymmetric antenna surrounded fully by air. Here, the dimer antennas are modelled with BEM as two cylindrical rods with radius $R = 15$ nm with hemispherical endcaps. The total length, including endcaps but excluding the gap, was set to 600 nm as in our experiments. Additional calculations were done also for antennas with a total rod length of 1000 nm, since this reveals the interferences of even higher modes up to $5\lambda/2$.

As a first step towards the modelling of the mode interactions in the asymmetric dimers, we start by individually looking at the modes of each rod. For an overview of the modes present in the individual nanorods, we consider the effective wavelength scaling formula given by Novotny [51] that was introduced in chapter 1.

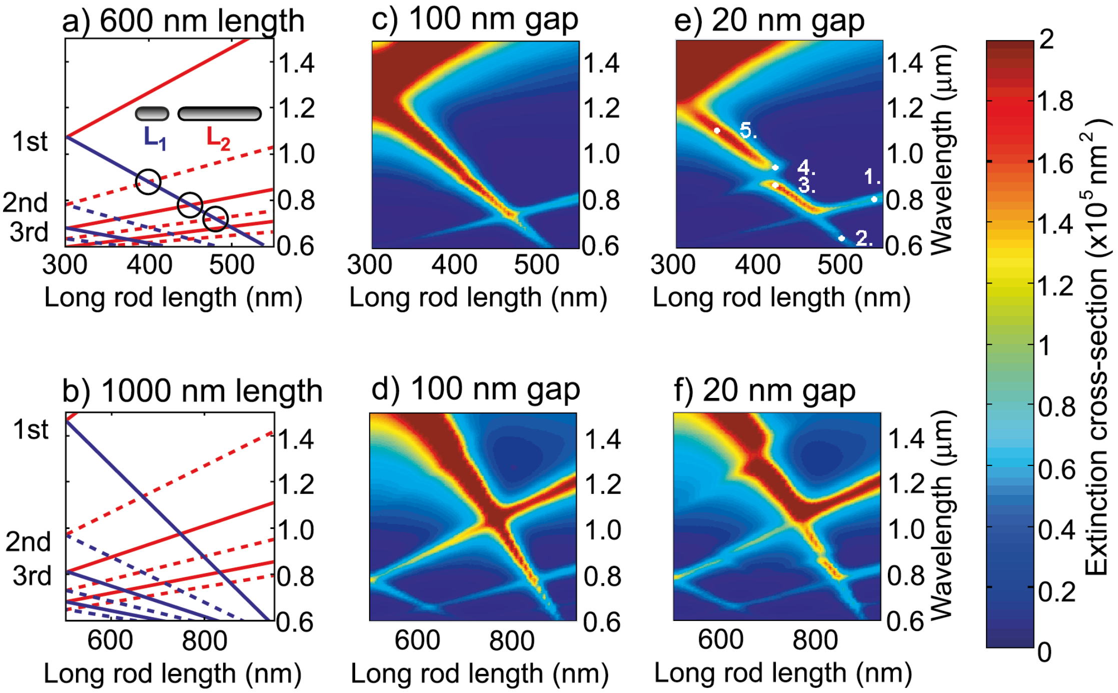

Figure 3.5: Position of the resonances for a dimer of overall length of 600 nm (top left panels) and of overall length 1000 nm (bottom left panels). In panels a) and b), we plot the resonances of order one to six for the individual long and short rods making up the dimer without coupling, according to the scaling law derived by L. Novotny. The modes of the smaller rod are shown in blue, the modes of the longer rod in red. Bright modes are solid lines, dark modes dashed lines. In panels c) and d), we show the results of BEM simulation for varying length ratio between the two rods the dimer consists of. The gap size here is 100 nm (weak coupling), whereas for panels e) and f) the rods are strongly coupled, with a gap of only 20 nm.

Fig. 3.5a) shows the calculated positions for the modes of the individual rods L_1 (short) and L_2 (long) constituting the asymmetric dimer for the case of 600 nm total length. We plot in solid lines the radiative modes and in dashed lines the nonradiative modes. As mentioned before, modes are radiative if they have a nonzero net dipole moment. The dipole moment depends on the order of the mode, i.e. odd multiples of $\lambda/2$ are radiative, even multiples are nonradiative [50]. The modes corresponding to rod L_1 blueshift as the rod length is decreased, while those of rod L_2 redshift because of the increase in length L_2. This leads to the occurence of different order modes sustained by the two nanorods at the same wavelength, which is expected to cause interference. Various crossings between the fundamental mode of L_1 with higher order modes of L_2 are indicated by circles in Fig. 3.5a).

The lines obtained with Novotny's scaling law do not take into account the effect of coupling on the position of the modes, but give an approximate overview of the occuring modes. These interactions are included in the full electrodynamical simulations. Fig. 3.5c)-f) shows full calculation results for the two asymmetric dimer lengths and for two values of the gap between the rods of respectively 100 nm (c,d) and 20 nm (e,f). For the 100 nm gap, where the interaction is weak, the calculations correspond quite well to the expected positions of the individual modes using the simple model. As expected, the dark modes (dashed lines) are not observed in the far-field extinction. Only a small dip is observed around the first crossing point in Fig. 3.5c) and d), which is the first onset of a hybridization between dark and bright modes observed more clearly in Fig. 3.5e) and f). The splitting between points 3. and 4. can be interpreted as interference between the first order mode of the smaller nanorod L_1 and the second order mode of the longer rod L_2, which makes the nonradiative dark second order mode visible and results in a dip in the spectrum. This interference is due to the bright mode being excited and transferring energy to the dark mode of the longer rod, which returns the energy with additional retardation. Both the direct and the indirect scattering paths then interfere destructively and cause the splitting.

For the 20 nm gap dimers in Fig. 3.5e) and f), the most pronounced splittings appear at roughly the length ratios of 1 : 2 and 1 : 4. Another spectral feature we observe here is a coupling between two bright modes, the bright order third mode of the longer

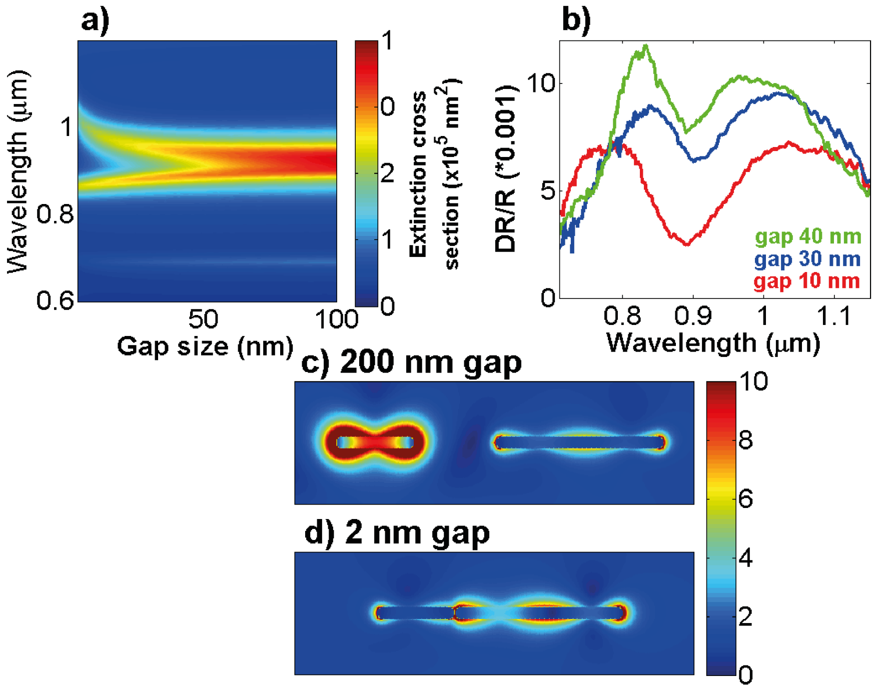

Figure 3.6: a) Extinction cross-section depending on gap size for a dimer with 410 nm and 190 nm rod length. b) Experimental spectra for a corresponding dimer with three different gap sizes. The dispersion at smaller gaps is clearly visible. Below are near-field maps at 910 nm calculated for the same length ratio as in a), with gaps of 200 nm (c) and of 2 nm (d). Even at long gaps such as 200 nm, there is still an excitation of the second-order mode of the long dimer. For very small gap sizes (d), we observe a quenching of the near-field in the gap and a stronger excitation of the nearfield around the longer rod.

rod L_2 and the first order mode of the smaller rod L_1. Unlike for the bright and dark mode interference, however, there is no destructive interference here, since both modes are radiative and can be excited. Thus, the coupling is completely symmetric and the secondary excitation pathways cancel out – we only observe constructive interference, which serves to make the third order mode more visible.

In Fig. 3.6, we show how strongly the EIT splitting is dependent on the dimer separation. The splitting first occurs at a separation of 50 nm in our case. With decreasing separation distances, we see that the splitting becomes more and more asymmetric. The bonding mode redshifts in cubic dependence of the gap size, as expected for dipolar interaction. The antibonding mode, however, blueshifts more slowly – this is caused by the interaction of the plasmon in the shorter nanorod with plasmons of much higher order in the other rod, as already found in the case of spherical nanoparticle dimers [135]. This behaviour is confirmed experimentally in Fig. 3.6b) for antennas with different gap sizes of 10, 30 and 40 nm.

These splittings correspond to avoided crossings where the coupling between dark and bright modes reveals the existence of dark modes through electromagnetically induced transparency (EIT) [114, 115]. This phenomenon is based on a modification of the radiative mode by the presence of a dark, nonradiative mode, which is excited through near-field coupling with the radiative dipole.

3.2.3 Near-field interference

To investigate the EIT-induced splitting into more detail, we plot both field enhancement and phase of the near fields in Fig. 3.7. The near-field maps clearly show the bonding

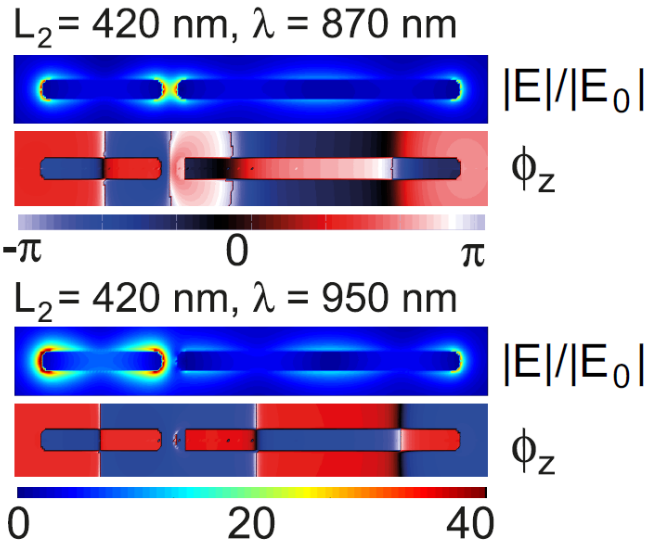

Figure 3.7: Near-field enhancement and phase profiles at the splitting (see numbers 3. and 4. in Fig. 3.5e).

nature of the mode at 950 nm, while the mode at 870 nm shows an anti-bonding profile with zero intensity in the gap. Another feature visible in the phases is the induced charge in the tip of the longer rod caused by the near-field coupling to the bright mode of the short rod. In EIT, the coupling strength is tuned by the distance between the two modes, as can be observed in Fig 3.6a), where we plot the extinction spectrum of the $L_2 = 420$ nm antenna versus gap size. The suppression of the bright mode through coupling with the dark mode is illustrated in Fig. 3.6c) and d). For a large gap of 200 nm, the short antenna shows a strong dipole mode; this mode is completely quenched for a small gap of 2 nm by the coupling. We note that even for a 200 nm gap, the long antenna is excited significantly through far-field dipole-dipole interaction. The influence of this excitation back onto the short antenna requires another dipole-dipole coupling which is concomitantly weaker.

In Fig. 3.8, we take a closer look at the near-field behaviour of our asymmetric antennas. We plot the near-fields for weak coupling (100 nm, upper row) and strong coupling (20 nm, lower row) in the center of the gaps and 5 nm from the endcaps on both sides. Comparing A1) and B1), we see that the radiation of the smaller rod is very much damped by close proximity to the longer rod. Instead of radiating, the energy is transferred to the longer rod, which in turn radiates and retransfers energy back to the smaller rod. The positions marked in these panels depict the further numbering of the panels to the right. In panel A2), we see as expected the blueshift and decrease in linewidth as the shorter rod gets smaller. For weak coupling, there is barely an effect in the center of the gap A3). In A4), we observe the redshift of the long rod as well as the

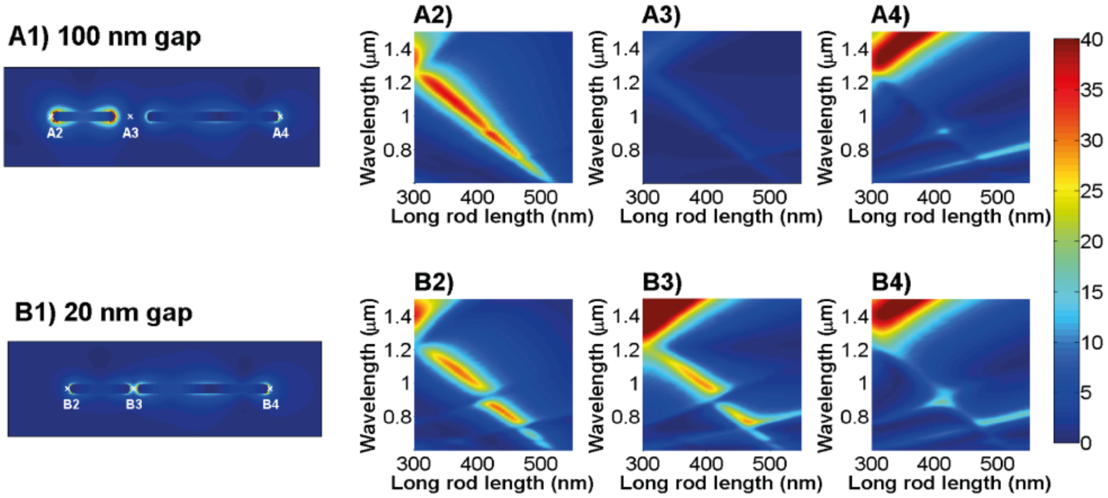

Figure 3.8: Near-field maps calculated at 910 nm for dimers with arm lengths 190 and 410 nm and a gap of 100 nm (A1) and 20 nm (B1), respectively. The top panels depict the near-field intensity for a weakly coupled antenna with gap size 100 nm 5 nm from the short end (A2), in the center of the gap (A3) and 5 nm from the long rod of the dimer (A4). The bottom panels show corresponding calculations for a strongly coupled asymmetric dimer with a gap of 20 nm.

third order mode. There is also a slight increase in field enhancement where first and second order modes meet, an indication that even at gap size 100 nm, our dimers are not completely decoupled.

For strong coupling, the picture gets more lively: Where bright and dark modes meet, we see avoided crossings (compare Fig. 3.5). This is most obvious at 5 nm distance from the endcap of the short rod (B2), but also in the center (B3), where we observe both near-field enhancement and interference from long and short rod. At 5 nm distance from the end of the long rod (B4), the coupling between the dark, second order mode of the long rod and the bright, first order mode of the small rod leads to field enhancement, since the dark mode is excited through the coupling. It is observed that at positions corresponding to the EIT crossing of bright and dark modes, energy is transferred from the short rod to the longer rod. This is of interest for applications, e.g. it would be possible to position a molecule at the end point of the long antenna B3) which will only be excited through coupling of the long rod with the bright mode of the short rod at the EIT condition. Interestingly, there is also an increase of field enhancement where the bright third order mode of the long rod and the bright first order mode of the shorter rod meet. This can be attributed to the larger cross-section of the first order mode and the subsequent radiative coupling.

3.2.4 Conclusion

In this chapter, the coupling and hybridisation of coupled symmetric and asymmetric nanoantennas was investigated. The plasmon ruler equation and the hybridisation model were introduced for coupled symmetric nanorods in order to better understand the coupling behaviour of nanorods. This toolkit is also applicable to asymmetric dimers as investigated in the second part of this chapter. They are a relatively simple model system for studying effects of electromagnetically induced transparency. Three dimensional plasmon rulers consisting of oligomers with coupled dipolar and quadrupolar resonances also exhibit EIT and have been suggested to measure nanoscale distances in chemical or biological matter and resolve time-dependent nanoscale motions [141].

As an extension of the highly successful dimer gap antenna concept, asymmetric dimers may also be of interest for a variety of applications, such as sum-frequency generation, multi-frequency sensors, and Raman scattering [142, 143]. Coupled asymmetric dimers as presented here are also highly suitable to LSPR sensing, due to the high sensitivity of the coupled nanorods to the dielectric environment. Another application for asymmetric nanoantennas which we will explore in the next chapter is that of asymmetric trimer nanoantenna switches for controlling the near-fields, which holds great promise for nonlinear optics and emission control.

Chapter 4

Photoconductively loaded plasmonic nanoantenna switches

As we have seen in previous chapters, metal nanostructures are capable of concentrating optical fields into subwavelength volumes by means of surface plasmon polaritons. Dimer nanoantennas in particular are especially useful in that regard, since the strong capacitive coupling between closely spaced antenna arms leads to strong local field enhancements, easily reaching intensity enhancements of up to a factor 100 at the resonance [109]. The exact position of the plasmonic resonance for nanoantennas is not only tunable by the spacing of the antenna arms, but also depends critically on the dielectric environment. Both influences have been extensively demonstrated experimentally, for instance for vertically aligned nanorods embedded in materials with various refractive indices [144], where the strong sensitivity of the collective plasmon resonances was attributed to the capacitive interaction between the rods.

In this chapter, we propose and explore theoretically a new concept of ultrafast optical switches based on nonlinear plasmonic nanoantennas, which operates on the transition from the capacitive to the conductive coupling regime between the antenna arms by varying the gap loading. This concept is then further developed for systems with interaction between higher order modes, in particular in a trimer system including the asymmetric antennas introduced in the previous chapter. All calculations in this chapter were performed using the boundary element method (BEM) in a full electromagnetic calculation including retardation (for further information, see chapter 2). Part of this chapter is composed of the gap loading calculations in symmetric antenna switches run by N. Large and used in his thesis [145] as well.

4.1 Concept of the photoconductive switch

Active control over subwavelength optical fields is of crucial importance for optical communication, sensing and quantum information technology. Physicists have been trying to achieve all-optical control over plasmons for a long time using different means, such as propagating surface plasmons on planar metal films [146, 147], hole arrays [148], and gold gratings [149]. On a single nanoparticle level, ultrafast heating and coherent vibrations of metal particles have been reported and explained by a spectral shift and broadening of the plasmon resonance [150, 151, 152]. However, these effects are small compared to the resonance itself.

On the other hand, sizable tunability of the antenna by impedance loading of its gap using a dielectric medium has recently been described theoretically [153] and experimentally [154]. The principle is based on the transition from capacitive to conductive coupling between two plasmon modes when bringing two nanoparticles into physical contact [155, 131]. Near-field investigations have shown control over progressive loading of a nanoantenna, which can be understood within the framework of circuit theory [36].

What we propose in this chapter is a related but conceptually very distinct approach using photoconductive loading of the antenna gap. We use photoexcited free carriers to short circuit the antenna arms, leading to a strong modification of both the spectral resonance structure and the near-field mode profile. To that effect, we assume the feedgap to be filled with a semiconductor such as amorphous silicon (a-Si), which allows us to achieve progressive gap loading by varying the free-carrier density through optical pumping. As the plasmonic antenna switch is based on a strong confinement of optical fields in space rather than in time, the antenna switch can operate at a very low switching energy while potentially reaching a much faster response than microphotonic switching devices [156, 157].

The principle of operation of the nanoantenna switch is illustrated in Fig. 4.1. The nanoantennas consist of two closely spaced cylindrical rods with hemispherical endcaps aligned along the same axis as shown schematically. The interparticle gap is loaded with a-Si.

In the unswitched case a), the antenna supports roughly half-wavelength resonances over its individual arms. For antennas in the optical range with gap sizes below 50 nm, these half-wave modes are hybridised into a symmetric combination by the capacitive interaction between the two rods [134]. Fig. 4.1b) shows the response of the same antenna above the free-carrier switching threshold. As the antenna arms are conductively coupled, the antenna now supports a half-wave resonance over the full antenna length. As we will show in this chapter, the conductive gap loading results in strong modifications of both the far-field antenna response and the near-field mode profiles.

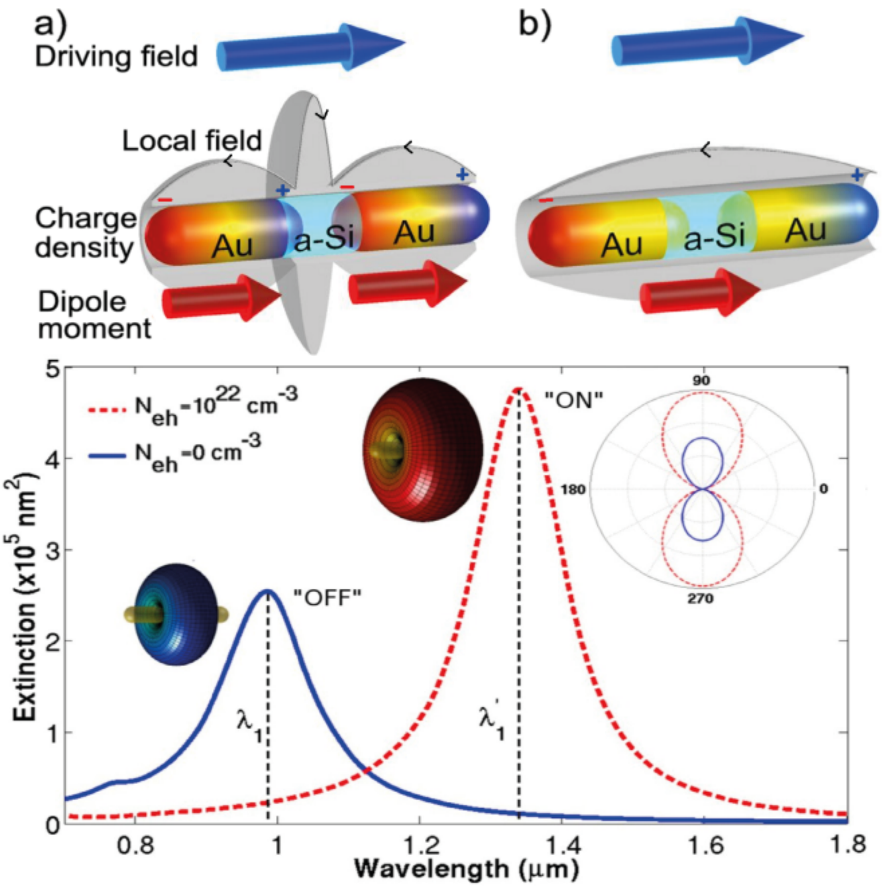

Figure 4.1: Illustration of the principle of antenna switching using a photoconductive gap, showing the fundamental mode of an unswitched (“OFF”) and a switched (“ON”) nanoantenna. We observe a sizable shift of the resonance.

In the lower part of Fig. 4.1, the effect of photoconductive switching on the far-field resonances of a nanoantenna with 100 nm arm length and a gap width of 50 nm is shown, resulting in a dramatic redshift. For this antenna, the capacitive interaction between the two nanorods is relatively weak and the unswitched resonance resembles that of the individual nanorods. Far-field extinction spectra were calculated for free carrier densities N_{eh} below (0 cm^{-3}, solid blue) and far above (10^{22} cm^{-3}, dashed red) the switching threshold. The unswitched antenna shows a strong resonance at a wavelength λ_1 of 980 nm, which can be attributed to the fundamental dipole modes of the uncoupled antenna arms [50]. Photoconductive switching induces a shift of the resonance position from λ_1 to λ_1' over 350 nm, or a relative shift $(\lambda_1' - \lambda_1)/\lambda_1$ of 36%. This switching effect is many times larger than that typically observed using dielectric loading [148, 154]. Calculated far-field radiation patterns corresponding to the two resonances of the unswitched and switched antenna are shown in the inset of Fig. 4.1. As both resonances correspond to a dipolar mode, no change is observed in the angular distribution pattern apart from an overall increase in radiative efficiency. As the radiated power is roughly proportional to the particle volume squared, this increase can be attributed to the addition of the photoconductive segment to the total antenna size.

4.2 The Drude model for semiconductors

The Drude model is routinely used to describe the optical behaviour of metals, as we have seen in chapter 2. The model assumes that the electrons in the valence band of such materials behave as a free electron gas, oscillating around the fixed lattice of ions. This is also applicable to the description of semiconductors where big amounts of electrons can be generated by optical excitation on the femtosecond to picosecond scale.

For use in our plasmonic nanoantenna switches, we choose amorphous silicon (a-Si) for its large electronic bandgap of 1.6 eV, high free-carrier nonlinearity, and further for its wide application range and compatibility with many technological processes [158]. The nonlinear optical response of crystalline silicon has been shown to be dominated by free carrier absorption, with a much weaker contribution from gap filling and band structure renormalization [159, 160]. As similar arguments hold for a-Si, we have calculated the dielectric function $\tilde{\epsilon}(\omega)$ of photoexcited a-Si by combining the experimental dielectric function $\tilde{\epsilon}_{\text{exp}}$ taken from Aspnes et al. [161] with the free-carrier Drude response [159], resulting in

$$\tilde{\epsilon}(\omega) = \tilde{\epsilon}_{\text{exp}}(\omega) - \left(\frac{\omega_{\text{pl}}}{\omega}\right)^2 \frac{1}{1 + i\frac{1}{\omega\tau_D}}\,, \tag{4.1}$$

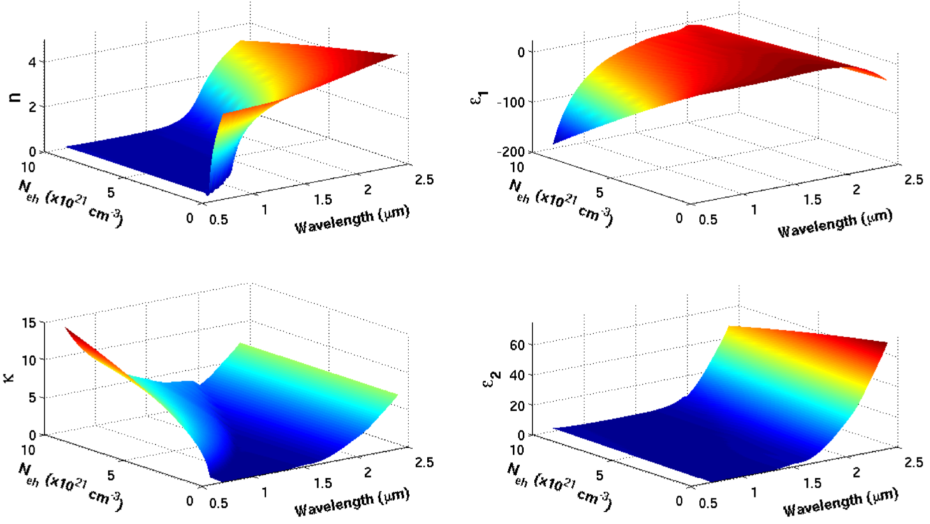

Figure 4.2: Real (*top*) and imaginary (*bottom*) part of the refractive index (*left*) and the equivalent dielectric function (*right*) for amorphous silicon depending on the electron-hole concentration as calculated with the Drude model. The relaxation time is $\tau_D \approx 10^{-14}$ s and the optical mass is assumed to be close to the one for crystalline silicion.

where $\omega_{\text{pl}} = \sqrt{N_{eh}e^2/\epsilon_0 m^*_{\text{opt}} m_e}$ denotes the plasma frequency, with N_{eh} the free carrier density, $m^*_{\text{opt}} = (m_e^{*-1} + m_h^{*-1})^{-1}$ the optical effective mass of the carriers, and $\tau_D \sim 10^{-14}$ s the Drude damping term. The optical effective mass for a-Si, $m^*_{\text{opt}} = 0.17$, is estimated to be close to the value of crystalline silicon [159]. The dielectric function $\tilde{\epsilon}(\omega)$ was calculated using Eq. (4.1) for values of the free-electron density N_{eh} ranging from 0 to 10^{22} cm^{-3}. Fig. 4.2 shows the real and imaginary part of the refractive index, respectively the dielectric function of a-Si depending on the free electron concentration. For values of N_{eh} above 10^{21} cm^{-3}, a strong modification of the refractive index occurs corresponding to the formation of a free-carrier plasma. A critical density N^{crit}_{eh} can be defined as the transition from primarily capacitive (dielectric) to primarily conductive (metallic) loading of the antenna gap, given by the condition $\text{Im}(\sqrt{\tilde{\epsilon}}) > \text{Re}(\sqrt{\tilde{\epsilon}})$, or equivalently $\text{Re}(\tilde{\epsilon}) < 0$. This condition yields an expression for the critical density

$$N^{\text{crit}}_{eh}(\omega) = \frac{\text{Re}[\tilde{\epsilon}_{\text{exp}}(\omega)]\epsilon_0 m^*_{\text{opt}}}{e^2}(\omega^2 + 1/\tau_D^2)\,. \tag{4.2}$$

The critical threshold depends quadratically on the optical frequency ω, while the influence of τ_D becomes prominent for $\tau_D < 1/\omega \sim 10^{-15}$ s, where it results in an overall shift of N^{crit}_{eh} to higher carrier densities.

4.3 Gap loading behaviour in plasmonic nanoantenna switches

As shown before, the idea of transforming nanoantennas into antenna switches is remarkably simple: The interparticle gap is loaded with a semiconductor. We use the Drude model from the previous section to obtain the dielectric function for different concentrations of free-carriers in the semiconductor.

The nanoantenna used here consists of two closely spaced cylindrical rods with hemispherical endcaps aligned along the same axis, as displayed in Fig. 4.1. We used dimensions as follows: A length of 100 nm for each of the rods (not including the endcaps), with a radius of 20 nm and varying gap widths (see simulations for different gap sizes in Fig. 4.3). There is no substrate in any of the simulations presented here, since we are looking at concepts primarily. Additional dielectric substrates are added easily enough in the simulations, as done for the numerical simulations accompanying the chapter on a realization of the antenna switches in the form of ITO-nanoantenna hybrid devices (see chapter 5).

The progressive conductive loading is explored in Fig. 4.3 for antennas of increasing gap dimensions. The horizontal dashed white lines show the position of the unswitched and the fully switched antenna resonance, the dashed white curve indicates the strongly wavelength-dependent switching threshold for the critical carrier density, which can be

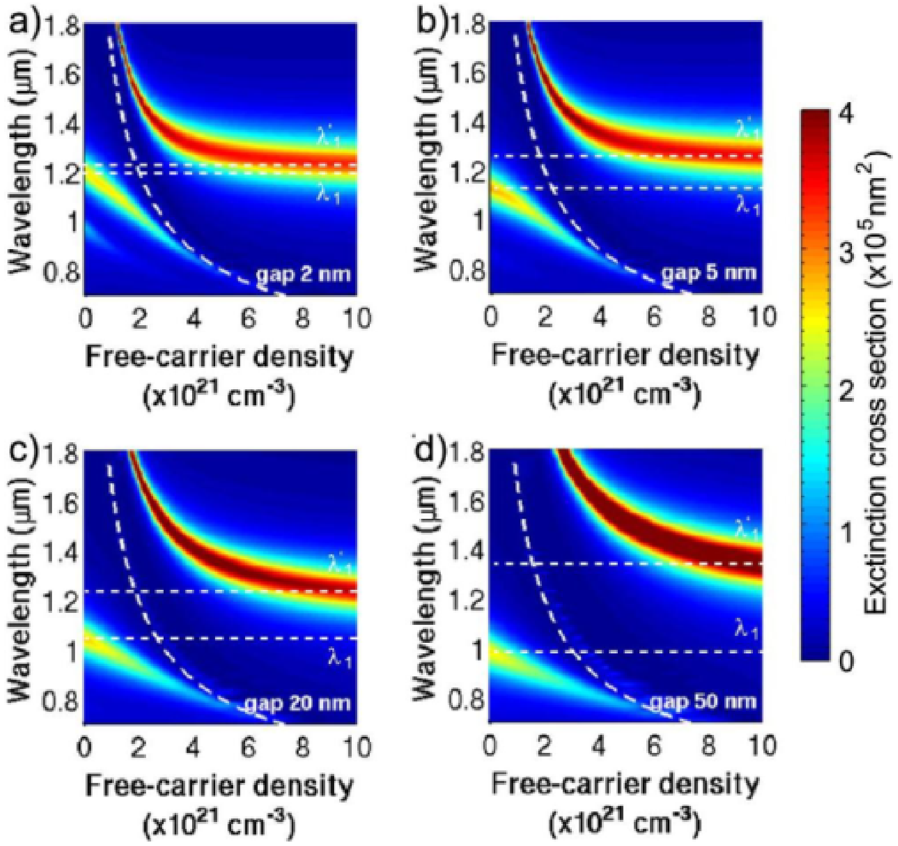

Figure 4.3: Colour density maps of the antenna spectral response as a function of the photoexcited free-carrier concentration for antennas with gap sizes 2 nm (a), 5 nm (b), 20 nm (c), and 50 nm (d).

obtained by the condition $\kappa(\omega) > n(\omega)$. The biggest shift of $(\lambda_1' - \lambda_1)/\lambda_1 = 36\%$ is obtained by the antenna with 50 nm gap width, which can be understood by the large change in antenna volume caused by the photoconductive bridge. Also, the redshift of the antenna arms in the unswitched state is only small, since the capacitive coupling at a distance of 50 nm is comparatively weak.

The general behaviour of the dynamics with increasing free-carrier density can be understood using basic circuit theory [153, 36]: In the unswitched state, the positive and negative polarisation charges act as a capacitor. As the carrier density in the feedgap increases, the charges in the endcaps decrease (reduction of the Coulomb interaction), leading to a blueshift of the mode. At some point where the current flow is so large that the capacitive mode can no longer be sustained, the mode gets damped and dies out.

The appearence of a new resonance at longer wavelength above the critical density line denotes the transition from the capacitive to the conductive regime in the cavity. Starting from the fully switched antenna at $N_{eh} = 10^{22}$ cm^{-3}, on the other hand, we see a redshift and a noticable decrease in linewidth of the mode when the carrier concentration decreases and the gap becomes less conductive. Since having positive charges in only one of the uncoupled antenna arms (as expected for the carrier distribution of one long dipole antenna) and negative charges in the other is physically impossible, we observe the mode redshifting dramatically before it dies out [131, 36]. The narrow spectral profile indicates a reduced damping of this mode, which is interesting in itself. The strong dispersion of the modes allows the antenna to simultaneously sustain the switched and the unswitched mode at the same time in different parts of the spectrum, which holds interest for potential device applications.

In Fig. 4.3, we show the gap loading in symmetric nanoantenna switches for 4 different gap sizes: 2, 5, 20 and 50 nm. For an antenna with a very small gap such as 2 nm, the unswitched capacitive state of the nanoantenna switch with its strong coupling already causing a large redshift does not differ very much from the conductive switched state. For a gap of 50 nm, on the other hand, the modes in the two nanorods are virtually uncoupled, with the capacitive interaction being very weak. It is also for this reason that the switching effect is the strongest here, since there is no initial redshift due to capacitive coupling. Another reason is simply the overall length of the antenna once it is switched, which is much larger with a 50 nm gap filled than, for example, a 2 nm gap. The reported large shift between the original mode and the mode in the new, switched

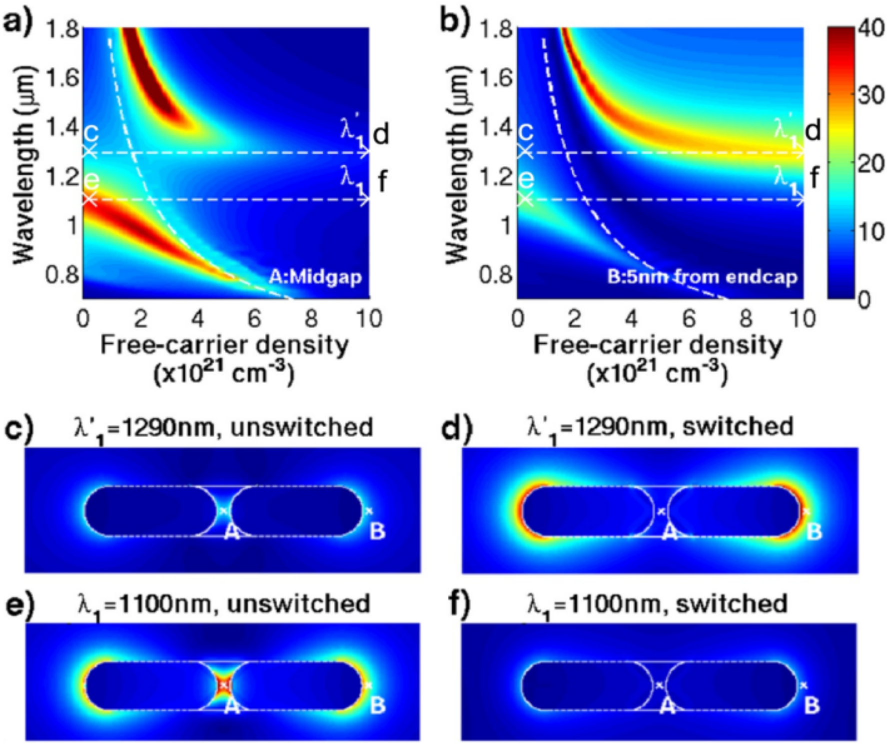

Figure 4.4: Near-field intensity maps calculated for an antenna of $L = 100$ nm arm length, radius $R = 10$ nm and $S = 10$ nm gap size, as function of wavelength and free-carrier density, in the antenna midgap [a)] and 5 nm away from the antenna arms [b)]. c)-f) Near-field intensity maps around the antenna of a) for resonance wavelength λ_1' [c) ,d)] and λ_1 [e),f)], under unswitched ($N_{eh} = 0$ cm^{-3}) [c),e)] and switched ($N_{eh} = 10^{22}$ cm^{-3}) [d),f)] conditions.

configuration holds a lot of promise for a number of applications even beyond ultrafast optical switching, the holy grail of nanophotonics at the moment.

In Fig. 4.4, the near-field intensity is plotted at two positions around an antenna with a 10 nm gap, in the center of the gap (position A) and 5 nm away from the end (position B). This antenna sustains a fundamental mode at $\lambda_1 = 1100$ nm and a high local intensity enhancement of a factor of 35 in the center of the gap at that wavelength. In panel a), the spectral dependence of the near-field enhancement on the free-carrier density in the midgap is plotted. The original mode blueshifts and dies out, whereas the second, switched mode is only sustained up to a density of $N_{eh} = 6 \cdot 10^{21}$ cm^{-3}, before the midgap is completely shortcircuited. Here, the semiconductor is still partly dielectric, as the fields in the gap would be completely suppressed otherwise. This transitional regime exists above the critical density line and the near-field enhancement here even exceeds that of the purely capacitively coupled antenna. The physical origin of this strong enhancement lies in the peculiar charge distribution in the antenna during the crossover from unswitched to switched state. In panel b), we observe the dispersion of the modes and the switching behaviour to a longer wavelength λ_1', as we have seen it for the far-fields. In panels c)-f), the mode profiles of the antenna at the two wavelengths λ_1' and λ_1 is plotted for the switched ($N_{eh} = 10^{22}$ cm^{-3}) and the unswitched ($N_{eh} = 0$ cm^{-3}) state. The mode at λ_1 is strongly quenched in the midgap by the photoconductive switching, due to the redistribution of charges associated with the suppression of the gap capacitor. The newly formed mode at λ_1' has its near-field intensity concentrated at the end points of the antenna and no intensity enhancement in the gap. Active manipulation of the local near-fields around plasmonic structures as presented here will be of interest for nonlinear optics and Surface Enhanced Raman Scattering (SERS) [162], quantum emitters [163], and coherent control [164]. In order to still be able to use the capacitive coupling between rods and the large field enhancement in the feedgap, it might be useful to combine two plasmonic nanoantenna switches as presented here and thus have a longer antenna in the fully switched state, which would leave the midgap free for deposition of an emitter.

For the rational design of antenna switches we define figures of merit of antenna performance for respectively far-field extinction and near-field intensity enhancements. For applications requiring large spectral shifts and extinction contrast, we calculate the relative resonance shift $(\lambda_1' - \lambda_1)/\lambda_1$ and the on-off extinction ratio $\sigma_{\text{on}}/\sigma_{\text{off}}$ at λ_1 and λ_1'. For the near-field switching, key parameters of interest are the on-off ratios of the local intensity at the midgap and antenna end positions A and B, respectively. Resulting values are shown in Fig. 4.5a),b) for the antennas with various gap sizes. The increasing capacitive loading for decreasing gap width S drives the individual particle resonances λ_1 towards that of the half-wave antenna λ_1' [162], resulting in a reduced far-field switching performance. Therefore, for far-field switching, antennas with a large gap are favorable for achieving a large spectral shift and high switching contrast. We should bear in mind

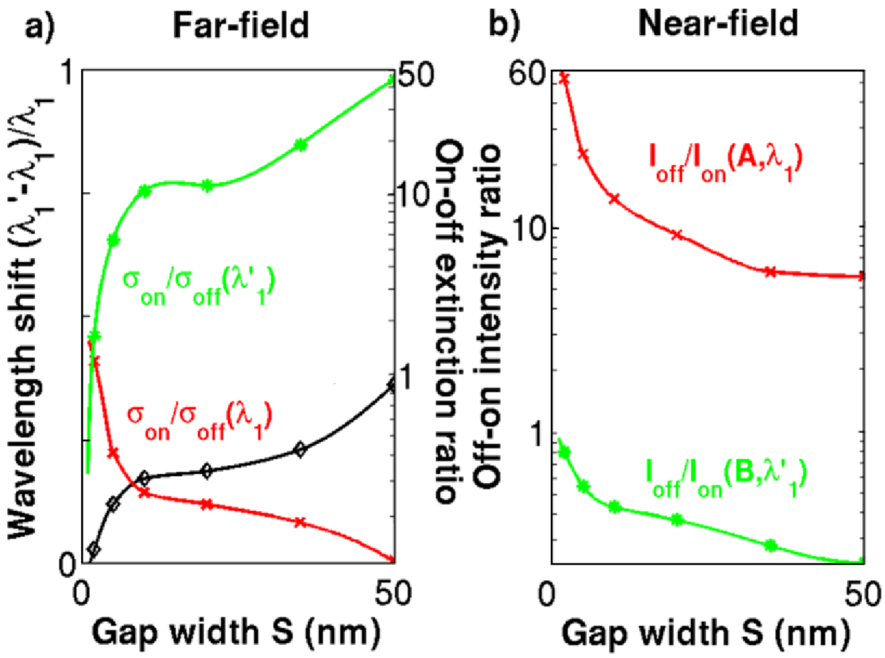

Figure 4.5: Figures of merit for switching operation for operation in a) far-field and b) near-field. Panel a): Relative resonance shift $(\lambda_1' - \lambda_1)/\lambda_1$ (left scale bar) and on-off extinction ratio $\sigma_{\mathrm{on}}/\sigma_{\mathrm{off}}$ at wavelengths λ_1 and λ_1' (inverse off-on ratio), against antenna gap width S. Panel b): Near-field intensity off-on ratios $I_{\mathrm{off}}/I_{\mathrm{on}}$ at λ_1, point A (midgap) and λ_1', point B (5 nm from tip, inverse off-on ratio).

though that antennas with a large gap require more energy for switching and do not benefit as much from reduced switching thresholds at antenna resonances. For the near-field switching, antennas with a narrow gap are more favorable as they produce higher local field enhancements. As mentioned earlier, active manipulation of the local near-fields around plasmonic nanoantennas will be of importance for applications involving coherent control over local field amplitudes and phases [164] and for active manipulation of quantum emitters [163].

4.4 Merits and practical considerations

The free carrier densities required for nanoantenna switching at near-infrared wavelengths are higher than those in the terahertz range [165, 166]. However such densities are routinely achievable using ultrafast laser excitation of an electron-hole plasma [159, 160]. In order to compare the switching energies required for photoconductive antenna switching with state-of-the-art microphotonic devices, we estimate the pumping energies for direct and 2-photon optical excitation. In this estimate, we do not consider dynamical effects occurring on the timescale of the optical pump pulse, which will be discussed further below. For pulsed optical excitation on a time scale much shorter than the carrier relaxation process in the system, the free carrier density N_{eh} can be estimated from the incident optical fluence F_0 using [158]:

$$N_{eh} = \frac{F_0}{\hbar\omega}\left[\alpha_0 + \frac{\beta F_0}{2\sqrt{2\pi}t_0}\right], \tag{4.3}$$

where $\omega = 2\pi/\lambda$, α_0 and β are the linear and two-photon absorption coefficients, and t_0 is the time duration of the pulse. For excitation of a-Si in the telecommunication range using an ultrafast laser, a critical density N_{eh}^{crit} of around 10^{21} cm^{-3} is achieved via two-step absorption ($\beta \simeq 120$ cm/GW) at a fluence of $F_0 = 0.73$ mJ/cm^2 [158]. Two-step absorption is an upconversion process where the electron is excited by two photons through an intermediate state, which in a-Si can be a midgap defect state. Similar switching fluences are obtained using linear absorption above the bandgap, where $\alpha_0 > 10^5$ cm^{-1} [160]. For excitation using a diffraction-limited spot of around 1 μm^2 area, the above fluence gives a switching energy of 7.3 pJ. This compares well to values achieved using microphotonic ring resonators [156] and photonic crystal nanocavities [157], which are however intrinsically several orders of magnitude slower than plasmonic devices [146].

The above switching energies are valid for ultrafast pulsed excitation. Under stationary pumping conditions, the carrier density will be limited by different relaxation mechanisms such as surface recombination, Auger processes, and electron diffusion. The ultrafast response of a-Si thin-films has been extensively studied by Esser et al. [160], who have shown that carrier densities in the 10^{21} cm^{-3} can be achieved using ultrafast laser absorption. Carrier-trapping into localized states leads to a considerable reduction of the free carrier lifetime for a thin film compared to bulk crystalline Si. Above densities of 8×10^{19} cm^{-3} another contribution to the relaxation time appears due to Auger processes involving spatially overlapping electron-hole pairs. The combined processes result in a relaxation rate of the order of 10^{13} s^{-1} at carrier densities around 10^{21} cm^{-3} [160]. An additional limiting factor to the carrier concentration is carrier diffusion out of the gap region. For an $S = 20$ nm gap region and a carrier diffusion constant of $D_e \simeq 40$ cm^2/s, electron diffusion will contribute to a relaxation rate of around $(S^2/D_e)^{-1} \sim 10^{13}$ s^{-1}, i.e. comparable to the Auger process.

In practice, these relaxation rates balanced against the pumping rate will determine the stationary free carrier population that can be achieved. However, they also provide the ultrafast time response of the nanoantenna switch desirable for many applications. Eventually all the energy deposited into the system will be converted into heat by electron-phonon relaxation on a time scale of picoseconds [167]. In the extreme case that all this energy is dissipated entirely in the nanoantenna, it produces a temperature rise of around 30 K. For this estimation we have used the lattice heat capacity of gold, $C_L \simeq 2.5 \times 10^6$ J/m^{3}K, and a total amount of 10^6 generated electron-hole pairs per antenna and per pump pulse. This number of carriers follows from Eq. (4.3) for the switching fluence of 0.73 mJ/cm^2 and the antenna gap dimensions. Effects of overheating can be substantially reduced by embedding the antenna into an environment with a good thermal conductivity.

The combination of strong optical resonances with a high local field enhancement in the antenna gap opens up opportunities for optical pumping employing the mode structure and its dynamic modulation. Since only a nanometer-sized active volume has to be pumped, which is strategically located in the antenna gap, the estimated pump intensity required for switching can be significantly reduced through funnelling of pump energy into the resonant antenna mode. Considering a typical 100-times resonant intensity enhancement in the antenna gap [50, 162], we estimate an ultimate switching energy of around 100 fJ. In addition, it may be possible to employ the strong resonant enhancement of nonlinear optical phenomena in the feed gap, such as second harmonic and supercontinuum generation [162, 168, 142], to produce a nonlinear absorption complementary to two-step absorption. The above resonant reduction of the pumping threshold assumes that this energy can be deposited into the resonant mode before the switching itself changes the antenna mode structure. In the other limit of stationary resonant pumping, the dynamic switching of the antenna will result in optically bistable behaviour [169]. We propose that the nanoantenna switch can thus be used as a saturable absorber element. This application may hold substantial promise for semiconductor lasers, which currently operate in the sub-100 fs pulsed regime [170]. The exact conditions for successful operation of plasmonic saturable absorbers will require extensive modelling which goes beyond this thesis.

4.5 Use of mode interference for switching

As shown in Fig. 4.4, plasmonic nanoantenna switches are very attractive because of their capabilities of control over the near-fields. However, positioning a quantum emitter in the gap is impossible because of the a-Si filling. This problem is circumvented by using, for example, a nanoantenna trimer and switching only one of the two available gaps. The idea is to switch into an EIT mode configuration sustained by the fully switched trimer (then effectively a dimer) as explored in the previous chapter.

A trimer with a strategically placed photoconductive junction was used for gap loading calculations. We look at a trimer with arms of 200 nm, 200 nm and 190 nm and gaps of 10 nm, with the gap between the 200 nm arms filled with a-Si (see Fig. 4.7). In Fig. 4.6a), we show the respective resonances of the 190 nm nanorod and the a-Si filled dimer with 200 nm arm lengths, as well as the unswitched trimer. The resonances of the components do not appear to overlap – there is, however, the dark antibonding mode of the dimer to be considered. The interference between this dark mode and the bright first order mode of the 190 nm nanorod causes another splitting, as shown for the unswitched trimer. The other splitting occurs for the switched trimer, where we essentially have

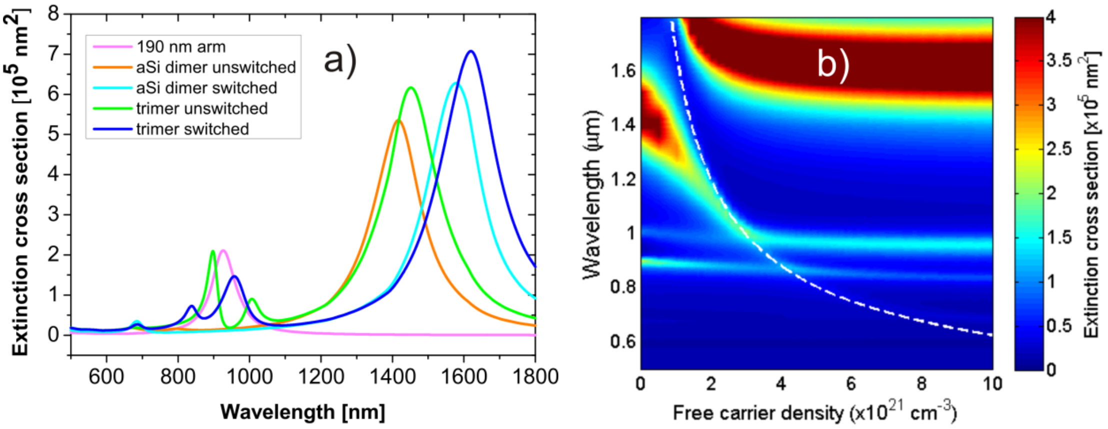

Figure 4.6: (a) Spectral extinction for a dimer with 200 nm arm lengths, a 190 nm nanorod and the complete trimer with different free carrier concentrations. (b) Spectral response as a function of photoexcited free-carrier concentration in the a-Si-filled gap. The trimer antenna has arms of two times 200 nm and another arm of 190 nm length, with gaps of 10 nm between them.

a dimer with arm lengths of 410 nm and 190 nm. As shown in the previous chapter, another splitting occurs at these arm lengths, due to the interference between the bright first order mode of the short rod and the dark second order mode of the long rod. This means that the switching in such a trimer will result in a progression from one initial splitting to another, fundamentally different splitting.

The dependence of the extinction cross section on the free carrier density is displayed in Fig. 4.6 on the right. Increasing the free carrier density in the gap, we see the expected blueshift of the strong first oder mode of the dimer in the NIR. Above the critical density which is again plotted as a dashed white line, we observe again the mode spectrum which was discussed in the previous chapter for the asymmetric dimers. What is of particular interest here is the behaviour at the criticial density line, where we go from one splitting to another. Where the blueshifted fundamental mode reaches the critical density line, it transforms into the dark λ-mode of the switched dimer, causing the splitting in the switched asymmetric dimer configuration.

In Fig. 4.7, the near-field intensity maps show the switching at four different positions along the trimer: at 5 nm from the ends as well as in the center of the feedgaps. At point A1), we oberve the dispersion of the fundamental mode in our structure and the reappearance of the new mode above the critical density, as well as the switching between the splitting. This is better visible in point A4), where the difference between the splittings divided by the critical density becomes obvious. Near-field intensity enhancements of a factor 30 are switched from 900 nm to 1000 nm, i. e. from the high-energy part of the original splitting to the low-energy part of the second splitting. In the a-Si filled midgap, the field enhancement is much the same as for the symmetric dimer of the previous section. Of particular interest is position A3), where we have extremely high field enhancements of up to 120 at all free-carrier densities, due to the strong capacitive

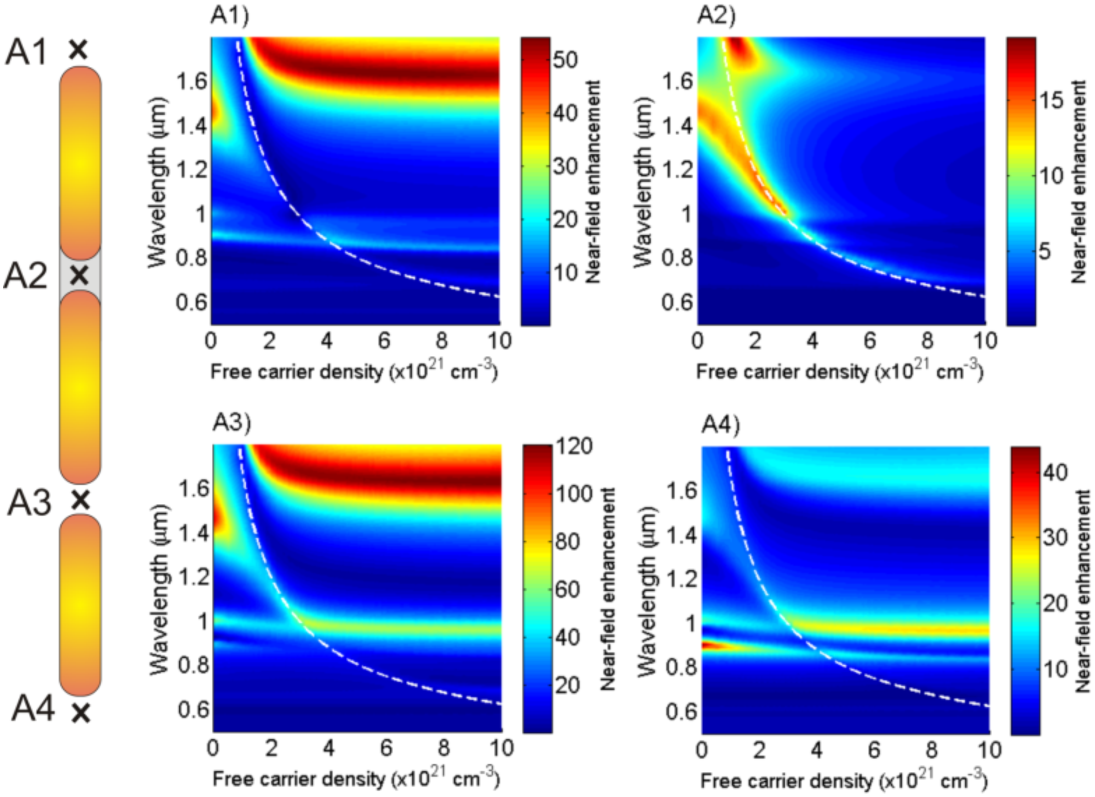

Figure 4.7: Near-field intensity maps as a function of the free carrier density for a trimer nanoantenna with arms of two times 200 nm and an additional arm of 190 nm length, with gaps of 10 nm. The gap between the 200 nm arm is filled with a-Si. A1) and A4) are taken at 5 nm distance from the endcaps, A2) and A3) in the respective midgaps.

coupling. This position can also be exploited for switching between higher-order mode interferences, as shown here.

Trimers and more complex structures hold great promise for applications as nanoantenna switches, especially with regard to controlling the near-fields. What we presented here is only a first step towards exploitation of the variety of dark and bright modes sustained by these structures – more investigations are needed to improve near-field control by varying different system parameters, such as the length of the third rod, or the length-length ratio of the asymmetric dimer with the filled gap, as explored in the previous chapter.

4.6 Conclusion

We have investigated a new class of nanoscale optical switches consisting of a plasmonic nanoantenna loaded with a photoconductive semiconductor material. By short circuiting the antenna gap using a semiconductor free-carrier plasma, we have shown that the mode spectrum of the antenna shifts dramatically using only very modest pumping energies. The nanoantenna switch can be used to control both far-field and near-field properties. In addition, we have identified a regime of partially conductive gap where a new plasmon mode is formed, which combines a narrow spectral profile with a large local-field enhancement in the antenna gap. The nanoantenna switch combines large modulation depth, low switching threshold, and potentially ultrafast time response. Although the switching threshold is relatively high compared to terahertz photoconductive devices, we expect that these carrier densities can be achieved using ultrafast optical pumping. As the switching mechanism is universal to any photoconductive medium, other semiconductors or semimetals such as ITO can be explored (see next chapter). Further optimisation may be possible by considering antenna designs different from the coupled-dipole configuration. As an example, we have explored trimer nanoantenna switches sustaining EIT for near-field control, but many other configurations are also feasible.

Chapter 5

All-optical control of single nonlinear plasmonic nanoantenna-ITO hybrids

In this chapter, a first attempt is made at realising a nanoantenna switch as introduced in the previous chapter. We demonstrate experimentally picosecond all-optical control of a single plasmonic nanoantenna embedded in indium tin oxide (ITO). We identify a picosecond response of the antenna-ITO hybrid system, which is distinctly different from transient bleaching observed for gold antennas on a nonconducting SiO_2 substrate. Our experimental results can be explained by the large free-carrier nonlinearity of ITO, which is enhanced by plasmon-induced hot-electron injection from the gold nanoantenna into the conductive oxide.

The main difference between the concept introduced in the last chapter and this first implementation lies, for one thing, in the material itself – we use Indium Tin Oxide (ITO) instead of amorphous silicon. We initially started our experiments with a-Si, but soon found that the gold nanoantennas tend to diffuse into the silicon at even moderate laser powers. ITO has recently become very popular as a transparent semiconductor in micro- and nanoelectronics. There is also a difference in the material coverage between this chapter and the previous one. Instead of depositing a semiconductor just in the gap, ITO is used as a substrate and sometimes as a cover layer since for deposition in the gap only, the necessary precision was impossible to achieve with the e-beam in our cleanroom.

The gold nanoantennas were fabricated using standard electron-beam lithography on an ITO-coated glass substrate, as described in chapter 2. Two types of commercial ITO substrates (Sigma-Aldrich) were used: a 25-nm thick ITO layer with sheet resistivity of 70-100 Ω/sq ('low-conductivity'), and a 120-nm thick ITO with sheet resistivity of 8-12 Ω/sq ('high-conductivity'). Nanoantennas were fabricated using deposition of a gold layer of 25 nm onto patterned photoresist followed by liftoff. We produced samples of nanoantennas on high- and low-conductivity ITO both with and without a cover layer of ITO. For covered antennas, a 25 nm thick ITO layer was deposited with a sheet resistivity matched to the respective ITO substrates. High conductivity ITO with a sheet resistance of 20 Ω/sq was obtained by r.f. sputtering in an oxygen/argon plasma with a mixing ratio of 1:136 at a temperature of 490°. Low conductivity ITO with a sheet resistance of 150 Ω/sq was obtained by r.f. sputtering in an oxygen/argon plasma at a temperature of 300° using the same mixing ratio.

5.1 Linear and nonlinear optical response of ITO

Transparent conductive oxides have recently been identified as promising materials for plasmonics and transformation optics applications in the near-infrared [83]. ITO is a n-type semiconductor of high transparency and nearly metallic conductivity with a bandgap of 3.5 - 4 eV [43, 89], see chapter 2. Davenas et al. [89] report band-to-band transitions to be at the origin of the strong absorption observed below 0.35 μm, whereas intra-band transitions resulting from free carrier excitation occur above 1.2 μm. Unity-order changes of the refractive index of indium tin oxide (ITO) above its bulk plasmon frequency have been demonstrated using voltage-controlled nanoscale space charge regions [171]. The free carrier density of ITO can be varied through the concentration of Sn^{4+} dopants and through oxygen vacancies introduced at higher deposition temperatures [172, 173]. The plasmon frequency is directly proportional to the free carrier density, and is located in the near-infrared range at a wavelength of ~ 1 μm for carrier densities around 10^{21} cm^{-3} [174].

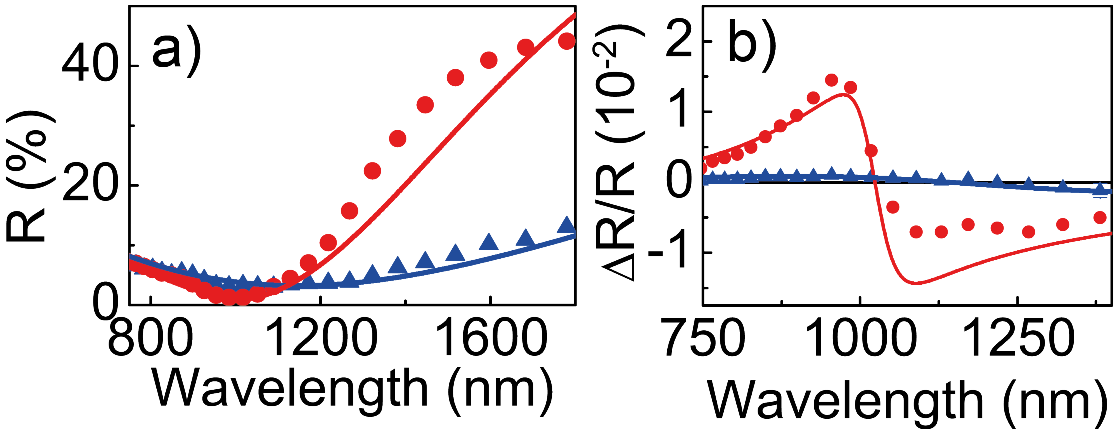

Figure 5.1: a) Measured reflectivities of the high- (red circles) and low-conductivity (blue triangles) substrates, fitted with the Drude model. b) Corresponding slow nonlinear response to pumping at 532 nm with 180 pJ from the ITO layers, again with corresponding Drude fits.

To analyse the linear and nonlinear optical response of our pure ITO films, we performed spectrally resolved reflectivity and pump-probe experiments at a distance 5 μm away from the antenna structures. Fig. 5.1a) shows the experimental reflectivity spectra of the low- (blue triangles) and high-conductivity (red dots) ITO layers. The reflectivity can be modeled using a simple Drude model description [175] as used in the previous chapter, including the experimental dielectric response of ITO [43]

$$\tilde{\epsilon}_{\rm ITO}(\omega) = \tilde{\epsilon}_{\rm exp}(\omega) - \left(\frac{\omega_{\rm pl}}{\omega}\right)^2 \frac{1}{1 + i(\omega\tau_D)^{-1}}\,, \tag{5.1}$$

where $\omega_{\rm pl} = \sqrt{Ne^2/\epsilon_0 m^*}$ denotes the plasma frequency, with N the free electron density, $m^* = 0.4m_e$ the effective electron mass, and $\tau_D = 5\times10^{-15}$ s the Drude relaxation time of ITO [174]. Fits to the experimental data were obtained using a multilayer reflectivity model [176], where we consider the reflectivity of a system composed of two dielectric interfaces. We therefore use the three-phase Fresnel equation [176]:

$$R = \frac{r_{10}^2 + r_{21}^2 + 2r_{10}r_{21}\cos(2\psi)}{1 + r_{10}^2 r_{21}^2 + 2r_{10}r_{21}\cos(2\psi)}, \tag{5.2}$$

with $r_{10} = (\sqrt{\epsilon}-1)/(\sqrt{\epsilon}+1)$ and $r_{21} = (1.52-\sqrt{\epsilon})/(\sqrt{\epsilon}+1.52)$ the two phase field reflectances at the air-ITO interface and the ITO-glass interface, respectively, with the refractive indices for glass (1.52) and air (1) already filled in. The phase ψ for an angle of incidence of 0° is $k\sqrt{\epsilon}l$, with k the wavevector and $l = 125$ nm the thickness of the ITO layer. These fits of the experimental data with both the Drude model and the three-phase Fresnel equation yield electron densities of $(9.6\pm0.1)\times10^{20}$ cm^{-3} for the high-conductivity ITO and $(7.3\pm0.1)\times10^{20}$ cm^{-3} for the low-conductivity ITO sample (lines in Fig. 5.1a).

The ITO reflectivity shows a transition from dielectric to metallic response, defined by the transition from positive to negative real part of ϵ. This behaviour is also observed in the nonlinear reflectivity changes as shown in Fig. 5.1b), representing the slow, stationary nonlinear component. The differential reflectivity $\Delta R/R$ can be calculated from the Drude model Eq. (5.1) through the shift of the plasmon resonance frequency $\Delta\omega_p = (\omega_p/2N)\Delta N$ for small changes in the carrier density ΔN. The general features of the experimental spectra for both ITO layers are reproduced well [lines in Fig. 5.1a)], apart from some discrepancy at longer wavelengths. The bipolar shape is attributed to the redshift of the bulk plasmon frequency, where the zero crossing in Fig. 5.1a) corresponds to the minimum in the Fresnel reflection at the air-ITO interface, given by $\tilde{\epsilon}_{\rm ITO} \simeq \epsilon_{\rm air}$. The fitted spectra show a decrease of the electron density ΔN of $(-2.1\pm0.1)\times10^{18}$ cm^{-3} and $(-5.4\pm0.2)\times10^{16}$ cm^{-3} for the high- and low-conductivity samples, respectively, at a pump energy of 180 pJ.

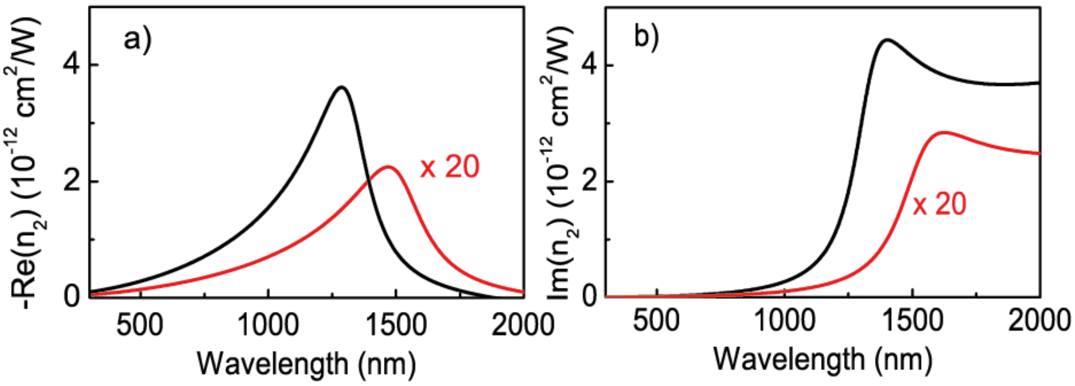

Figure 5.2: Free-carrier nonlinearity as described by the nonlinear coefficient for 20 nm low-conductivity (red) and 120 nm high-conductivity (black) ITO substrates.

The nonlinearity of pure ITO is thus governed by the free carrier-density, as shown here and in [97]. Similar to the instantaneous Kerr effect [177, 178], this noninstantaneous third order nonlinearity can be expressed by a nonlinear coefficient n_2, representing the resulting refractive index modulation Δn by optical pumping at 532 nm normalised to the optical peak intensity I of the excitation beam: $n_2 = \Delta n/I$.

Resulting values of n_2 for both the real and the imaginary part of this nonlinear refractive index coefficient over the spectral range are shown in Fig. 5.2 for a 20 nm layer of low-conductivity ITO (red curve) and a 120 nm layer of high-conductivity ITO (black curve). These are obtained from fits to the experimental reflectivity data shown in Fig. 5.1. We find a much larger nonlinearity (more than a factor 20) for the high-conductivity ITO, due to the strong dispersion of the free-carrier nonlinearity near the plasma frequency and the larger ΔN resulting from stronger pump absorption at 532 nm. Our values for the Kerr-nonlinearity are of the same order of magnitude as values for the Kerr-nonlinearity of ITO films with similar electron density [178], taken at a single wavelength around 720 nm.

5.2 Optical response of single gold antenna-ITO hybrids

The plasmonic modes of individual nanoantennas are characterised using the method of spatial modulation microscopy (SMM) [103, 104, 105], which was explained in more detail in chapter 2. SMM produces very sensitive extinction measurements by detecting a periodical modulation of the particle position in the laser focus using a lock-in amplifier. The nanoantennas are located using two-dimensional SMM scans. The spatial modulation is chosen perpendicular to the antenna long axis to reduce finite-antenna size effects in the SMM response.

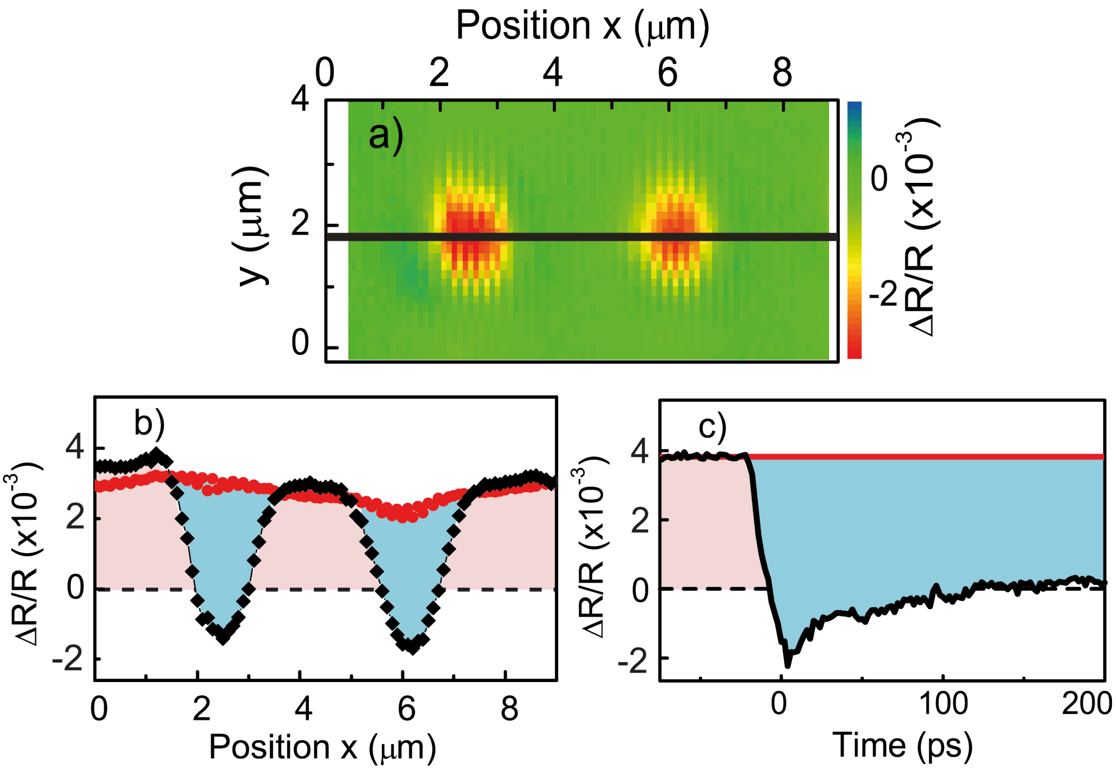

Figure 5.3: a) Fast component pump-probe scan of two antennas with the thermal background subtracted. The black line indicates where the data for b) is measured, both for the fast (black, blue) and the slow (red) component, both clearly centered on the antennas. c) Time-resolved reflectivity at 910 nm wavelength of the slow thermal (red) and the fast antenna-ITO hybrid response (black, blue).

After identification of a single nanoantenna using its optical extinction signature, we measured its picosecond nonlinear response following excitation by the pump laser. A nonlinear response was observed from both the nanoantenna and the ITO substrate, as illustrated in Fig. 5.3 for two symmetric nanoantennas. Spatial scans taken across the antenna at pump-probe delays of −20 ps (red dots) and 5 ps (black diamonds) are shown in Fig. 5.3b). These scans, as well as the two-dimensional image of Fig. 5.3a) showing only the fast (blue) component, reveal that the fast pump-probe signal is only present at the position of the nanoantenna. Figure 5.3c) shows the time-resolved nonlinear response measured at the position of the nanoantenna, at a wavelength of 910 nm. The differential reflectivity signal $\Delta R/R$ consists of a stationary, positive component characteristic for the ITO, indicated by the red shaded area, and a fast, negative component with a decay time of 500 ± 30 ps, indicated by the blue shaded area. The stationary component agrees well with the measurements for pure ITO as shown in the previous section and can be attributed to the background signal of ITO in the focal spot, which is unrelated to the nanoantenna. In the following, we will focus on the fast component of the antenna-ITO response only.

5.2.1 Symmetric nanoantennas on ITO

The spectrally-resolved nonlinear response of a typical symmetric nanoantenna-ITO hybrid on and also covered by high-conductivity ITO is shown in Fig. 5.4b), where the $\Delta R/R$ amplitudes are plotted at a delay of 5 ps (black diamonds). A complete time- and wavelength-dependent picture of the nonlinear modulation for the antenna-ITO hybrid is shown in Fig. 5.4c). The dependence of the nonlinear signal on pump energy is shown in Fig. 5.4d). Both the stationary (red dots) and the fast (black diamonds) components show a linear dependence on pump power, indicating that the nonlinear response results from single-photon absorption.

As already mentioned, the stationary component (not shown in Fig. 5.4) closely resembles the pure ITO response without the nanoantenna. The fast component (blue area) shows a bipolar shape centered at the antenna dipole resonance. Given that the antenna covers a fraction of only several per cent of the probe spot, the equal magnitude of the

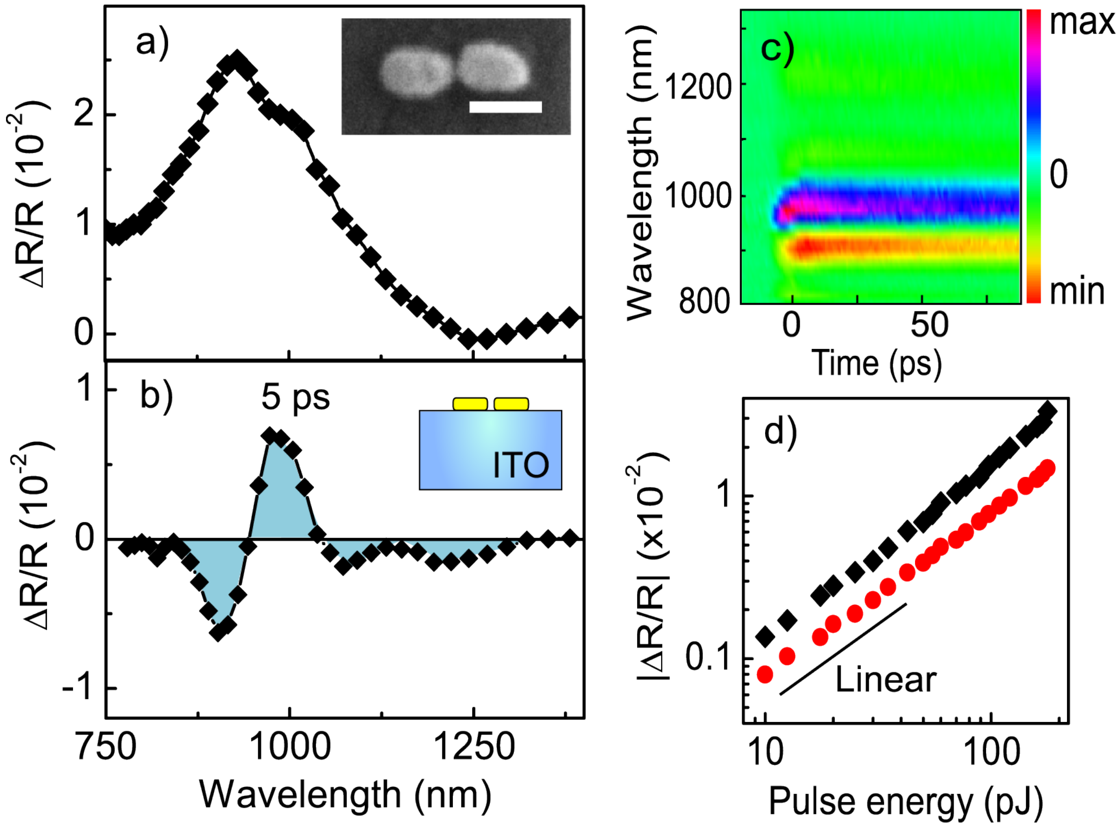

Figure 5.4: a) Extinction spectrum and b) Fast nonlinear response of a nanoantenna with a 20 nm gap embedded in high-conductivity ITO at 180 pJ, with the thermal background from the ITO subtracted. The inset in a) and b) show an SEM picture of the antenna and a schematic, respectively. c) Time-resolved spectrum of the nonlinear response. d) Dependence of the slow heat component (red circles) and the fast component (black diamonds) of $|\Delta R/R|$ on pump energy, at 980 nm wavelength.

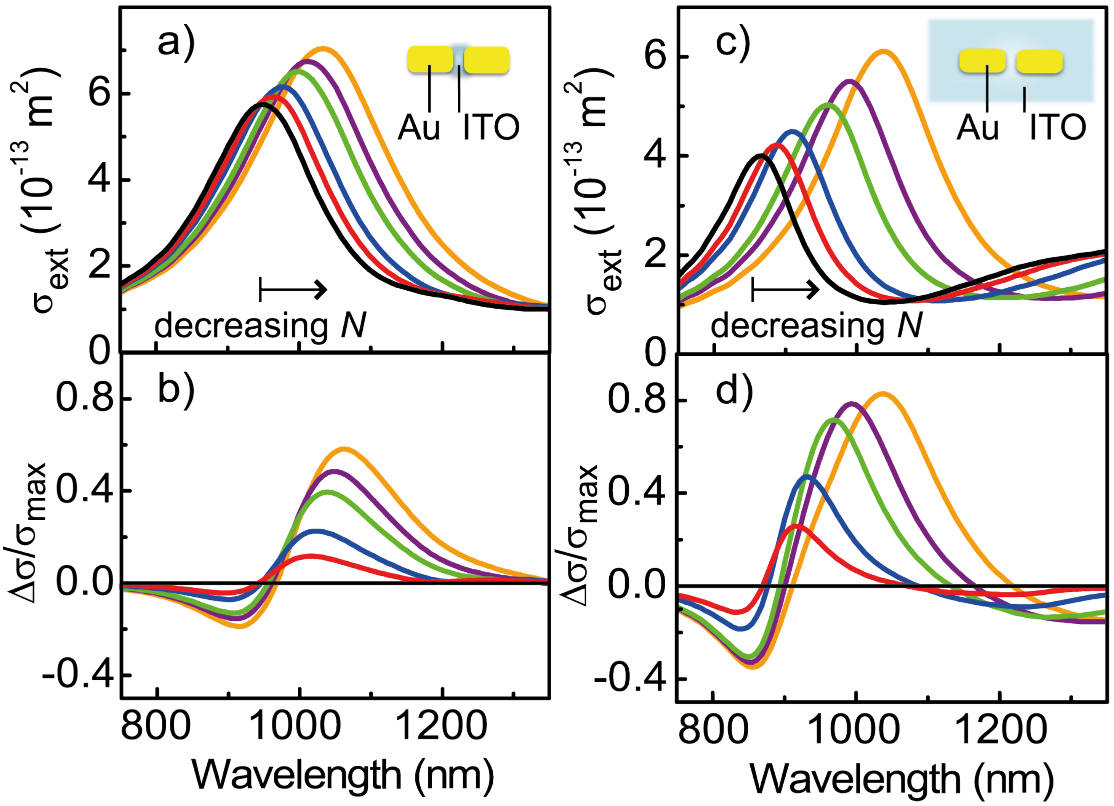

Figure 5.5: a) Extinction spectra for an antenna with ITO only in the gap with the same dimensions as the antenna in Fig. 2 with arm length 200 nm, arm width 120 nm, height 25 nm and gap size 20 nm with FDTD simulations at different carrier concentrations: 9.6 (black), 9.0 (red), 8.0 (blue), 7.0 (green), 6.0 (magenta) and 5.0 (orange) $\times 10^{20}$ cm^{-3}. b) Corresponding differential signal. c) and d) show the same as a),b), but for an antenna completely embedded in ITO, comparable to the antenna in Fig. 5.4.

antenna and ITO signals (compare Fig. 5.3) shows that the antenna nonlinear response is an order of magnitude larger than that of the pure ITO. This difference is even larger for the antennas on low-conductivity ITO, which show a similar strong antenna hybrid response. A similar response was observed for antennas on ITO substrate as for antennas which were fully covered with an ITO top layer.

As a starting point in our analysis of the ITO-antenna interaction, we calculate the response of a plasmonic nanoantenna to a modification of the ITO free carrier density using FDTD simulations. We consider a rectangular dimer nanoantenna with dimensions of $200 \times 120 \times 25$ nm^3 for the individual arms and a gap width of 20 nm. The effect of the ITO distribution is assessed by comparing a geometry in which ITO is present only in the antenna gap with one where the antenna is fully embedded in ITO $\big[$see insets of Fig. 5.5a),c)$\big]$. Single-antenna extinction cross-sections are shown in Figs. 5.5a) and c) for various ITO free-carrier densities between $5.0 - 9.6 \times 10^{20}$ cm^{-3}. A decrease of the free-carrier density N is associated with a redshift of the antenna dipole resonance. Notice that this happens in the regime in which the ITO is dielectric, where an increase in the free-carrier density results in an decrease of the refractive index, and in addition a screening of the capacitive antenna interaction [67]. Starting from the experimentally determined carrier density of 9.6×10^{20} cm^{-3}, differential pump-probe spectra are obtained as shown in Fig. 5.5b) and d) for pump-induced changes of the carrier density. The magnitude and spectral shape of the theoretical curves matches well our experimental data for a change in carrier density of $\Delta N = -6 \times 10^{19}$ cm^{-3}. This carrier reduction is respectively one- and two-orders of magnitude larger than the stationary variations measured for the high- and low-conductivity ITO substrates in absence of antennas. While the antenna resonance clearly is sensitive to dielectric gap loading [153], no qualitative difference is observed with the fully-embedded antenna, which shows the largest resonance shift. We also performed calculations for antennas on an ITO substrate, giving qualitatively similar results as for the two cases presented here. We note that the increase of the extinction towards long wavelengths can be attributed to absorption in the ITO substrate, which scales proportional to the amount of ITO material present in the model. The oscillations in the pump-probe signal observed in this region in Fig. 5.5d), which are also found in our experimental data of Fig. 5.4b), result from the changes in the ITO free-carrier density.

5.2.2 Asymmetric nanoantennas on ITO

We now consider the effect of mode coupling and EIT as explored in chapter 3 on the nonlinear response of the asymmetric dimers. In analogy to our results obtained on symmetric antenna structures, we use the antenna-ITO hybrid system as a way to achieve a large optical nonlinearity of the combined system [97].

We experimentally investigated one of the asymmetric dimer antennas of chapter 3 with long rod length L_2 of 420 nm. The extinction spectrum obtained through the spatial modulation method is shown in Fig. 5.6a) and shows the splitting of the bright dipolar mode caused by the EIT effect. The fast, picosecond component of the nonlinear modulation signal, i.e. after subtraction of a thermal background, is shown in Fig. 5.6b) for a delay of 5 ps between the arrival of pump and probe pulses. This fast transient modulation has a typical decay time of 200 ps as can be seen from the time trace in Fig. 5.6e). For symmetric antennas, a redshift of the dipolar resonance was found resulting from a reduction in the free carrier density of the ITO substrate [97] and the resulting differential response $\Delta R/R$ was found to have a typical bipolar spectral shape. The initial free carrier concentration was found to be $N = 7.3 \times 10^{20}$ cm^{-3}, with an induced change in carrier concentration of $\Delta N \approx 6 \times 10^{19}$ cm^{-3}. Clearly, the response of the asymmetric dimer shows at least four positive and negative contributions. Comparison with numerical simulations in Fig. 5.6f) confirms this trend around the EIT anti-crossing, where both the upper and the lower branches show a redshift. The BEM simulation was run with ITO in the gap only. We find that the exact position and

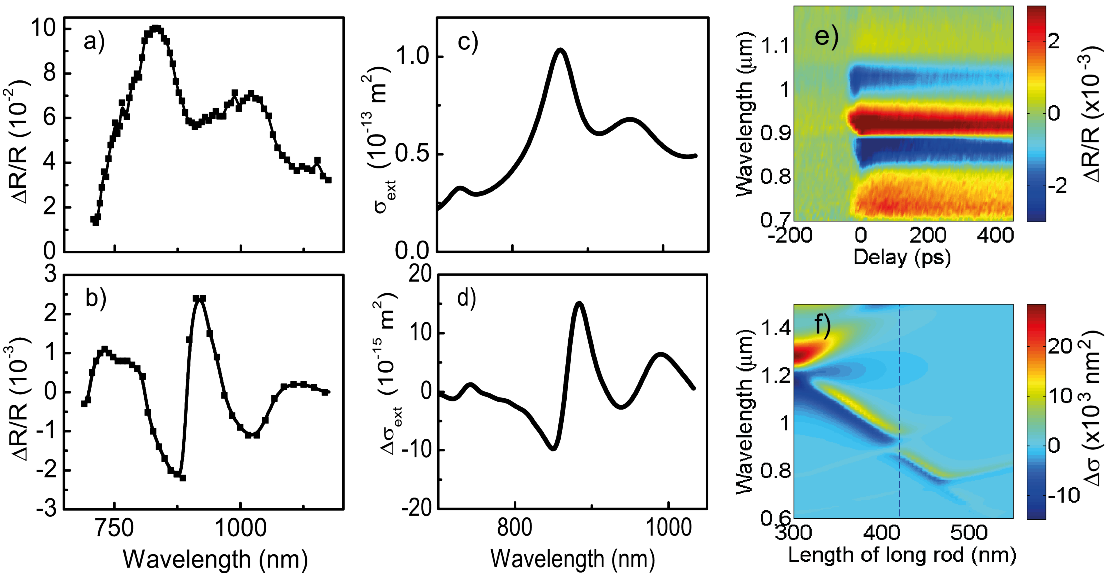

Figure 5.6: a) Experimental spectra acquired by spatial modulation spectroscopy for a dimer with higher order mode interference. b) Corresponding nonlinear signal for pumping energy of 60 pJ at 5 ps delay after the pump arrives, showing the complex dynamics taking place. c) and d) show the corresponding fit obtained with FDTD simulations. e) Time resolved trace of the nonlinear signal. f) Difference in extinction cross-section for an asymmetric dimer of varying lengths using BEM simulations for varying free carrier concentrations in the ITO.

magnitude of the positive and negative parts depend strongly on the exact antenna length. The FDTD simulations in Fig. 5.6c),d) show the response of an optimised antenna on low-conductivity ITO where indeed the observed trend is reproduced with the change in carrier concentration found earlier.

5.3 Optical response of single gold nanoantennas on SiO_2

In order to establish whether the pump-probe nonlinear response can be attributed to a gold, ITO, or hybrid antenna-ITO nonlinearity, we performed additional experiments using antennas which were separated from the ITO by a 100 nm SiO_2 spacer layer. In Fig. 5.7b), the fast (i.e. background subtracted) response of a nanoantenna grown on SiO_2 is measured. Corresponding optical extinction spectra are shown in Fig. 5.7a), for polarisation parallel to the antenna axis. We find that antennas on ITO generally have a smaller cross section compared to antennas on SiO_2, which is attributed to the different substrate permittivities in the spectral region of interest. Fig. 5.7b) shows a very different behaviour for the nonlinear reflectivity of the antenna on SiO_2. A predominantly negative $\Delta R/R$ is found, which corresponds to a decrease of the plasmon resonance and is consistent with bleaching of the surface plasmon resonance by nonequilibrium heating

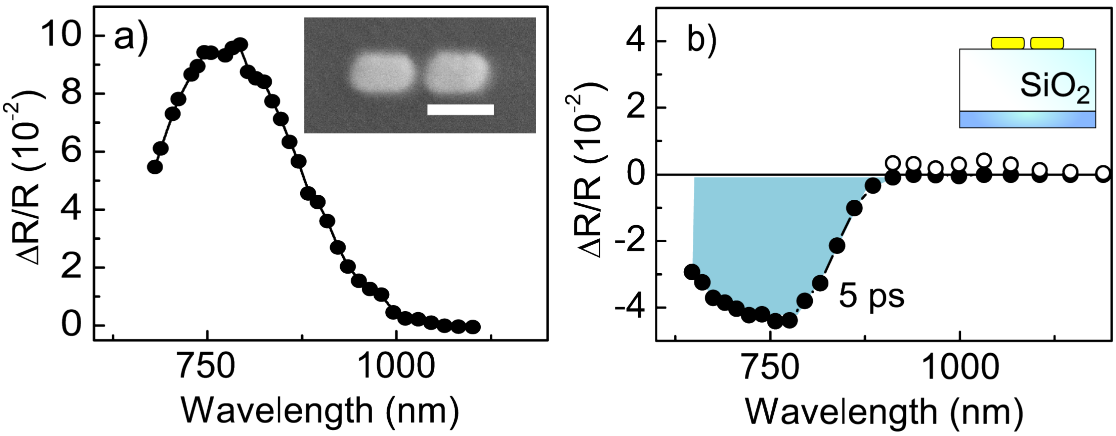

Figure 5.7: a) Extinction spectrum and b) Fast nonlinear response of a nanoantenna with a 30 nm gap on a SiO_2 spacer at low-conductivity ITO at 180 pJ. The inset in a) and b) show an SEM picture of the antenna and a schematic, respectively.

of conduction electrons in the gold [151, 179, 180]. The open circles in Fig. 5.7b) indicate slightly positive values which are caused by acoustic oscillations.

Transient bleaching as observed here is a well-known process where the heating of the electron gas leads to a decrease and broadening of the plasmon resonance. The electrons in the gold are excited by the pump pulse, the electron gas heats up and thermalises through electron-electron scattering. The electron gaps cools down further by electron-photon interactions until lattice and electron gas reach a thermal equilibrium, a process that is well described by the two-temperature model [181]. In the end, the initially absorbed photon energy is absorbed by the surrounding medium via phonon-phonon interactions, causing the aforementioned acoustic oscillations.

5.4 Comparison of different substrates and conclusions

A full statistical analysis of the behaviour of a number of symmetric antennas on the different samples is shown in Fig. 5.8, where we have plotted the maximum value of the nonlinear $\Delta R/R$ signal at a pump energy of 80 pJ, normalised to the maximum of the spatial modulation signal in order to normalise variations in antenna polarisability. A positive value is reported for antennas showing a bipolar response, while a negative value represents a unipolar bleaching signal. The statistical analysis confirms the observations of Fig. 5.4 and Fig. 5.7 that a qualitatively different response is found for the antenna-ITO hybrids as for the antennas on SiO_2. Four antennas on high-conductivity ITO did not show the reported resonance shift, but rather showed a transient bleaching response. Although a detailed understanding of the variations observed in Fig. 5.8 is lacking, we expect these may be related to local variations of the samples, including nanoantenna-substrate attachment, roughness, and polycrystallinity of the ITO. We also note that

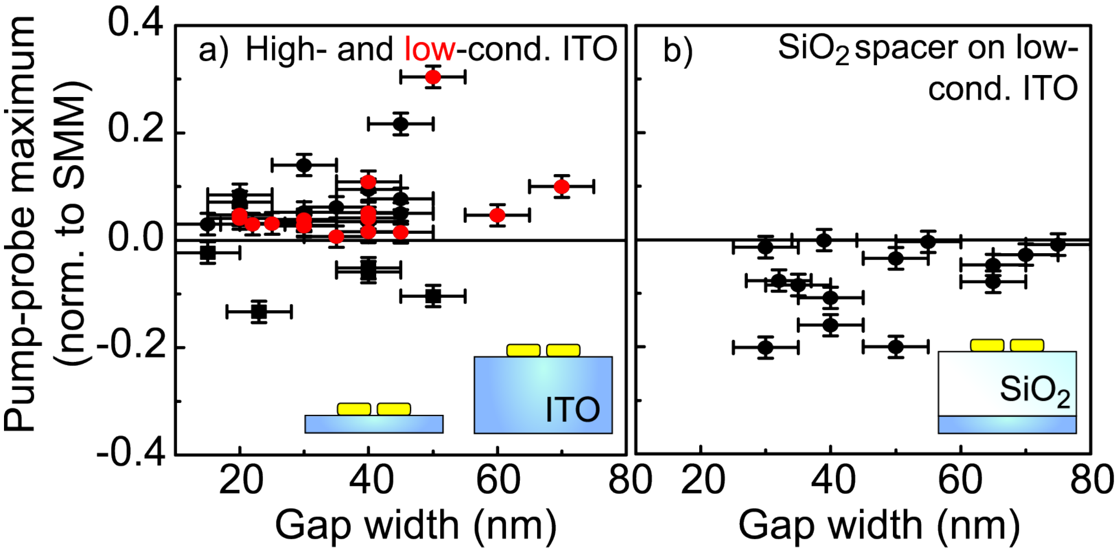

Figure 5.8: Statistics of the maximum pump probe effect normalised by the spectral maximum for a) high-conductivity (black circles) and low-conductivity ITO (red circles) as well as for b) a SiO_2 spacer between the antenna and low-conductivity ITO. ITO layers have blue, SiO_2 layers white colours. The pumping energy is 80 pJ for all measurements.

the measurements do not show a dependence on antenna gap size, indicating that the effects are not critically dependent on antenna gap filling [67]. This is consistent with the limited effect of full ITO coverage on the nonlinear response. As we used relatively moderate pump powers to obtain these statistics, the modulation depths will be 2.5 times larger for the higher pump power used in Fig. 5.4 and Fig. 5.7.

The experimental results indicate that the fast modulation of nanoantennas on ITO is directly related to nonlinear refractive index changes in the ITO substrate. As seen from the FDTD simulations in Fig. 5.5, the carrier reduction is orders of magnitude larger than the stationary variations in the ITO substrates. The nonlinear coefficient n_2 for the antenna-ITO hybrid is found to be 5.9×10^{-11} cm^{-2}/W, or 1.4×10^{-8} esu, which is 36 times larger than that for ITO without nanoantennas in the high-conductivity case. In the case of the low-conductivity ITO, we obtain an increase by a factor of 1475, which makes the low-conductivity ITO-antenna hybrids even more remarkable. The nanoantenna thus acts as a sensitiser for the ITO free-carrier nonlinearity. It should be noted that the free-carrier nonlinearity of isolated gold nanoparticles can reach as high as 10^{-7} esu [182, 183], which is however governed by its imaginary part resulting in plasmon bleaching as observed in Fig. 5.7.

As explained, the order-of-magnitude difference in free-carrier modulation obtained for the antenna-ITO hybrid as compared to pure ITO suggests an effect of the nanoantenna on the local carrier density. Furthermore, the pronounced difference in the $\Delta R/R$ pump-probe response for the antennas on ITO in Fig. 5.4 and on SiO_2 in Fig. 5.7 indicates a difference in the mechanism underlying the nonlinear antenna response. This

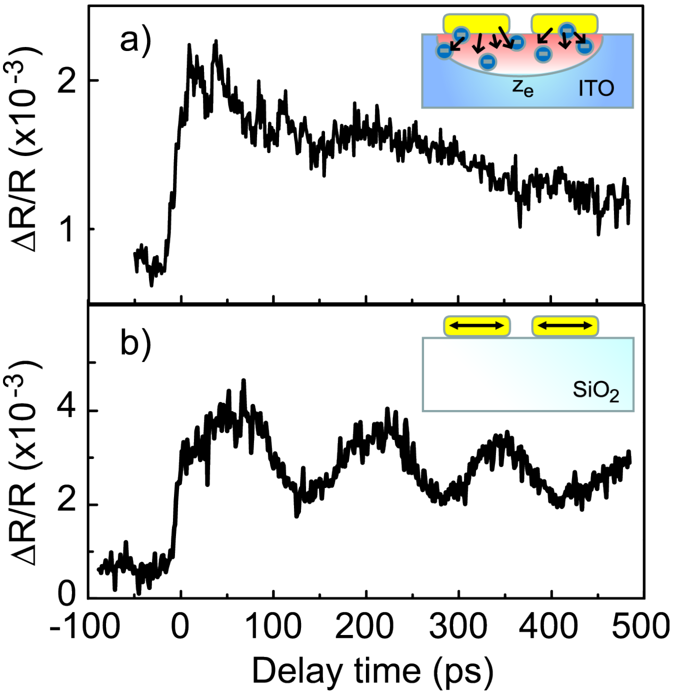

Figure 5.9: Time-resolved reflectivity, at 1050 nm wavelength, of single nanoantennas on a) high-conductivity ITO and b) on SiO$_2$. Inset: mechanisms showing fast electron injection from the gold into the depleted ITO in panel a); and energy relaxation in the isolated gold antenna on SiO$_2$ in panel b), exciting the coherent vibrational modes of the nanoparticle.

interpretation is supported by further evidence gained from the presence of vibrational modes, as shown in Fig. 5.9. It is well-known that for colloidal gold nanoparticles, rapid energy relaxation of photoexcited electrons to the lattice results in a coherent mechanical oscillation of the nanoparticle. We observed these vibrational modes (see panel b) in Fig. 5.9) for a large number of antennas on SiO$_2$, as well as on low-conductivity ITO, but not for antennas on high-conductivity ITO (see panel a) in Fig. 5.9). Of 17 antennas on low-conductivity ITO, we found vibrational modes on 11 (64.7 %), while 15 out of 24 antennas (62.5%) of antennas on SiO$_2$ showed acoustic vibrations. For antennas on high-conductivity ITO, on the other hand, we found no vibrations for all 19 antennas under study. A faster damping of the vibrational modes of the gold antenna on ITO than on SiO$_2$ would be expected given the acoustic impedances ($Z_{\text{Au}} = 6.2 \times 10^7$ kg m^{-2}s^{-1}, $Z_{\text{ITO}} = 5.6 \times 10^7$ kg m^{-2}s^{-1}, $Z_{\text{SiO2}} = 3.5 \times 10^7$ kg m^{-2}s^{-1}). However, the acoustic impedance cannot explain the incongruity between low- and high-conductivity ITO.

The absence of vibrational modes supports our interpretation that there must be a fundamental difference in the energy transfer mechanism for the two substrates. To explain all the above observations, we propose a mechanism based on fast electron injection from gold into ITO. This mechanism is facilitated by the high dc-conductivity of the transparent conductive oxide, allowing electrons to flow between the plasmonic device and the substrate. It has been shown in gold films that the nonequilibrium transport of hot electrons results in a substantial broadening of the energy deposition compared to the optical skin depth. In the linearised regime of the two-temperature model, the penetration depth z_e depends on the thermal diffusion coefficient κ_e and the electron-phonon coupling constant g as $z_e = (\kappa_e/g)^{1/2}$ [184]. The electronic thermal conductivity κ_e is given by $\kappa_e = \kappa_0 T_e/T_l$, with $\kappa_0 = 317$ W m^{-1} K^{-1} the equilibrium value for gold. For small temperature differences $T_e/T_l \sim 1$ and using $g = 2.0 \times 10^{16}$ W m^{-3} K^{-1}, the resulting electron penetration depth is $z_e = 126$ nm, which is substantially larger than the thickness of the gold antenna. Assuming a good ohmic conductance of the antenna-ITO interface, hot-electron injection within the electron-phonon relaxation time thus results in a rapid energy injection into the ITO substrate. The deposition of energy into the ITO instead of the gold lattice results in a suppression of the vibrational modes of the nanoantenna-ITO hybrid. For the low-conductivity ITO, the film thickness of 25 nm probably limits the energy transfer into the ITO film, explaining the observation of acoustic modes in this case. Fast local heating of the ITO surrounding the nanoantenna will be accompanied by a net migration of free carriers due to thermal diffusion [185, 186]. The decay of the signal on a 500 ps time scale corresponds well with the expected cooling of this zone using heat diffusion models [187]. The high repetition frequency of our setup results in a stationary background temperature over a larger, micrometer-sized area [186], which provides the pure ITO signal in Fig. 5.1.

Chapter 6

Large-area semiconductor-gold dimer metamaterials for optical switching

In the previous chapter, individual nanoantenna-ITO hybrids were investigated. In this chapter, new materials to produce all-optical switching are explored. Metamaterials are large-area materials patterened on a sub-wavelength scale which exhibit new properties. While ITO has already been shown to be a promising nonlinear material for nanophotonic switches, another type of transparent conductive oxide, aluminum doped zinc oxide (AZO), is explored as well as different deposition techniques for ITO. Especially evaporation and subsequent annealing hold great promise since this technique allows for localised deposition and nanoscale patterning.

Dimer antenna substrates were produced using hole-mask lithography over a large surface area (see chapter 2), which show a homogeneous effective medium response. Hole-mask lithography is a versatile fabrication method which can be used to produce uniform plasmonic metamaterial layers over a large surface area [68, 69, 82, 71]. Depositing conductive oxide layers of 20 nm on top allows us to confirm the proposed mechanism in a different plasmonic system, showing that hot electron injection by plasmonic gold antennas is a universally applicable mechanism for producing active metamaterials.

6.1 Gold dimer substrate

The linear spectral response of the disk dimer antenna layer without metal oxide coverage is shown in reflection in Fig. 6.1a). The presence of the plasmonic dimers is observed as a peak in the reflection spectra and a dip in the transmission spectra. The longitudinal mode of the particle dimers is redshifted in comparison to the transverse mode due to capacitive coupling between the disks of each dimer. Fig. 6.1a) shows nonlinear pump probe spectra for the pure gold dimer substrate. The dimers exhibit a transient bleaching response as expected, as shown in Fig. 6.1b). The negative nonlinear response at the position of the peak corresponds to a decrease of the resonance, whereas the positive signal at the sides (here observed at 780 nm, respectively 810 nm for the other polarisation) corresponds to a broadening of the resonance.

In the current configuration which was also used for the measurements presented in the previous chapter, the nanoantennas are pumped from the back and measured in reflection from the front. In order to pump the substrate layers directly, the sample is turned around and reflection was measured coming from the backside and pumping the frontside of the sample. The linear spectral response of the plasmonic disk dimer antenna layer without metal oxide coverage in this configuration is shown in Fig. 6.2. The presence of the plasmonic dimers is now observed as a dip both in the reflection and the transmission spectra. This can be understood by looking at the reflectivity which is given by

$$R = |E_{\text{sub}}|^2 + |E_{\text{scat}}|^2 + 2E_{\text{sub}}E_{\text{scat}} \cos\phi\,, \tag{6.1}$$

where E_{sub} denotes the reflected field of the substrate, E_{scat} the reflected field of the nanoantenna layer, and ϕ the relative phase difference between the two components. The field reflected at an glass-air interface experiences a phase difference of π when compared to that reflected at an air-glass interface, which changes the sign of the interference term in Eq. (6.1) and converts the previously seen peak into a dip in the spectrum.

Transient bleaching for a dip observed in reflection shows as a positive pump probe signal centered at the plasmon resonance, which was indeed observed for pumping from

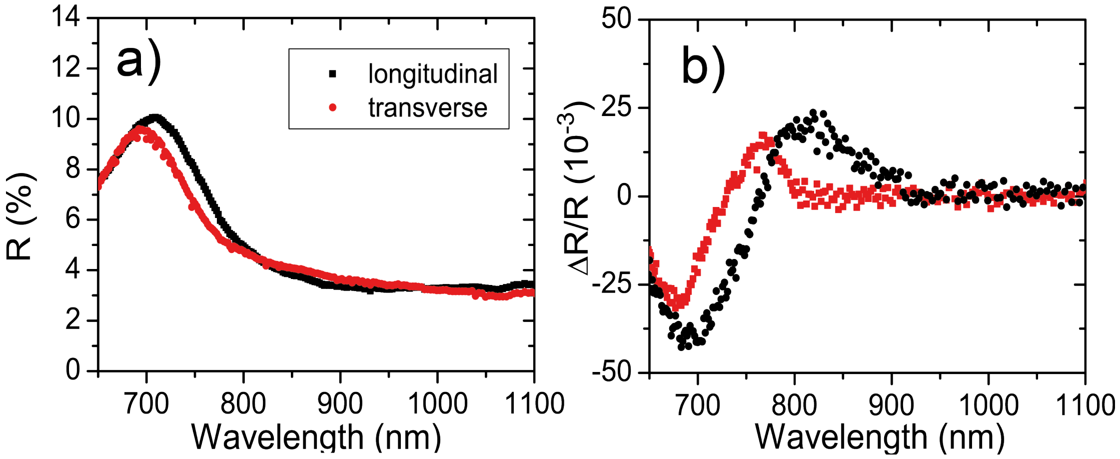

Figure 6.1: a) Reflection and b) nonlinear spectral response of the gold dimer substrate without cover layer and pumped from the back. Transient bleaching is observed, corresponding to a decrease and broadening of the plasmon resonance.

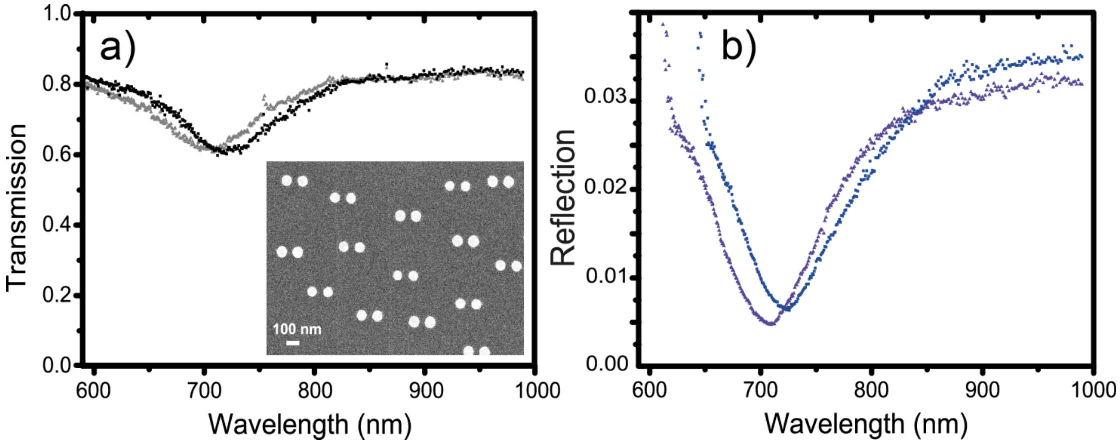

Figure 6.2: a) Transmission and b) reflection spectra of the gold dimer substrate in absence of any cover layers. We observe a dip in the spectra for both reflection and transmission, which is redshifted for the longitudinal polarisation (black in transmission and blue in reflection) with regard to the transverse polarization (dark grey in transmission, violet in reflection) due to coupling between the dimer disks. *Inset:* SEM image of the nanodisk dimers.

the front of the sample. For the cover layers investigated in the rest of this chapter, all measurements will be performed by pumping from the front and measuring in reflection on the back of the sample through the glass surface.

6.2 Gold-metal oxide hybrid metamaterial covered by layers of metal oxides

6.2.1 Gold dimers covered by an AZO layer

First, the effects are studied using a thin layer of AZO obtained by Atomic Layer Deposition (ALD) as described in chapter 2. ZnO-based materials are of enormous interest for novel electronic devices [188] for their favourable electronic, piezoelectric, and thermal properties. ALD results in smooth layers of much higher quality than conventional sputtering methods, which is favourable for obtaining reproducible devices. ALD results in controlled growth of single atomic layers, guaranteeing large-area film deposition conformality due to the self-limiting and surface-saturated reaction [100]. This process is ideal for growth of nm thick layers. However, patterning such as with e-beam or other lithographic methods is difficult, since the chemical reaction takes place everywhere on the sample.

The coverage with the various conductive oxide layers leads to a further redshift of the resonances as is shown in Fig. 6.3a) showing the longitudinal polarisation component in reflection. Compared to the uncovered antenna layers, the reflectivities show a slightly higher overall value which can be explained by the larger refractive index of the cover layers. Additionally, the plasmon resonances show a slight asymmetry. This asymmetry can be explained by the sensitivity of a reflectivity signal to small variations in the distance between a scatterer and the reflecting substrate, a phenomenon recently referred to as interferometric scattering [189]. The reflectivity is given by Eq. (6.1). For an antenna layer positioned directly on top of a substrate, $\phi = 0$ and the mixing terms have zero phase offset. However, for a 20-nm top layer with refractive index around 2.0, the reflected field from the antenna layer perceives an 80 nm optical path length difference or a $\sim 0.1\pi$ phase shift with respect to the air-conductive oxide reflection. This additional phase shift results in a contribution of the real part of the polarisability, resulting in the typical dispersive lineshape.

Nonlinear pump-probe spectra of the antenna-AZO hybrids are shown in Fig. 6.3b) for a pumping energy of 30 pJ. Similar to the response of a single nanoantenna [97] in the previous chapter, the total signal consists of a fast, picosecond contribution and a stationary component due to heat pileup. All signals are bipolar, with a zero crossing near or at the location of the minimum of the reflectivity curve, indicating a redshift of the plasmon mode. It should be pointed out that the dispersive shape of the reflectivity could also produce a bipolar nonlinear response in the case of pure plasmon bleaching, as the scattered field E_{scat} is reduced and therefore the interference term in Eq. 6.1 decreases. However, in such a case the zero crossing of the bipolar signal would be positioned at the wavelength corresponding to the phase inversion of the asymmetric profile, which clearly is not the case in our measurements.

The dependence of the optical modulation on the pulse energy of the pump laser is shown in Fig. 6.4. Here, a 60 pJ energy corresponds approximately to a fluence of

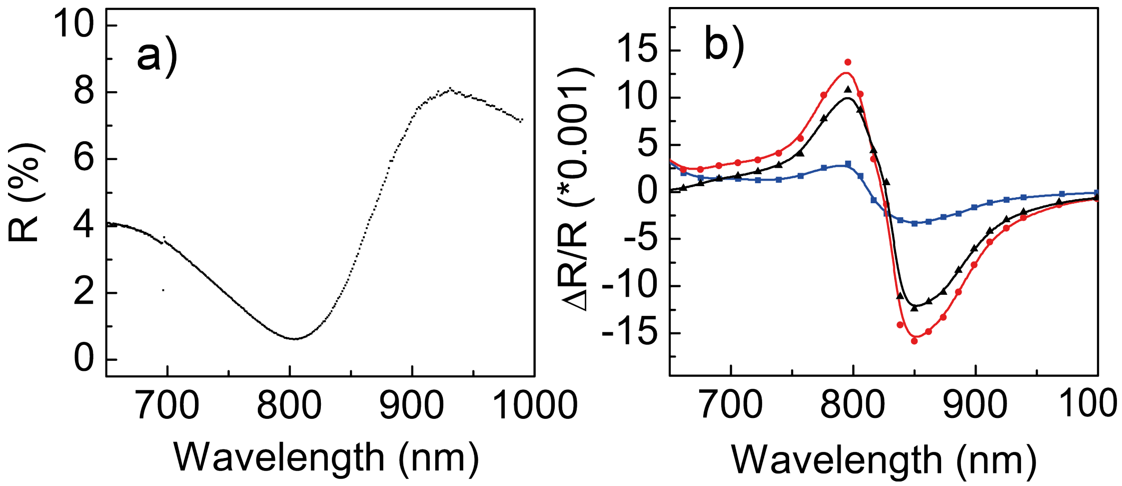

Figure 6.3: a) Reflectivity and b) nonlinear spectral response for AZO. For the nonlinear signal, we differ between 3 components: the stationary heat signal (blue squares), the fast pump probe signal on top of the heat signal (red circles), and the effective difference between both (black triangles). All signals were measured at 30 pJ.

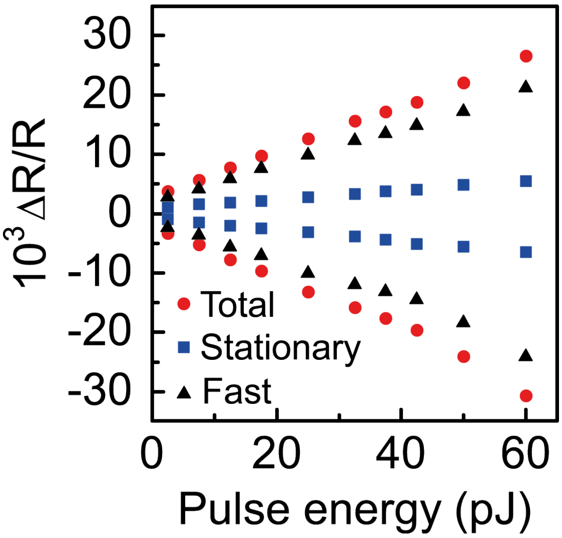

Figure 6.4: Dependence of the slow heat component (blue squares), the fast component (red circles) and their difference (black triangles) of $\Delta R/R$ on pump energy, at the peak positions of the dipolar signal for AZO at 795 nm and 850 nm.

1.9 mJ/cm^2. These results are of the same order of magnitude as the values obtained for individual antenna-ITO hybrids, when we normalise the modulation amplitude to the spectral maximum of the antenna-induced reflectivity (i.e. Fig. 5.8 in the previous chapter. Some differences may be attributed to variations in doping density and antenna geometry, the latter resulting in different amounts of absorption and carrier injection.

Regarding only the magnitude of the nonlinear response, however, the pump probe signal of our metamaterial at 30 pJ is comparable to the magnitude of the response obtained from a single nanoantenna at 180 pJ – the area in the beam spot is covered much more efficiently. Looking at cross sections, a single antenna with arm length 200 nm, height 25 nm and gap size 20 nm has an extinction cross section of around 6×10^{-13} m^2 at the resonant wavelength, as reported in [97], whereas our disk dimers have a peak cross section of 2×10^{-13} m^2 at the resonance. However, the greater density accounts for approximately 9 to 16 dimers to be in the beam at any time, which explains the much larger nonlinear response.

In Fig. 6.5, we show the time-resolved reflectivity for different wavelengths for the AZO hybrid metamaterial and for longitudinal and transverse polarisations. The thermal background signals have been subtracted for displaying purposes. Cross sections of the maps are shown in the bottom panel of Fig. 6.5 for three wavelengths corresponding to the maximum, minimum, and zero crossing of the nonlinear signals. A large difference is observed in the dynamics of the nonlinear signal: in the previous chapter, the single nanoantenna-ITO hybrids were reported to show an approximately single-exponential decay with a time constant of 500 ± 30 ps. For the AZO covered dimer metamaterial sample, we find an additional component with a time constant of 21 ± 1 ps followed by

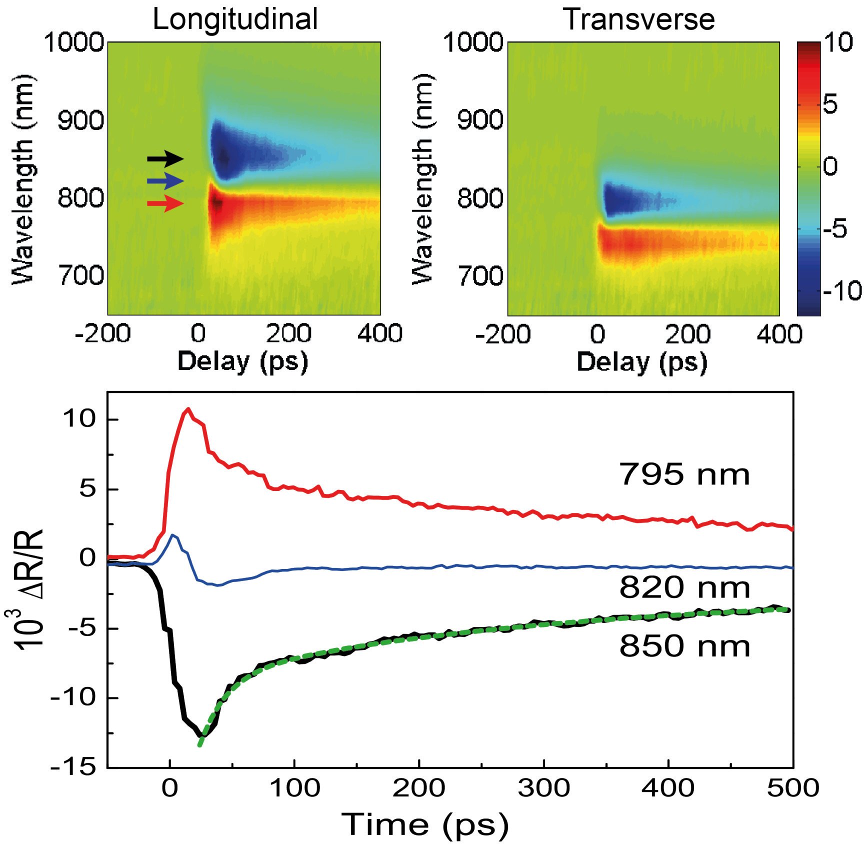

Figure 6.5: Time-resolved spectral maps of the pump-probe signals $\Delta R/R$ for both polarisations with the stationary heat components subtracted, for dimers covered in AZO. *Bottom panel:* Cross sections of $\Delta R/R$ versus time at three wavelengths corresponding to the spectra of Fig. 6.3. Fits using biexponential decay are displayed as a green dashed line yielding time constants of 21 ± 1 ps and 543 ± 14 ps.

a slower component of 543 ± 14 ps. We attribute this difference to different thermal conductivities for the ITO and AZO. For the bulk materials, values for ITO of around $\kappa_{\mathrm{ITO}} = 5.9$ W m^{-1} K^{-1} have been reported [190]. For AZO, values differ enormously from $\kappa_{\mathrm{ITO}} = 1000$ W m^{-1} K^{-1} for single-crystal ZnO down to hundred times less for polycrystalline thin films. It is well known that for polycrystalline materials, the heat conductivity is limited by diffusion barriers over grain boundaries [191]. The high quality of the AZO deposited using ALD is likely to result in better heat conductivity properties than the polycrystalline sputtered ITO. Our results call for more systematic studies of the properties of the layers produced by ALD. The similarity of the slow decay component for both layers suggest that this contribution is associated to the cooling down of the thin-film oxide through the glass substrate.

Another characteristic feature in the time-resolved maps is the fast blueshift of the bipolar signal in the first tens of picosecond following the excitation. This transient response is clearly observed in the time traces around the zero crossing of the spectral profile (blue line at 820 nm in Fig 6.5). The exact origin of this recurrent feature is not yet understood at the moment. The blueshift seems to be related to the nonequilibrium electron dynamics directly following the picosecond pump pulse. Alternatively, this fast transient may be associated with the generation of a strain wavepacket in the 20-nm thin oxide layer with frequency components up to several hundred GHz [192].

6.2.2 Gold dimers covered by sputtered ITO

A control sample covered in sputtered ITO as investigated in the previous chapter was prepared with a 20 nm cover layer. The ITO (Indium 90% Tin 10%, target from Lesker) was deposited in an oxygen/argon plasma of mixing ratio 1:136 at a temperature of 490°C. As for the AZO, the cover produces a slightly dispersive lineshape in the reflection spectrum shown in Fig. 6.6a). As before, we find a bipolar nonlinear response of the covered disk dimer antennas corresponding to a redshift of the resonance, compare Fig. 6.6b). The zero crossing of the bipolar signal is clearly positioned at the minimum of the reflection spectrum, fortifying the interpretation of a redshift.

Comparison between the signals shows that the modulation is higher for the antenna-AZO hybrids than for disk dimers covered with a sputtered ITO-layer of similar thickness. Additionally, the time-resolved reflectivity displayed in Fig. 6.5 is best fitted by a single-exponential fit yielding a decay with a time constant of 450 ± 40 ps, which agrees reasonably well with the decay times found for single antenna-ITO hybrids, keeping in mind that we used commercially available high-conductivity substrates to grow the antennas on in the previous chapter.

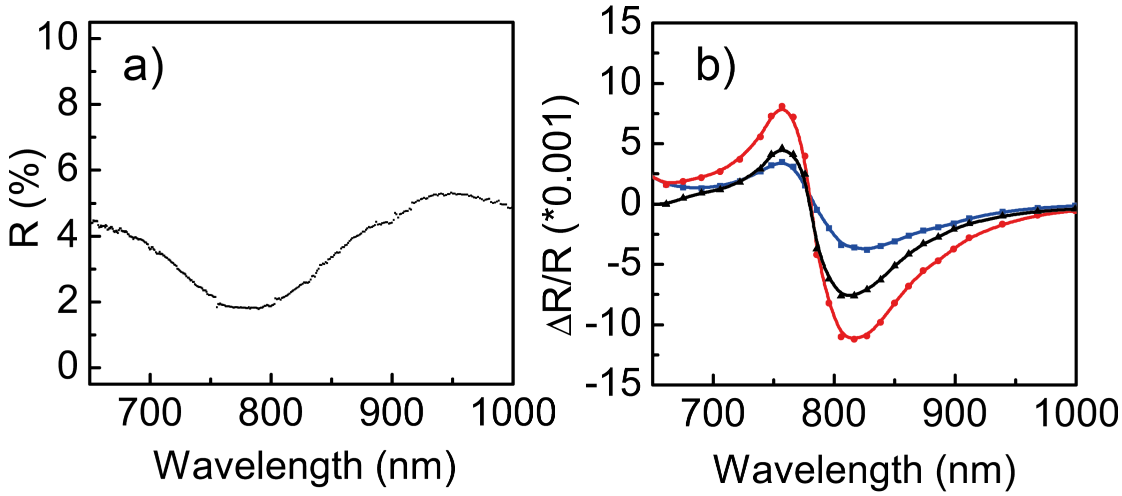

Figure 6.6: a) Reflectivity and b) nonlinear spectral response for a 20 nm ITO layer sputtered onto our dimer substrate. For the nonlinear signal, there are 3 components: the stationary heat signal blue squares), the fast pump probe signal on top of the heat signal (red circles), and the difference between both (black triangles). All signals were measured at 30 pJ.

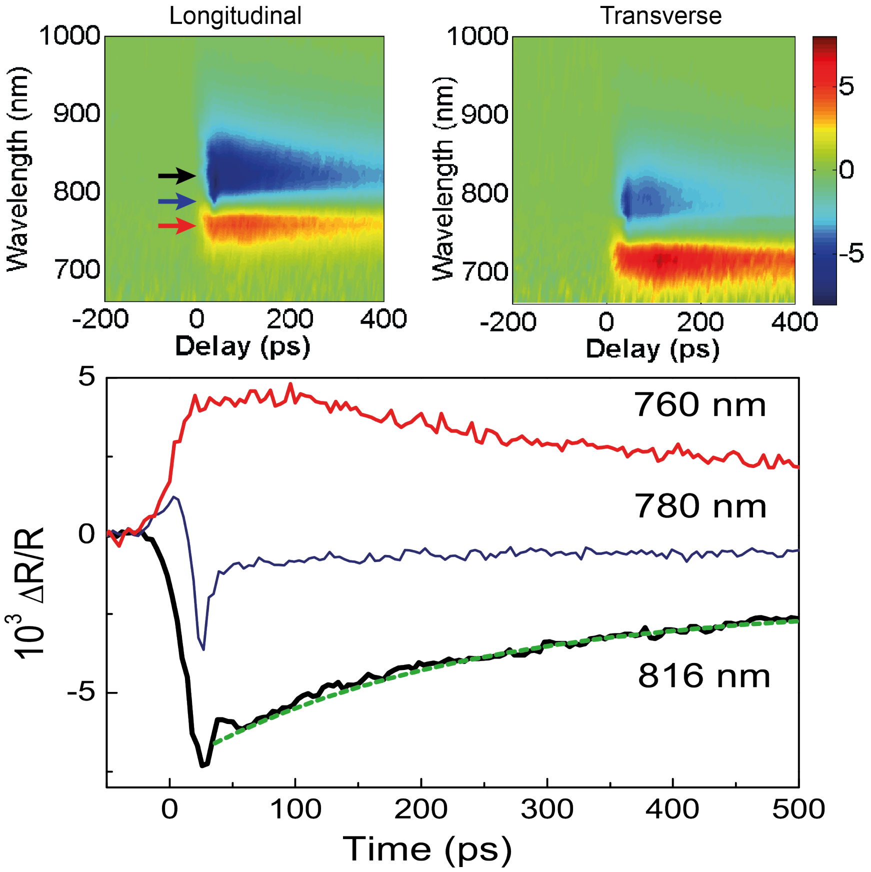

Figure 6.7: Time-resolved spectral maps of the pump-probe signals $\Delta R/R$ for both polarisations with the stationary heat components subtracted, for dimers covered in sputtered ITO. *Bottom panel:* Cross sections of $\Delta R/R$ versus time at three wavelengths corresponding to the spectra of Fig. 6.6. A fit using single-exponential decay for ITO yields a time constant of 450 ± 40 ps, and is shown as a dashed green line.

As shown in Fig. 2.9 in chapter 2, the surface of sputtered ITO even at high temperatures shows a very rough and grainy structure. This polycrystallinity limits the heat conductivity and is responsible for the slow single-exponential decay. As observed for the ITO, the bipolar signal displays a fast blueshift in the first tens of picosecond following the excitation, which can be clearly observed in the time traces around the zero crossing of the spectral profile.

6.2.3 Gold dimers covered by evaporated ITO

A sample of the dimer metamaterial covered by evaporated ITO was also fabricated. Evaporation of ITO and subsequent annealing is an established technique to produce ITO contacts [90], since it is directional and allows deposition on patterned photoresist, which is neither the case for sputtering nor for ALD. Additionally, deposition temperatures can be kept low and the subsequent annealing can be done after lift-off of the photoresist.

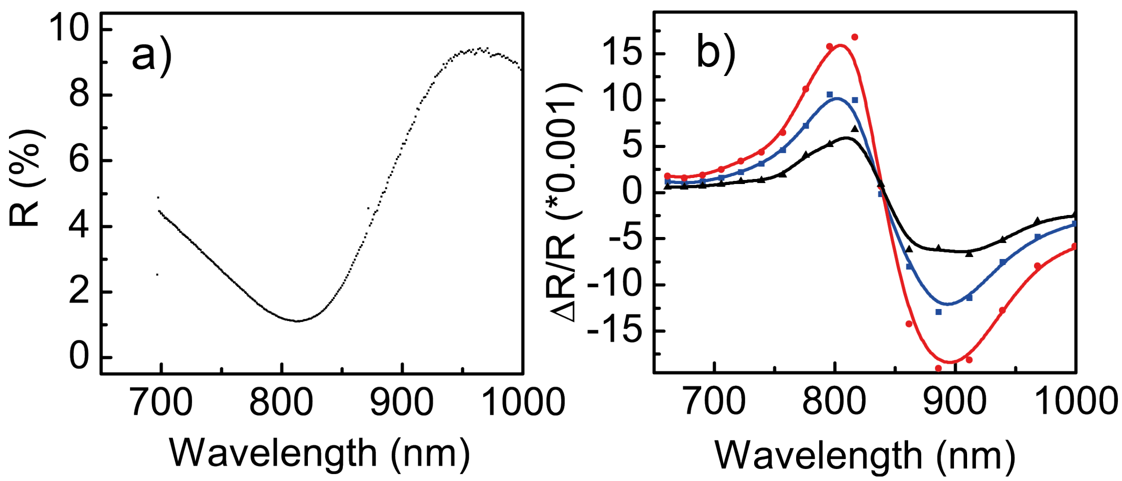

Figure 6.8: a) Reflectivity and b) nonlinear spectral response for a 20 nm ITO layer evaporated onto our dimer substrate. For the nonlinear signal, 3 components are shown as before: the stationary heat signal (blue squares), the fast pump probe signal on top of the heat background (red circles), and the difference between both (black triangles). All signals were measured at 30 pJ.

ITO grains (90-10 wt%, 99.99 % pure from Testbourne Ltd.) were heated in a ceramic crucible at 2×10^{-4} mbar partial oxygen pressure and subsequently annealed in air for 1h at 200°C, which is suffient to completely anneal a 20 nm film. For a 200 nm film, 2h were necessary to reach optimum sheet resistivity.

Conductivity was optimised for both sputtering and evaporation and led to the conclusion that while both r.f. sputtering and evaporation allow us to reach high sheet resistances of 40-50 Ω/sq for a 200 nm film of good transparency, evaporated films were found to show a much smoother consistency.

As can be seen in Fig. 2.9 in chapter 2, the evaporated ITO forms a smooth film on the gold dimers, whereas the sputtered ITO forms grains on the substrate. These grains can be found next to the dimers, but also sometimes in the gap between two disks which accounts for and explains the variety in the magnitude of the results presented in [97]. The stochiometry of ITO is crucial due to its effect on electrical and optical properties, so smooth and uniform films are desirable.

In Fig. 6.8, linear spectra and nonlinear pump-probe spectra af the antenna-ITO hybrids with evaporated ITO are shown, as before for a pumping energy of 30 pJ in order to compare the different conductive oxides. The magnitude of the signal from the sample covered with evaporated ITO is the biggest of our hybrid metamaterial devices, reaching values of more than $\Delta R/R = 15 \times 10^{-2}$. However, the thermal background for evaporated ITO is also much higher, leaving the effective difference between fast and slow components comparable to that of AZO and sputtered ITO.

In Fig. 6.8, the time-resolved reflectivity of the disk dimers covered with evaporated ITO is shown for different wavelengths for the two polarisations, with the thermal background

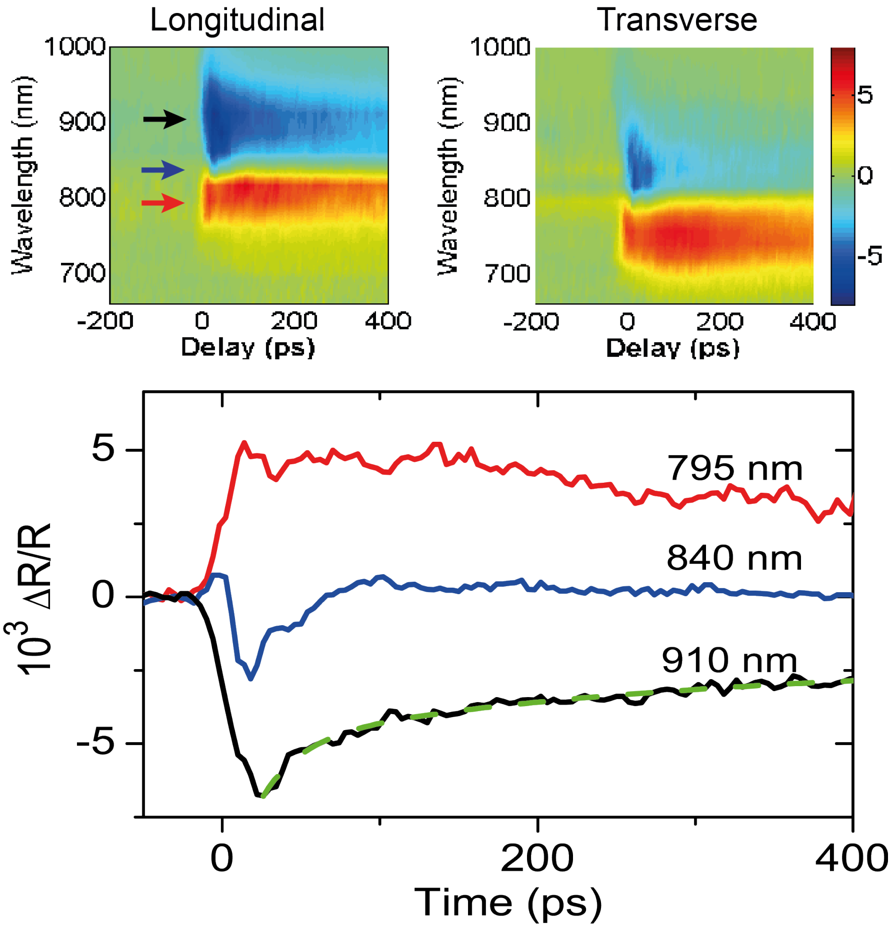

Figure 6.9: Time-resolved spectral maps of the pump-probe signals $\Delta R/R$ for both polarisations with the stationary heat components subtracted, for ITO evaporated onto the dimer substrate. *Bottom panel:* Cross sections of $\Delta R/R$ versus time at three wavelengths corresponding to the spectra of Fig. 6.8. Fits using biexponential decay are displayed as a green dashed line yielding time constants of 24 ± 4 ps and 480 ± 20 ps.

signal subtracted. In the lower panel where the cross sections are shown, the decay is again fitted better by a biexponential than by a single exponential decay, yielding times of 24 ± 4 ps and 480 ± 20 ps.

The similarity of the decay to AZO indicates that the structure of the evaporated ITO films is reasonably smooth and uniform. The fast decay time is not as short as that of the antenna-AZO hybrids, but no other deposition technique can yield films of similar conformality due to its superior control of the deposition itself.

6.3 Conclusion

In this chapter, the use of different transparent conducting oxide layers for activation of hybrid metamaterial devices was investigated. It was shown that the effect of fast electron injection from plasmonic structures into their immediate surroundings is a very general effect that occurs in a variety of materials. Transparent conducting oxides such as ITO and AZO form a group of promising nonlinear materials for use in hybrid metamaterial optoelectronic devices. The availability of highly controllable fabrication methods using Atomic Layer Deposition make AZO in particular an ideal candidate for device applications where layers of conductive oxides are needed. The possibility to achieve modulation with a 20-nm film as demonstrated here is a prerequisite for using this deposition technique which is limited to relatively thin layers. Further optimisation may provide even more sizeable changes in refractive index and therefore nonlinear response of the hybrid devices.

Decay times for sputtered and evaporated ITO as well as for AZO are summarised in Table 6.1. It was found that the response of the antenna-AZO hybrids gives both the biggest as well as the fastest response, which can be ascribed to the superior electrical and optical properties of atomic layer deposited AZO. The slow decay component found for all layers deposited on the dimer metamaterial substrate is attributed to the heat transfer from the conductive oxide layers to the underlaying glass. This heat pile-up might be reduced in the future by using another layer on top which does not contribute to the refractive index change, but provides good thermal conductivity, such as sapphire (Al_2O_3), with a thermal conductivity between 5 and 30 $Wm^{-1}K^{-1}$ [194].

Table 6.1: Decay times

Sample	fast decay	slow decay
AZO	21 ± 1	543 ± 14
sp. ITO	–	450 ± 40
evap. ITO	24 ± 4	480 ± 20

Concerning nanoscale patterning and strategic deposition of conductive oxides, first steps have been taken with the directional evaporation of ITO to locally deposit ITO in the gap. This will pave the road for further exploration and exploitation of the idea of nanoantenna switches introduced in chapter 4.

Chapter 7

Conclusion

7.1 Summary

In this section, we briefly summarise the main points of the research done in the framework of this thesis. To start with, the interference and coupling in symmetric and asymmetric dimers have been investigated both experimentally and theoretically. Asymmetric dimers in particular have been shown to provide a relatively simple model system for studying effects of electromagnetically induced transparency. Their simplicity of design in particular is of great interest, as the geometry in principle could be achieved using a variety of techniques including both top-down lithography as well as bottom-up fabrication methods such as colloidal chemistry or electrochemical templated growth [195, 196, 197].

Furthermore, we have explored theoretically a new concept of ultrafast optical switches based on plasmonic nanoantennas. These antenna nanoswitches operate on the transition from the capacitive to the conductive coupling regime between two closely spaced metal nanorods. By filling the antenna gap with amorphous silicon, progressive antenna-gap loading can be achieved due to variations of the free-carrier density in the semiconductor. Strong modification of the antenna response is observed both in the far-field response and in the local near-field intensity. This concept was explored both for the straightforward case of symmetric antennas as well as for asymmetric antennas, where it is possible to switch from the EIT coupling between the antiboding mode of a nanoantenna dimer with an additional nanorod to another destructive interference pattern of a larger antenna by short-circuiting the gap between two of the three antenna arms. The large modulation depth, low switching threshold and potentially ultrafast time response of antenna switches holds promise for applications ranging from integrated nanophotonic circuits to quantum information devices. Such nanoantenna switches can open up new avenues to applications ranging from integrated photonics and ultrafast lasers to quantum information devices and near-field control.

As a first step towards the implementation of such devices, we have demonstrated all-optical control of symmetric nanoantennas on low- and high-conductivity ITO. We identify a hybrid picosecond nonlinear response involving rapid energy transfer via hot electrons from the gold into the transparent conductive oxide that can be described by an enormous corresponding Kerr-nonlinearity. Nanoplasmonic hot-electron injection provides new functionality in controlling the optical properties of materials at the nanoscale, which is of fundamental importance as it opens a path for new ultrafast devices and for exploring combinations of new materials to produce all-optical switching. By exploiting the large free-carrier nonlinearity of ITO around the bulk plasmon frequency, hot-electron injection provides a large modulation of the antenna dipole resonance wavelength. The transparent conductive oxide ITO is shown to be a promising nonlinear material for nanophotonic switches, supporting earlier work on electro-optical modulation [171]. Apart from the nonlinear optical response of the symmetric dimers, we have also demonstrated the signature of EIT-induced splitting in the nonlinear regime through picosecond modulation of the refractive index of the ITO substrate.

In addition to this first device implementation, the use of different transparent conducting oxides for activation of hybrid metamaterial devices has been investigated. It was shown that the effect of fast electron injection from plasmonic structures into their immediate surroundings is a general phenomenon that occurs in a variety of materials. Transparent conducting oxides such as the investigated ITO and AZO form a group of promising nonlinear materials for use in hybrid metamaterial optoelectronic devices. The availability of highly controllable fabrication methods using Atomic Layer Deposition make AZO in particular an ideal candidate for device applications. The possibility to achieve modulation with thin 20 nm films (or even films of less than 5 nm) as demonstrated in this thesis is a prerequisite for using this deposition technique which is limited to relatively thin layers. Further optimisation of the various deposition processes may provide even more sizeable refractive index changes and therefore nonlinear response of hybrid devices.

7.2 Outlook – ideas and perspectives

The work done in this thesis paves the road for a number of further investigations into responses of hybrid devices and picosecond transfer mechanisms. Further work into nanoantenna-conductive oxide hybrids needs to be done to optimise the nonlinear modulation that can be achieved. For example, more complex structures with a multitude of dark and bright modes such as oligomers [198, 199, 200] might prove suitable. Additionally, the selective deposition of conductive oxides at strategic points needs to be investigated in more detail. More complex structures are also very promising for strategic gap loading, for example in the gap of a Yagi-Uda antenna, as proposed in Ref. [201].

Further optimisation of the deposition of conductive oxides might make it possible to achieve the full transition from capacitive to conductive coupling for a symmetric antenna. ALD deposition of AZO as used in chapter 6, for example, has been reported to achieve carrier densities of up to several $10^{21}/\text{cm}^3$ [202]. Optimised film deposition with better crystalline qualities will also allow us to achieve a more uniform response of single hybrid antenna devices.

Good crystalline structure will also be needed for electrically controlled devices. As already mentioned, the Atwater group has recently shown that an order-unity refractive index modulation of conductive oxides is possible by applying a bias voltage [171]. Electrical control in the form of a nanoantenna-MOSFET device and a combined approach of electrical and optical control for gap loading of antenna devices are desirable for integration with existing silicon technologies.

Another route to achieve fully controlled gap loading is via all-optical control using the ultrafast response as obtained with femtosecond laser pulses. For the work in this thesis, we used picosecond pulses. Femtosecond pulses make a whole new regime of ultrafast control accessible and will open a window into femtosecond dynamics of carriers in our antenna hybrid devices.

Investigating the ultrafast response and saturable absorption with femtosecond pulses will also be a first step towards integration of plasmonic nanoantenna switches with VECSELs (Vertical External Cavity Surface Emitting Lasers) which conventionally use semiconductor saturable absorber mirros (SESAMs) [203]. Epitaxially grown quantum wells are used as SESAMs so far, but gaploading antennas based on ultrafast switching of conductive oxides in the gap might prove a feasible alternative plasmonic SESAM with the added advantage of better tunability and reproducibility [67].

Another material of potential interest for gaploading is cadmium telluride (CdTe), deposited by electrochemical deposition. First steps have been taken by mixing a CdTe deposition solution and depositing layers of different compositions to optimise the composite ratio of cadmium and tellurium. Electrochemical growth of gold nanoantennas with variable length inside of Anodised Aluminium Oxide (AAO) membranes has been explored by many groups [60, 140]. With this knowledge, we have fabricated first nanoantenna devices consisting of single gold nanorods, see Fig. 7.1, a first step towards dimers with CdTe in the gap. It is also possible to electrochemically deposit nanorod dimers with nm thin self-assembled monolayer (SAM) buffers in the gap [195, 196, 197, 204], opening up possibilities for “barcode” oligomers with CdTe, Au and SAM segments aligned along the same axis.

Once full switching with nanoantennas has been achieved, the integration of single nanoantenna switches with a silicon photonic waveguide follows as a logical next step. First results of linear coupling between antennas and waveguides have been reported recently [205, 206] – integration with nanoantenna switches will allow all-optical nanoscale

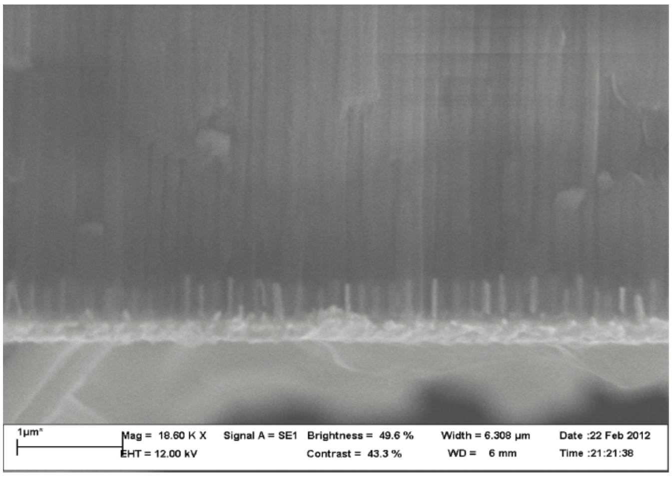

Figure 7.1: Gold nanoantennas of 500 nm length in an AAO matrix, fabricated by electrochemical deposition.

control of transmission in silicon waveguides and mark an important step towards miniturisation of optical circuits.

Another direction is the further exploitation of our energy transfer mechanism by fast electron injection, especially in conjunction with phase-change materials. Phase change materials such as vanadium dioxide (VO_2) have been of great interest for use in optical and electronic nanodevices for the last thirty years [88]. There are two avenues to investigate here: The VO_2 with its sharp transition from the insulating to the metallic state just above room temperature could be used as a gaploading material in nanoantenna switches as proposed in chapter 4. On the other hand, we could use nanostructures, starting with simple gold disks resonant at different wavelengths, as nanoactuators to drive the phase transition on the nanoscale. The fast electron injection that occurs on the picosecond scale might thus enable picosecond for- and backwards switching of VO_2. Another point of interest is also the change in optical response of the nanostructure due to the refractive index change in the phase-changed substrate, closing the circle to nanoantenna switches.

The idea of an all-optical actuator can also be expanded to other phase-change materials such as chalcogenides. All-optical writing and rewriting of GST (Ge:Sb:Te) is already used in rewritable CD and DVD technology, where bit memory cells are addressed individually. These addressed memory cells could be made even smaller by addressing them via plasmonic actuators or even hotspots in optical gap antennas [207, 208], thus achieving unprecedented areal densities and fast writing speeds.

In conclusion, I hope that I have been able to give a conclusive overview of a small part of the exciting work that is being conducted to obtain fundamental insights into the behaviour of structures on the nanoscale and to integrate plasmonic devices with existing technologies. As shown in this section, there is a lot of further investigations still to be done and I firmly believe that we have only seen the beginning of “the golden age of plasmonics”.

Bibliography

[1] E. Abbe,"Beiträge zur Theorie des Mikroskops und der mikroskopischen Wahrnehmung", Arch. Mikrosk. Anat. **9**, 413 (1873).

[2] M. Brongersma and V. Shalaev, "The case for plasmonics", Science **328**, 440 (2010).

[3] M. Faraday, "Experimental relations of gold (and other metals) to light", Phil. Trans. R. Soc. Lond. **147**, 145 (1857).

[4] K. A. Willets and R. P. Van Duyne, "Localized Surface Plasmon Resonance Spectroscopy and Sensing", Ann. Rev. Phys. Chem. 58, 267 (2007).

[5] W. A. Murray and W. L. Barnes, "Plasmonic Materials", Adv. Mat. **19**, 3771 (2007).

[6] U. Kreibig and M. Vollmer, "Optical Properties of Metal Clusters", Springer Series in Materials Science **25**, Springer, Heidelberg (1995).

[7] G. Mie, "Beiträge zur Optik trüber Medien, speziell kolloidaler Metalllösungen", Ann. Phys. **25**, 377 (1908).

[8] C. F. Bohren and D. R. Huffman, "Absorption and Scattering of Light by Small Particles", Wiley-VCH, Weinheim (2004).

[9] J. Dorfmueller, R. Vogelgesang, W. Khunsin, C. Rockstuhl, C. Etrich and K. Kern, "Plasmonic Nanowire Antennas: Experiment, Simulation, and Theory", Nano Lett. **9**, 3596 (2010).

[10] J. Dorfmueller, "Optical Wire Antennas: Near-Field Imaging, Modeling and Emission Patterns", PhD thesis, University of Lausanne (2010), `http://library.epfl.ch/en/theses/?nr=4707`.

[11] H. Wang, D. W. Brandl, F. Le, P. Nordlander and N. J. Halas, "Nanorice: A Hybrid Plasmonic Nanostructure", Nano Lett. **4**, 827 (2006).

[12] V. Giannini, R. Rodríguez-Oliveros and J. A. Sánchez-Gil, "Surface Plasmon Resonances of Metallic Nanostars/Nanoflowers for Surface-Enhanced Raman Scattering", Plasmonics **5**, 99 (2010).

[13] R. Rodríguez-Olivreos and J. A. Sánchez-Gil, “Gold nanostars as thermoplasmonic nanoparticles for optical heating”, Opt. Expr. **20**, 621 (2010).

[14] A. M. Kern and O. J. F. Martin, “Excitation and reemission of molecules near realistic plasmonic nanostructures”, Nano Lett. **11**, 482 (2011).

[15] L. Hirsch, R. Stafford, J. Bankson, S. Sershen, B. Rivera, R. Price, J. Hazle, N. J. Halas and J. L. West, “Nanoshell-mediated near-infrared thermal therapy of tumors under magnetic resonance guidance”, Proc. Natl. Acad. Sci. USA **100**, 13549 (2003).

[16] C. Loo, A. Lowery, N. J. Halas, J. L. West and R. A. Drezek, “Immunotargeted nanoshells for integrated cancer imaging and therapy”, Nano Lett. **5**, 709 (2005).

[17] M. I. Stockman, “Nanoplasmonics: The physics behind the applications”, Phys. Today **64**, 39 (2011).

[18] N. Liu, M. Tang, M. Hentschel, H. Giessen and A. Alivisatos, “Nanoantenna-enhanced gas sensing in a single tailored nanofocus”, Nat. Mat. **10**, 631 (2011).

[19] N. Yu, E. Cubukcu, L. Diehl, M. A. Belkin, K. B. Crozier F. Capasso, D. Bour, S. Corzine and G. Höfler, “Plasmonic quantum cascade laser antenna”, Appl. Phys. Lett. **91**, 173113 (2007).

[20] J. K. Trautman, J. J. Macklin, L. E. Brus and E. Betzig, “Near-field spectroscopy of single molecules at room temperature”, Nature **369**, 40 (1994).

[21] K. Kneipp, “Surface-Enhanced Raman Scattering”, Phys. Today **60**, 11 (2007).

[22] H. Atwater and A. Polman, “Plasmonics for improved photovoltaic devices”, Nat. Mat. **9**, 205 (2010).

[23] V. E. Ferry, M. A. Verschuuren, H. B. T. Li, E. Verhagen, R. J. Walters, R. E. I. Schropp, H. A. Atwater and A. Polman, “Light trapping in ultrathin plasmonic solar cells”, Opt. Expr. **18**, A237 (2010).

[24] M. W. Knight, H. Sobhani, P. Nordlander and N. J. Halas, “Photodetection with Active Optical Antennas”, Science **332**, 702 (2011).

[25] J. Valentine, S. Zhang, T. Zentgraf, E. Ulin-Avila, D. A. Genov, G. Bartal and X. Zhang, “Three-dimensional optical metamaterial with a negative refractive index”, Nature **455**, 376 (2008).

[26] D. R. Smith, J. B. Pendry and M. C. K. Wiltshire, “Metamaterials and Negative Refractive Index”, Science **305**, 788 (2004).

[27] D. Schurig, J. J. Mock, B. J. Justice, S. A. Cummer, J. B. Pendry, A. F. Starr and D. R. Smith, “Metamaterial Electromagnetic Cloak at Microwave Frequencies”, Science **314**, 977 (2006).

[28] J. B. Pendry, D. Schurig and D. R. Smith, “Controlling Electromagnetic Fields”, Science **312**, 1780 (2006).

[29] J. K. Rowling, “Harry Potter and the Philosopher’s Stone”, Bloomsbury, London (1997).

[30] W. L. Barnes, A. Dereux and T. W. Ebbesen, “Surface plasmon subwavelength optics”, Nature **424**, 824 (2003).

[31] T. W. Ebbesen, C. Genet and S. I. Bozhevolnyi, “Surfaceplasmon circuitry”, Phys. Today **61**, 44 (2008).

[32] E. Feigenbaum and H. A. Atwater , “Resonant Guided Wave Networks”, Phys. Rev. Lett. **104**, 147402 (2010).

[33] P. C. D. Hobbs, R. B. Laibowitz, F. R. Libsch, N. C. LaBianca and P. P. Chiniwalla, “Efficient waveguide-integrated tunnel junction detectors at 1. 5 μm” Opt. Expr. **15**, 16376 (2007)

[34] S. A. Maier, “Plasmonics: Fundamentals and Applications”, Springer, New York (2007).

[35] L. Novotny and B. Hecht, “Principles of Nano-Optics”, Cambridge University Press (2007).

[36] M. Schnell, A. Garcia-Etxarri, A. J. Huber, K. Crozier, J. Aizpurua and R. Hillenbrand, “Controlling the near-field oscillations of loaded plasmonic nanoantennas”, Nat. Phot. **3**, 287 (2009).

[37] L. Novotny, “From near-field optics to optical antennas”, Phys. Today **64**, 47 (2011).

[38] P. Ghenuche, S. Cherukulappurath, T. H. Taminiau, N. F. van Hulst and R. Quidant, “Spectroscopic Mode Mapping of Resonant Plasmon Nanoantennas”, Phys. Rev. Lett. **101**, 116805 (2008).

[39] L. Novotny, “Nano-optics: Optical antennas tuned to pitch”, Nature **455**, 887 (2008).

[40] J. Zuloaga, E. Prodan and P. Nordlander, “Quantum Plasmonics: Optical Properties and Tunability of Metallic Nanorods”, ACS Nano, **4**, 5269 (2010).

[41] J. Scholl, A. Koh, and J. Dionne, “Quantum plasmon resonances of individual metallic nanoparticles”, Nature **483**, 421 (2012).

[42] N. Halas, “Plasmonics: An Emerging Field Fostered by *Nano Letters*”, Nano Lett. **10**, 3816 (2010).

[43] E. D. Palik, “Handbook of Optical Constants of Solids”, Academic Press, New York (1991).

[44] P. B. Johnson and R. W. Christy, “Optical Constants of the Noble Metals”, Phys. Rev. **B6**, 4370 (1972).

[45] P. G. Etchegoin, E. C. Le Ru and M. Meyer, “An analytical model for the optical properties of gold”, J. Chem. Phys. **125**, 164705 (2006).

[46] A. D. Boardman, “Electromagnetic surface modes”, John Wiley & Sons (1982).

[47] H. Fischer, “Enhancement and Subwavelength Confinement of Light in Plasmonic Nanostructures”, PhD thesis, University of Lausanne (2008), `http://infoscience.epfl.ch/record/125995`.

[48] F. J. González, J. Alda, J. Simón, J. Ginn and G. Boreman, “The effect of metal dispersion on the resonance of antennas at infrared frequencies”, Infrared Phys. Tech., **52**, 48 (2009).

[49] O. Stenzel, “The physics of thin film optical spectra: an introduction”’, Springer, Berlin (1996).

[50] J. Aizpurua, G. W. Bryant, L. J. Richter, F. J. García de Abajo, B. K. Kelley and T. Mallouk, “Optical properties of coupled metallic nanorods for field-enhanced spectroscopy”, Phys. Rev. B **71**, 235420 (2005).

[51] L. Novotny, “Effective Wavelength Scaling for Optical Antennas”, Phys. Rev. Lett. **98**, 266802 (2007).

[52] G. W. Bryant, F. J. García de Abajo and J. Aizpurua, “Mapping the Plasmon Resonances of Metallic Nanoantennas”, Nano Lett. **2**, 631 (2008).

[53] C. Fumeaux, M. A. Gritz, I. Codreanu, W. L. Schaich, F.J. González and G. D. Boreman, “Measurement of the resonant lengths of infrared dipole antennas”, Infrared Phys. Tech. **41**, 271 (2000).

[54] F. Neubrech, T. Kolb, R. Lovrincic, G. Fahsold, A. Pucci, J. Aizpurua, T. W. Cornelius, M. E. Toimil-Molares, R. Neumann and S. Karim, “Resonances of individual metal nanowires in the infrared”, Appl. Phys. Lett. **89**, 253104 (2006).

[55] F. Neubrech, “Oberflaechenverstärkte Infrarot-Spektroskopie mittels Gold-Nanoantennen”, PhD thesis, University of Heidelberg (2008), `http://archiv.ub.uni-heidelberg.de/volltextserver/` frontdoor.php?source_opus=8799.

[56] T. Ung, L. M. Liz-Marzán and P. Mulvaney, “Optical Properties of Thin Films of Au@SiO_2 Particles”, J. Phys. Chem. B **105**, 3441 (2001).

[57] P. K. Jain, X. Huang, I. H. El-Sayed and M. A. El-Sayed, “Noble Metals on the Nanoscale: Optical and Photothermal Properties and Some Applications in Imaging, Sensing, Biology, and Medicine”, Acc. Chem. Res. **41**, 1578 (2008).

[58] R. Abargues, J. Marqués-Hueso, J. Canet-Ferrer, E. Pedrueza, J. L. Valdés, E. Jiménez and J. P. Martínez-Pastor, “High-resolution electron-beam patternable nanocomposite containing metal nanoparticles for plasmonics”, Nanotechnology **19**, 355308 (2008).

[59] A. A. Tseng, “Recent developments in micromilling using focused ion beam technology”, J. Micromech. Microeng. **14**, R15 (2004).

[60] H. Yao, J. Duan, D. Mo, H. Y. Günel, Y. Chen, J. Liu and T. Schäpers, “Optical and electrical properties of gold nanowires synthesized by electrochemical deposition”, J. Appl. Phys. **110**, 094306 (2011).

[61] Y.-Y. Yu, S.-S. Chang, C.-L. Lee and C. R. C. Wang, “Gold Nanorods: Electrochemical Synthesis and Optical Properties”, J. Phys. Chem. B **101**, 6661 (1997).

[62] N. Van Hoang, S. Kumar and G.-H. Kim, “Growth of segmented gold nanorods with nanogaps by the electrochemical wet etching technique for single-electron transistor applications”, Nanotechnology **20**, 125607 (2009).

[63] L. Novotny and N. van Hulst, “Antennas for light”, Nat. Phot. **5**, 83 (2011).

[64] P. Bharadwaj, B. Deutsch and L. Novotny, “Optical Antennas”, Adv. Opt. Photonics **1**, 438 (2009).

[65] A. G. Curto, G. Volpe, T. H. Taminiau, M. P. Kreuzer, R. Quidant and N. F. van Hulst, “Unidirectional Emission of a Quantum Dot Coupled to a Nanoantenna”, Science **329**, 5994 (2010).

[66] D. J. Bergman and M. I. Stockman, “Surface Plasmon Amplification by Stimulated Emission of Radiation: Quantum Generation of Coherent Surface Plasmons in Nanosystems”, Phys. Rev. Lett **90**, 027402 (2003).

[67] N. Large, M. Abb, J. Aizpurua and O. L. Muskens, “Photoconductively Loaded Plasmonic Nanoantenna as Building Block for Ultracompact Optical Switches”, Nano Lett. **10**, 1741 (2010).

[68] H. Fredriksson, Y. Alaverdyan, A. Dmitriev, C. Langhammer, D. S. Sutherland, M. Zäch and B. Kasemo, “Hole-Mask Colloidal Lithography”, Advanced Materials, **19**, 4297 (2007).

[69] T. Shegai, S. Chen, V. D. Miljković, G. Zengin, P. Johansson and M. Käll, “A bimetallic nanoantenna for directional colour routing”, Nat. Comm. **2**, 481 (2011).

[70] J. Zhao, B. Frank, S. Burger and H. Giessen, “Large-Area High-Quality Plasmonic Oligomers Fabricated by Angle-Controlled Colloidal Nanolithography”, ACS Nano **5**, 9009 (2011).

[71] S. Cataldo, J. Zhao, B. Frank, F. Neubrech, B. Frank, C. Zhang, P. V. Braun and H. Giessen, “Hole-Mask Colloidal Nanolithography for Large-Area Low-Cost Metamaterials and Antenna-Assisted Surface-Enhanced Infrared Absorption Substrates”, ACS Nano **6**, 979 (2012).

[72] W. B. J. Zimmerman, “Multiphysics Modelling with Finite Element Methods”, *Series on stability, vibration and control of systems*, Issue 18, World Scientific Publishing, London (2006).

[73] M. Mayr and U. Thalhofer, “Numerische Lösungsverfahren in der Praxis: FEM-BEM-FDM”, Hanser Elektronik (1993).

[74] M. Abb, E. P. A. M. Bakkers and O. L. Muskens, “Ultrafast dephasing of light in strongly scattering GaP nanowires”, Phys. Rev. Lett. **106**, 143902 (2011).

[75] M. W. Knight and N. J. Halas, “Nanoshells to nanoeggs to nanocups: optical properties of reduced symmetry core shell nanoparticles beyond the quasistatic limit”, New J. of Phys. **10**, 105006 (2008).

[76] J. T. Katsikadelis, “Boundary Elements Theory and Applications”, Elsevier, Oxford (2002).

[77] P. K. Banerjee, “The Boundary Element Methods in Engineering”, McGraw-Hill College (1994).

[78] F. J. García de Abajo and A. Howie, “Relativistic Electron Energy Loss and Electron-Induced Photon Emission in Inhomogeneous Dielectrics”, Phys. Rev. Lett. **80**, 5180 (1998).

[79] F. J. García de Abajo and A. Howie, “Retarted field calculation of electron energy loss in inhomogeneous dielectrics”, Phys. Rev. **B65**, 115418 (2002).

[80] K. S. Yee, “Numerical solution of initial boundary value problems involving Maxwell’s equations in isotropic media”, IEEE T. Antenn. Propag. **14**, 302 (1966).

[81] J. Stodolka, D. Nau, M. Frommberger, C. Zanke, H. Giessen and E. Quandt, “Fabrication of two-dimensional hybrid photonic crystals utilizing electron beam lithography”, Micrelectron. Eng. **78-79**, 442 (2005).

[82] M. A. Otte, M.-C. Estevez, D. Regatos, L. M. Lechuga and B. Sepúlveda, “Guiding Light in Monolayers of Sparse and Random Plasmonic Meta-atoms”, ACS Nano **5**, 9179 (2011).

[83] A. Boltasseva and H. A. Atwater, “Low-loss plasmonic metamaterials”, Science **331**, 290 (2011)

[84] P. R. West, S. Ishii, G. V. Naik, N. K. Emani, V. M. Shalaev and A. Boltasseva, “Searching for better plasmonic materials”, Laser Photonics Rev. **4**, 795 (2010).

[85] G. V. Naik and A. Boltasseva, “A comparative study of semiconductor-based plasmonic metamaterials”, Metamaterials **5**, 1 (2011).

[86] G. V. Naik and A. Boltasseva, “Semiconductors for plasmonics and metamaterials”, Phys. Status Solidi RRL **4**, 295 (2010).

[87] G. V. Naik, J. Kim and A. Boltasseva, “Oxides and nitrides as alternative plasmonic materials in the optical range”, Opt. Mater. Express **1**, 1090 (2011).

[88] Z. Yang, C. Ko and S. Ramanathan, “Oxide Electronics Utilizing Ultrafast Metal-Insulator Transitions”, Annu. Rev. Mater. Res., **41**, 337 (2011).

[89] J. Davenas, S. Besbes and H. Ben Ouada, “NIR spectrophotometry characterization of ITO electronic property changes at the interface with a PPV derivative”, Synth. Met. **138**, 295 (2003).

[90] S. A. Bashar, “Study of Indium Tin Oxide (ITO) for Novel Optoelectronic Devices”, PhD Thesis, King’s College, London (1998), `http://www.betelco.com/sb/phd/`.

[91] R. N. Joshi, V. P. Singh and J. C. McClure, “Characteristics of indium tin oxide films deposited by r.f. magnetron sputtering”, Thin Solid Films **257**, 32 (1995).

[92] L. Kerkache, A. Layadi, E. Dogheche and D. Rémiens, “Physical properties of RF sputtered ITO thin films and annealing effect”, J. Phys. D: Appl. Phys. **39**, 184 (2006).

[93] S. Takayama, A. Tanaka, T. Sugawara and T. Himuro, “Effects of Oxygen Gas Annealing on Electrical Properties and Internal Stress in Indium Tin Oxide Films”, Jap. J. of Appl. Phys. **41**, L619 (2002).

[94] T.-C. Lin, S.-C. Chang and C.-F. Chiu, “Annealing effect of ITO and ITO/Cu transparent conductive films in low pressure hydrogen atmosphere”, Mat. Sc. and Eng.: B **129**, 39 (2006).

[95] R. X. Wang, C. D. Beling, S. Fung, A. B. Djurišić, C. C. Ling, C. Kwong and S. Li, “Influence of annealing temperature and environment on the properties of indium tin oxide thin films”, J. Phys. D: Appl. Phys. **38**, 2000 (2005).

[96] S.-C. Chang, “Low-pressure H2/N2 annealing on indium tin oxide film”, Microel. J. **38**, 1220 (2007).

[97] M. Abb, P. Albella, J. Aizpurua and O. L. Muskens, “All-Optical Control of a Single Plasmonic Nanoantenna-ITO Hybrid”, Nano Lett. **11**, 2457 (2011).

[98] M. Abb and O. L. Muskens, “Ultrafast Plasmonic Nanoantenna-ITO Hybrid Switches”, Int. J. of Opt. **2012**, 132542 (2012).

[99] P. Banerjee, W.-J. Lee, K.-R. Bae, S. B. Lee and F. W. Rubloff, "Structural, electrical and optical properties of atomic layer deposition Al-doped ZnO films", J. of Appl. Phys. **108**, 043504 (2010).

[100] D.-J. Lee, J.-Y. Kwon, S.-H. Kim, H.-M. Kim and K.-B. Kim, "Effect of Al Distribution on Carrier Generation of Atomic Layer Deposited Al-Doped ZnO Films", J. Electrochem. Soc. **158**, D277 (2011).

[101] D.-J. Lee, H.-M. Kim, J.-Y. Kwon, H. Choi, S.-H. Kim and K.-B. Kim, "Structural and Electrical Properties of Atomic Layer Deposited Al-Doped ZnO Films", Adv. Funct. Mater. **21**, 448 (2011).

[102] M. Rusu, A. Grudinin and O. Okhotnikov, "Slicing the supercontinuum radiation generated in photonic crystal fiber using an all-fiber chirped-pulse amplification system", Opt. Express **13**, 6390 (2005).

[103] A. Arbouet, D. Christofilos, N. Del Fatti, F. Vallée, J. R. Huntzinger, L. Arnaud, P. Billaud and M. Broyer, "Direct Measurement of the Single-Metal-Cluster Optical Absorption", Phys. Rev. Lett. **93**, 127401 (2004).

[104] O. L. Muskens, P. Billaud, M. Broyer, N. Del Fatti and F. Vallée, "Optical extinction spectrum of a single metal nanoparticle: Quantitative characterization of a particle and of its local environment", Phys. Rev. **B78**, 205410 (2008).

[105] O. Muskens, D. Christofilos, N. Del Fatti and F. Vallée, "Optical response of a single noble metal nanoparticle", J. of Opt. A: Pure Appl. Opt. **8**, S264 (2006).

[106] C.-Y. Tsai, J.-W. Lin, C.-Y. Wu, P-T. Lin, T.-W. Lu and P.-T. Lee, "Plasmonic Coupling in Gold Nanoring Dimers: Observation of Coupled Bonding Mode", Nano Lett. **12**, 1648 (2012).

[107] P. Anger, P. Bharadwaj and L. Novotny, "Enhancement and Quenching of Single-Molecule Fluorescence", Phys. Rev. Lett. **96**, 113002 (2006).

[108] S. Kühn, U. Hakanson, L. Rogobete and, V.Sandoghdar, "Enhancement of Single-Molecule Fluorescence Using a Gold Nanoparticle as an Optical Nanoantenna", Phys. Rev. Lett. **97**, 017402 (2006).

[109] O. L. Muskens, V. Giannini, J. A. Sánchez-Gil and J.Gómez Rivas, "Strong Enhancement of the Radiative Decay Rate of Emitters by Single Plasmonic Nanoantennas", Nano Lett. **7**, 2871 (2007).

[110] L. Shao, K. C. Woo, H. Chen, Z. Jin, J. Wang and H.-Q. Lin, "Angle- and Energy-Resolved Plasmon Coupling in Gold Nanorod Dimers", ACS Nano **4**, 3053 (2010).

[111] C. Tabor, D. Van Haute and M. A. El-Sayed, "Effect of Orientation on Plasmonic Coupling between Gold Nanorods", ACS Nano **9**, 3670 (2009).

[112] N. Verellen, Y. Sonnefraud, H. Sobhani, F.Hao, V. V.Moshchalkov, P. Van Dorpe, P. Nordlander and S. A. Maier, “Fano Resonances in Individual Coherent Plasmonic Nanocavities”, Nano Lett. **9**, 1663 (2009).

[113] B. Luk’yanchuk, N. I. Zheludev, S. A. Maier, N. J. Halas, P. Nordlander, H. Giessen and C. T. Chong, “The Fano Resonance in Plasmonic Nanostructures and Metamaterials”, Nat. Mater. **9**, 707 (2010).

[114] S. Zhang, D. A. Genov, Y. Wang, M. Liu and X. Zhang, “Plasmon-Induced Transparency in Metamaterials”, Phys. Rev. Lett. **101**, 047401 (2008).

[115] N. Liu, L. Langguth, T. Weiss, J. Kästel, M. Fleischhauer, T. Pfau and H. Giessen, “Plasmonic Analogue of Electromagnetically Induced Transparency at the Drude Damping Limit”, Nat. Mater. **8**, 758 (2009).

[116] Z.-J. Yang, Z.-S. Zhang, L.-H. Zhang, Q.-Q. Li, Z.-H. Hao and Q.-Q. Wang, “Fano Resonances in Dipole-Quadrupole Plasmon Coupling Nanorod Dimers”, Opt. Lett. **36**, 1542 (2011).

[117] O. L. Muskens, V. Giannini, J. A. Sánchez-Gil and J. Gómez Rivas, “Optical scattering resonances of single and coupled dimer plasmonic nanoantennas”, Opt. Expr. **15**, 17736 (2007).

[118] H. Wei, A. Reyes-Coronado, P. Nordlander, J. Aizpurua, H. Xu, “Multipolar Plasmon Resonances in Individual Ag Nanorice”, ACS Nano **4**, 2649 (2010).

[119] F. Chen, N. Alemu and R. L. Johnston, “Collective plasmon modes in a compositionally asymmetric nanoparticle dimer”, AIP Adv. **1**, 032134 (2011).

[120] K. C. Woo, L. Shao, H. Chen, Y. Liang, J. Wang and H.-Q. Lin, “Universal Scaling and Fano Resonance in the Plasmon Coupling between Gold Nanorods”, ACS Nano **5**, 5976 (2011).

[121] F. J. García de Abajo, “Non-local effects in the plasmons of strongly interacting nanoparticles, dimers, and waveguides”, J. Phys. Chem. C **112**, 17983 (2008).

[122] A. J. Pasquale, B. M. Reinhard and L. Dal Negro, “Engineering Photonic-Plasmonic Coupling in Metal Nanoparticle Necklaces”, ACS Nano **5**, 6578 (2011).

[123] L. Langguth and H. Giessen, “Coupling Strength of complex plasmonic structures in the multiple dipole approximation”, Opt. Expr. **19**, 22156 (2011).

[124] C. Huang, X. Yin, L. Kong and Y. Zhu, “Interactions of nanorod particles in the strong coupling regime”, J. Phys. Chem. C **114**, 21123 (2010).

[125] B. M. Reinhard, M. Siu, H. Agarwar, A. P. Alivisatos and J. Liphardt, “Calibration of Dynamic Molecular Rulers Based on Plasmon Coupling between Gold Nanoparticles”, Nano Lett. 5, 2246 (2005).

[126] P. K. Jain, W. Huang, M. A. El-Sayed, "On the Universal Scaling Behavior of the Distance Decay of Plasmon Coupling in Metal Nanoparticle Pairs: A Plasmon Ruler Equation", Nano Lett. **7**, 2080 (2007).

[127] P. K. Jain, M. A. El-Sayed, "Universal Scaling of Plasmon Coupling in Metal Nanostructures: Extension from Particle Pairs to Nanoshells", Nano Lett. **7**, 2854 (2007).

[128] P. K. Jain, M. A. El-Sayed, "Surface Plasmon Coupling and Its Universal Size Scaling in Metal Nanostructures of Complex Geometry: Elongated Particle Pairs and Nanosphere Trimers", J. Phys. Chem. C **112**, 4954 (2008).

[129] C. Tabor, R. Murali, M. Mahmoud, M. A. El-Sayed, "On the Use of Plasmonic Nanoparticle Pairs As a Plasmon Ruler: The Dependence of the Near-Field Dipole Plasmon Coupling on Nanoparticle Size and Shape", J. Phys. Chem. A **113**, 1946 (2009).

[130] A. M. Funston, C. Novo, T. J. Davis and P. Mulvaney, "Plasmon Coupling of Gold Nanorods at Short Distances and in Different Geometries", Nano Lett. **9**, 1651 (2009).

[131] I. Romero, J. Aizpurua, G. W. Bryant and F. J. García de Abajo, "Plasmons in nearly touching metallic nanoparticles: singular response in the limit of touching dimers", Opt. Expr. **14**, 9988 (2006).

[132] J. Zuloaga and P. Nordlander, "On the Energy Shift between Near-Field and Far-Field Peak Intensities in Localized Plasmon Systems", Nano Lett. **11**, 1280 (2011).

[133] J. Zuloaga, E. Prodan, and P. Nordlander, "Quantum Description of the Plasmon Resonances of a Nanoparticle Dimer", Nano Lett. **9**, 887 (2009).

[134] E. Prodan, C. Radloff, N. J. Halas and P. Nordlander, "A Hybridization Model for the Plasmon Response of Complex Nanostructures", Science **302**, 419 (2003).

[135] P. Nordlander, C. Oubre, E. Prodan, K. Li and M. I. Stockman, "Plasmon Hybridization in Nanoparticle Dimers", Nano Lett. **4**, 899 (2004).

[136] B. Willingham, D. W. Brandl and P. Nordlander, "Plasmon Hybridization in Nanorod Dimers", Appl. Phys. B **93**, 209 (2008).

[137] M. D. Turner, M. M. Hossain and M. Gu, "The effects of retardation on plasmon hybridization within metallic nanostructures", New J. Phys. **12**, 083062 (2010).

[138] O. Pérez González, "Optical properties and high-frequency electron transport in plasmonic cavities", PhD thesis, Universidad del País Vasco (2011), `http://cfm.ehu.es/nanophotonics/THESIS/Thesis_Olalla_Perez_Nov_2011.pdf`.

[139] J.-S. Huang, J. Kern, P. Geisler, P. Weinmann, M. Kamp, A. Forchel, P. Biagioni and B. Hecht, "Mode Imaging and Selection in Strongly Coupled Nanoantennas", Nano Lett. **10**, 2105 (2010).

[140] E. K. Payne, K. L. Shuford, S. Park, G. C. Schatz and C. A. Mirkin, "Multipole Plasmon Resonances in Gold Nanorods", J. Phys. Chem. B **110**, 2150 (2006).

[141] N. Liu, M. Hentschel, T. Weiss, A. P. Alivisatos and H. Giessen, "Three-Dimensional Plasmon Rulers", Science **332**, 1407 (2011).

[142] M. Danckwerts and L. Novotny, "Optical Frequency Mixing at Coupled Gold Nanoparticles", Phys. Rev. Lett. **98**, 026104 (2007).

[143] J. Petschulat, D. Cialla, N. Janunts, C. Rockstuhl, U. Hübner, R. Möller, H. Schneidewind, R. Mattheis, J. Popp, A. Tünnermann, F. Lederer and T. Pertsch, "Doubly resonant optical nanoantenna arrays for polarization resolved measurements of surface-enhanced Raman scattering", Opt. Expr. **18**, 4184 (2010).

[144] W. Dickson, G. A. Wurtz, P. Evans, D. O'Connor, R. Atkinson, R. Pollard and A. V. Zayats, "Dielectric-loaded plasmonic nanoantenna arrays: A metamaterial with tuneable optical properties", Phys. Rev. B **76**, 115411 (2007).

[145] N. Large, "Resonant Raman-Brillouin Scattering in Semiconductor and Metallic Nanostructures – From Nano-Acoustics to Acousto-Plasmonics", PhD thesis, Universidad del País Vasco (2011), `http://cfm.ehu.es/nanophotonics`.

[146] K. F. MacDonald, Z. L. Sámson, M. I. Stockman and N. I. Zheludev, "Ultrafast active plasmonics", Nat. Phot. **3**, 55 (2009).

[147] D. Pacifici, H. J. Lezec and H. A. Atwater, "All-optical modulation by plasmonic excitation of CdSe quantum dots", Nat. Phot. **1**, 402 (2007).

[148] G. A. Wurtz, R. Pollard and A. V. Zayats, "Optical Bistability in Nonlinear Surface-Plasmon Polaritonic Crystals", Phys. Rev. Lett. **97**, 057402 (2006).

[149] X. Zhang, B. Sun, J. M. Hodgkiss and R. H. Friend, "Tunable Ultrafast Optical Switching via Waveguided Gold Nanowires", Adv. Mater. **20**, 4455 (2008).

[150] G. A. Wurtz, R. Pollard, W. Hendren, G. P. Wiederrecht, D. J. Gosztola, V. A. Podolskiy and A. V. Zayats, "Designed ultrafast optical nonlinearity in a plasmonic nanorod metamaterial enhanced by nonlocality", Nat. Nanotech. **6**, 107 (2011).

[151] S. Link and M. A. El-Sayed, "Spectral Properties and Relaxation Dynamics of Surface Plasmon Electronic Oscillations in Gold and Silver Nanodots and Nanorods", J. Phys. Chem. B **103**, 8410 (1999).

[152] M. A. van Dijk, M. Lippitz and M. Orrit, "Detection of Acoustic Oscillations of Single Gold Nanospheres by Time-Resolved Interferometry", Phys. Rev. Lett. **95**, 267406 (2005).

[153] A. Alù and N. Engheta, "Tuning the scattering response of optical nanoantennas with nanocircuit loads", Nat. Phot. **2**, 307 (2008).

[154] J. Berthelot, A. Bouhelier, C. Huang, J. Margueritat, G. Colas-des-Francs, E. Finot, J.-C. Weeber, A. Dereux, S. Kostcheev, H. Ibn El Ahrach, A.-L. Baudrion, J. Plain, R. Bachelot, P. Royer and G. P. Wiederrecht, "Tuning of an Optical Dimer Nanoantenna by Electrically Controlling its Load Impedance", Nano Lett. **9**, 3914 (2009).

[155] T. Atay, J.-H. Song and A. V. Nurmikko, "Strongly Interacting Plasmon Nanoparticle Pairs: From Dipole-Dipole Interaction to Conductively Coupled Regime", Nano Lett. **4**, 1627 (2004).

[156] V. R. Almeida, C. A. Barrios, R. R. Panepucci and M. Lipson, "All-optical control of light on a silicon chip", Nature **431**, 1081 (2004).

[157] T. Tanabe, M. Notomi, S. Mitsugi, A. Shinya and E. Kuramochi, "Fast bistable all-optical switch and memory on a silicon photonic crystal on-chip", Opt. Lett. **30**, 2575 (2005).

[158] K. Ikeda, Y. Shen and Y. Fainman, "Enhanced optical nonlinearity in amorphous silicon and its application to waveguide devices", Opt. Expr. **15**, 17761 (2007).

[159] K. Sokolowski-Tinten and D. von der Linde, "Generation of dense electron-hole plasmas in silicon", Phys. Rev. B **61**, 2643 (2000).

[160] A. Esser, K. Seibert, H. Kurz, G. N. Parsons, C. Wang, B. N. Davidson, G. Lucovsky and R. J. Nemanich, "Ultrafast recombination and trapping in amorphous silicon", Phys. Rev. B **41**, 2879 (1990).

[161] D. E. Aspnes, A. A. Studna and E. Kinsbron, "Dielectric properties of heavily doped crystalline and amorphous silicon from 1.5 to 6.0 eV", Phys. Rev. B **29**, 768 (1984).

[162] P. Mühlschlegel, H.-J. Eisler, O. J. F. Martin, B. Hecht and D. W. Pohl, "Resonant optical antennas", Science **308**, 1607 (2005).

[163] A. K. Akimov, A. Mukherjee, C. L. Yu, D. E. Chang, A. S. Zibrov, P. R. Hemmer, H. Park and M. D. Lukin, "Generation of single optical plasmons in metallic nanowires coupled to quantum dots", Nature **450**, 402 (2007).

[164] M. Aeschlimann, M. Bauer, D. Bayer, T. Brixner, F. J. García de Abajo, W. Pfeiffer, M. Rohmer, C. Spindler and F. Steeb, "Adaptive subwavelength control of nano-optical fields", Nature **446**, 301 (2007).

[165] E. Hendry, M. J. Lockyear, J. Gómez Rivas, L. Kuipers and M. Bonn, "Ultrafast optical switching of the THz transmission through metallic subwavelength hole arrays", Phys. Rev. B **75**, 235305 (2007).

[166] H.-T. Chen, W. J. Padilla, M. J. Cich, A. K. Azad, R. D. Averitt and A. J. Taylor, "A metamaterial solid-state terahertz phase modulator", Nat. Phot. **3**, 148 (2009).

[167] O. L. Muskens, N. Del Fatti and F. Vallée, "Femtosecond Response of a Single Metal Nanoparticle", Nano Lett. **6**, 552 (2006).

[168] P. J. Schuck, D. P. Fromm, A. Sundaramurthy, G. S. Kino and W. E. Moerner, "Improving the Mismatch between Light and Nanoscale Objects with Gold Bowtie Nanoantennas", Phys. Rev. Lett. **94**, 017402 (2005).

[169] E. Abraham and S. D. Smith, "Optical bistability and related devices", Rep. Prog. Phys. **45**, 815 (1982).

[170] A. H. Quarterman, K. G. Wilcox, V. Apostolopoulos, Z. Mihoubi, S. P. Elsmere, I. Farrer, D. A. Ritchie and A. Tropper, "A passively mode-locked external-cavity semiconductor laser emitting 60-fs pulses", Nat. Phot. **3**, 729 (2009).

[171] E. Feigenbaum, K. Diest and H. A. Atwater, "Unity-Order Index Change in Transparent Conducting Oxides at Visible Frequencies", Nano Lett. **10**, 2111 (2010).

[172] C. G. Granqvist and A. Hultaker, "Transparent and conducting ITO film: New developments and applications", Thin Solid Films **411**, 1 (2002).

[173] S. Ray, R. Banerjee, N. Basu, A. K. Batabyal and A. K. Barua, "Properties of tin doped indium oxide thin films prepared by magnetron sputtering", J. Appl. Phys. **54**, 3497 (1983).

[174] M. D. Losego, A. Y. Efremenko, C. L. Rhodes, M. G. Cerruti, S. Franzen and J.-P. Maria, "Conductive oxide thin films: Model systems for understanding and controlling surface plasmon resonance", J. Appl. Phys. **106**, 024903 (2009).

[175] J. Zhang, T. Atay and A. V. Nurmikko, "Optical Detection of Brain Cell Activity Using Plasmonic Gold Nanoparticles", Nano Lett. **9**, 519 (2009).

[176] S. H. Brewer and S. Franzen, "Indium Tin Oxide Plasma Frequency Dependence on Sheet Resistance and Surface Adlayers Determined by Reflectance FTIR Spectroscopy", J. Phys. Chem. B **106**, 12986 (2002).

[177] G. Lenz, J. Zimmermann, T. Katsufuji, M. E. Lines, H. Y. Hwang, S. Spälter, R. E. Slusher, S.-W. Cheong, J. S. Sanghera and I. D. Aggarwal, "Large Kerr effect in bulk Se-based chalcogenide glasses", Opt. Lett. **25**, 254 (2000).

[178] H. I. Elim, W. Ji and F. Zhu, "Carrier concentration dependence of optical Kerr nonlinearity in indium tin oxide films", Appl. Phys. B: Laser O. **82**, 439 (2006).

[179] C. Voisin, D. Christofilos, P. A. Loukakos, N. Del Fatti, F. Vallée, J. Lermé, M. Gaudry, E. Cottancin, M. Pellarin and M. Broyer, "Ultrafast electron-electron scattering and energy exchanges in noble-metal nanoparticles", Phys. Rev. B **69**, 195416 (2004).

[180] G. V. Hartland, "Ultrafast studies of single semiconductor and metal nanostructures through transient absorption microscopy", Chem. Sci. **1**, 303 (2010).

[181] S. I. Anisimov, B. L. Kapeliovich and T. L. Perelman, "Electron emission from metal surfaces exposed to ultrashort laser pulses" (Translation), Soviet Physics - JETP **39**, 375 (1974).

[182] F. Hache, D. Ricard, C. Flytzanis and U. Kreibig, "The optical Kerr effect in small metal particles and metal colloids: The case of gold", Appl. Phys. A: Mater. Sci. Process. **47**, 347 (1988).

[183] H. Inouye, K. Tanaka, I. Tanahashi and K. Hirao, "Ultrafast dynamics of nonequilibrium electrons in a gold nanoparticle system", Phys. Rev. B **57**, 11334 (1998).

[184] V. E. Gusev and O. B. Wright, "Ultrafast nonequilibrium dynamics of electrons in metals", Phys. Rev. B **57**, 2878 (1998).

[185] W. A. Schroeder, T. S. Stark and A. L. Smirl, "Hot-carrier enhancement of photorefractive space-charge fields in zinc-blende semiconductors", Opt. Lett. **16**, 989 (1991).

[186] D. H. Hurley, O. B. Wright, O. Matsuda and S. L. Shinde, "Time resolved imaging of carrier and thermal transport in silicon", J. Appl. Phys. **107**, 023521 (2010).

[187] V. Juvé, M. Scardamaglia, P. Maioli, A. Crut, S. Merabia, L. Joly, N. Del Fatti and F. Vallée, "Cooling dynamics and thermal interface resistance of glass-embedded metal nanoparticles", Phys. Rev. B **80**, 195406 (2009).

[188] A. Janotti and C. G. Van de Walle, "Fundamentals of zinc oxide as a semiconductor", Rep. Prog. Phys. 72, 126501 (2009).

[189] P. Kukura, H. Ewers, C. Müller, A. Renn, A. Helenius and V. Sandoghdar, "High-speed nanoscopic tracking of the position and orientation of a single virus", Nat. Methods **6**, 923 (2009).

[190] T. Ashida, A. Miyamura, N. Oka, Y. Sato, T. Yagi, N. Taketoshi, T. Baba and Y. Shigesato, "Thermal transport properties of polycristalline tin-doped indium oxide films", J. Appl. Phys. **105**, 073709 (2009).

[191] S.-M. Lee, D. G. Cahill and T. H. Allen, "Thermal conductivity of sputtered oxide films", Phys. Rev. B **52**, 253 (1995).

[192] T. C. Zhu, H. J. Maris and J. Tauc, "Attenuation of longitudinal-acoustic phonons in amorphous SiO_2 at frequencies up to 440 GHz", Phys. Rev. B **44**, 4281 (1991).

[193] V. Krachmalnicoff, E. Castanié, Y. de Wilde and R. Carminati, "Fluctuations of the Local Density of States Probe Localized Surface Plasmons on Disordered Metal Films", Phys. Rev. Lett. **105**, 183901 (2010).

[194] CRC Materials Science and Engineering Handbook, Third Edition, Edited by James F. Shackelford and William Alexander, CRC Press 2000, ISBN: 978-0-8493-2696-7.

[195] J. K. N. Mbindyo, T. E. Mallouk, J. B. Mattzela, I. Kratochvilova, B. Razavi, T. N. Jackson and T. S. Mayer, "Template synthesis of metal nanowires containing monolayer molecular junctions", J. Am. Chem. Soc. **124**, 4020 (2002).

[196] L. T. Cai, H. Skulason, J. G. Kushmerick, S. K. Pollack, J. Naciri, R. Shashidhar, D. L. Allara, T. E. Mallouk and T. S. Mayer, "Nanowire-Based Molecular Monolayer Junctions: Synthesis, Assembly, and Electrical Characterization", J. Phys. Chem. B 108, 2827 (2004).

[197] C. E. Gardner, M. A. Ghanem, J. W. Wilson and D. C. Smith, "Development of a Nanowire-Based Test Bed Device for Molecular Electronics Applications", Anal. Chem. **78**, 951 (2006).

[198] M. Hentschel, M. Saliba, R. Vogelgesang, H. Giessen, A. P. Alivisatos and N. Liu, "Transition from Isolated to Collective Modes in Plasmonic Oligomers", Nano Lett. **10**, 2721 (2010).

[199] M. Hentschel, D. Dregely, R. Vogelgesang, H. Giessen and N. Liu, "Plasmonic Oligomers: The Role of Individual Particles in Collective Behavior", ACS Nano **5**, 2042 (2011).

[200] D. Dregely, M. Hentschel and H. Giessen, "Excitation and tuning of higher-order Fano resonances in plasmonic oligomer clusters", ACS Nano **5**, 8202 (2011).

[201] I. S. Maksymov, A. E. Miroshnichenko and Y. S. Kishvar, "Actively tunable optical Yagi-Uda nanoantenna with bistable emission characteristics", arXiv:1202.2521v1 [physics.optics] (2012).

[202] M. Y. Zhang and G. J. Cheng, "Highly conductive and transparent alumina-doped ZnO films processed by direct pulsed laser recrystallization at room temperature", Appl. Phys. Lett. **99**, 051904 (2011).

[203] U. Keller, K. J. Weingarten, F. X. Kärtner, D. Kopf, B. Braun, I. D. Jun, R. Fluck, C. Hönninger, N. Matuschek and J. Aus der Au, "Semiconductor Saturable Absorber Mirrors (SESAM's) for Femtosecond to Nanosecond Pulse Generation in Solid-State Lasers", IEEE J. Sel. Top. Quant. **2**, 435 (1996).

[204] R. Whiter, "Working Towards Electrically Contacted Plasmonic Nano-Antennas", Master thesis, University of Southampton (2011).

[205] M. Février, P. Gogol, A. Aassime, R. Mégy, C. Delacourt, A. Chelnokov, A. Apuzzo, S. Blaize, J.-M. Lourtioz and B. Dagens, "Giant Coupling Effect between Metal Nanoparticle Chain and Optical Waveguide", Nano Lett. **12**, 1032 (2012).

[206] F. Degirmenci, I. Bulu, P. Deotare, M. Khan, M. Loncar and F. Capasso, "Waveguide integrated plasmonic platform for sensing and spectroscopy", Proc. SPIE **7941**, 794117 (2011).

[207] D. O'Connor and A. V. Zayats, "Data storage: The third plasmonic revolution", Nat. Nanotech. **5**, 482 (2010).

[208] B. C. Stipe, T. C. Strand, C. C. Poon, H. Balamane, T. D. Boone, J. A. Katine, J.-L. Li, V. Rawat, H. Nemoto, A. Hirotsune, O. Hellwig, R. Ruiz, E. Dobisz, D. S. Kercher, N. Robertson, T. R. Albrecht and B. D. Terris, "Magnetic recording at 1.5 Pb m^2 using an integrated plasmonic antenna", Nat. Phot. **4**, 484 (2010).